

6. Appendixes

Appendix 1: List of prepared layered hydroxides

Appendix 2: Nickel hydroxide ultrathin nanosheets as building blocks for electrochemically active layers (B. Schneiderová, J. Demel, J. Pleštil, P. Janda, J. Bohuslav, D. Ihiawakrim, O. Ersen, G. Rogez, K. Lang, *J. Mater. Chem. A*, **2013**, 1, 11429–11437)

Appendix 3: Electrochemical performance of cobalt hydroxide nanosheets formed by the delamination of layered cobalt hydroxide in water (B. Schneiderová, J. Demel, J. Pleštil, H. Tarábková, J. Bohuslav, K. Lang, *Dalton Trans.*, **2014**, 43, 10484–10491)

Appendix 4: Nickel-cobalt hydroxide nanosheets: Synthesis, morphology and electrochemical properties (B. Schneiderová, J. Demel, A. Zhigunov, J. Bohuslav, H. Tarábková, P. Janda, K. Lang, *J. Colloid Interface Sci.*, **2017**, 499, 138–144)

Appendix 1

List of prepared layered hydroxides: their preparation methods (direct precipitation (DP), hydrothermal precipitation (HP), anion exchange (AE)), precursors, structural type (layered hydroxide salt (LHS), layered double hydroxide (LDH)), Ni or Co coordination and valency and delamination capability.

Layered hydroxide	Preparation method	Precursors	Structure	Coordination	Valency of Ni or	Delamination in water
LNiH-Lac(p)	DP	Ni(Lac) ₂	LHS	octahedral	Ni ²⁺	Yes
LNiH-NO ₃ (p)	DP	Ni(NO ₃) ₂	LHS	octahedral	Ni ²⁺	Yes
LNiH-DS	HP	Ni(NO ₃) ₂	LHS	octahedral	Ni ²⁺	No
LNiH-Lac(ae)	AE	LNH-DS, NaLac	LHS	octahedral	Ni ²⁺	Yes
LNiH-NO ₃ (ae)	AE	LNH-DS, NaNO ₃	LHS	octahedral	Ni ²⁺	No
LCoH-DS	HP	CoCl ₂	LHS/LDH	tetrahedral/ octahedral	Co ²⁺ ,Co ³⁺	No
LCoH-Lac	AE	LCoH-DS, NaLac	LDH	octahedral	Co ²⁺ ,Co ³⁺	Yes
LNiCoH-DS	HP	NiCl ₂ , CoCl ₂ (1:1 n/n)	LHS/LDH	tetrahedral/ octahedral	Ni ²⁺ ,Co ²⁺ ,Co ³⁺	No
LNiCoH-Lac	AE	LNiCoH-DS, NaLac	LDH	octahedral	Ni ²⁺ ,Co ²⁺ ,Co ³⁺	Yes

Apendix 2

Nickel hydroxide ultrathin nanosheets as building blocks for electrochemically active layers†

Cite this: *J. Mater. Chem. A*, 2013, **1**, 11429

Barbora Schneiderová,^{ab} Jan Demel,^a Josef Pleštil,^c Pavel Janda,^d Jan Bohuslav,^{de} Dris Ihiawakrim,^f Ovidiu Ersen,^f Guillaume Rogez^f and Kamil Lang^{*a}

Layered nickel hydroxides (LNHs), intercalated with lactate and nitrate anions, were synthesised using controlled precipitation and anion exchange methods. The present study reports a novel approach for the delamination of LNHs in water into nickel hydroxide nanosheets. The thickness of a single nanosheet varied between 0.7 and 1.0 nm with a lateral dimension between 50 and 80 nm. The nanosheets formed colloidal solutions or gels, retained the original hydroxide structure of LNHs, and were stable for weeks. The nanosheets were re-assembled into large-scale, well-oriented films with adjustable thickness using drop casting and spin coating techniques. The prepared nanostructured films were electrochemically active with stable and reproducible charge–discharge properties in an alkaline electrolyte. These results suggest that the nickel hydroxide nanosheets, prepared by the present methods, have potential as building blocks in the design of nanocomposite materials for energy applications.

Received 31st May 2013

Accepted 24th July 2013

DOI: 10.1039/c3ta12129a

www.rsc.org/MaterialsA

1 Introduction

Layered hydroxides are lamellar compounds^{1–3} that are widely used as polymer fillers⁴ or for the design of novel materials with magnetic,^{5,6} electrochemical,² catalytic,^{7,8} and photochemical functions.^{9–12} The variability of layered hydroxides arises from the combination of the inorganic hydroxide layers with the properties contributed by the host anions intercalated between these layers.¹³ Ultrathin nanosheets, prepared by delamination of layered hydroxides, have many attractive properties given by an exceptional thickness on the order of one nanometer and a lateral size up to micrometers.¹⁴

The most-studied layered hydroxides are layered double hydroxides (LDHs). LDHs can be synthesised in a wide range of compositions with the general formula $[M_{1-x}^{II}M_x^{III}(\text{OH})_2]^{x+}(\text{A}^{m-})_{x/m} \times n\text{H}_2\text{O}$. These materials contain

stacked brucite-like layers where divalent cations are partially replaced by trivalent cations. As a result, these layers possess positive charge balanced by anions in the interlayer space. Growing interest has been directed towards layered simple hydroxides where the layers are composed of a single type of metal cation and the positive charge is imposed by hydroxyl vacancies.^{3,15} In the present work, we focus on layered nickel hydroxide salts (LNHs) that have two polymorphs: α -Ni(OH)₂ has brucite-like Ni(OH)₂ layers and the ideal composition derived from the nitrate salt, Ni₂(OH)₃NO₃ × *n*H₂O, with one-fourth of the OH[−] ions replaced by the nitrate anions located in the interlayer.^{3,15,16} In contrast, the brucite-like structure of β -Ni(OH)₂ does not contain intercalated anions or water molecules and has a small basal spacing of 4.6 Å. It has been documented that the crystal structure, size, and morphology of Ni(OH)₂ have a significant effect on physical and chemical properties.¹⁷ Depending on these parameters, LNHs possess interesting magnetic properties,^{5,6} electrochemical behaviour suitable for the construction of rechargeable batteries and capacitors,^{18,19} and gas-sensing activity.²⁰

LNH, intercalated with dodecyl sulphate (LNH-DS), was identified as a potential material for the preparation of hexagonal α -Ni(OH)₂ nanosheets and hierarchical microspheres useful in ultrathin film devices in energy applications.^{21,22} The LNH layers on graphene have superior electrochemical properties, such as good reversibility and high specific capacitance.^{23,24} α -Ni(OH)₂ undergoes morphological changes during the discharging–charging process caused by the oxidation of Ni(OH)₂ to the corresponding oxide-hydroxide and the reverse reaction.^{21,24,25} During this process, compensating ions from the electrolyte insert and re-insert into a nickel electrode and their mobility in the electrode material is crucial for the overall rate of

^aInstitute of Inorganic Chemistry of the AS CR, v. v. i., Husinec-Řež 1001, 250 68 Řež, Czech Republic. E-mail: lang@iic.cas.cz; Fax: +420 22094 1502; Tel: +420 26617 2193

^bFaculty of Science, Charles University in Prague, Hlavova 2030, 128 43 Praha 2, Czech Republic

^cInstitute of Macromolecular Chemistry of the AS CR, v. v. i., Heyrovského nám. 2, 162 06 Praha 6, Czech Republic

^dJ. Heyrovský Institute of Physical Chemistry of the AS CR, v. v. i., Dolejškova 3, 182 23 Praha 8, Czech Republic

^eInstitute of Chemical Technology, Prague, Technická 5, 166 28 Praha 6, Czech Republic

^fInstitut de Physique et Chimie des Matériaux de Strasbourg, UMR CNRS-Uds 7504, 23 rue du Loess, BP 43, 67034 Strasbourg Cedex 2, France

† Electronic supplementary information (ESI) available: Syntheses, elemental analysis, voltammetric experiments description, TGA/DTA/MS curves, powder XRD patterns, FTIR and UV-Vis spectra, SAXS curves, SEM, TEM and AFM images. See DOI: 10.1039/c3ta12129a

the discharging–charging process.¹⁸ The mobility of the compensating ions is higher in very thin films, as shown for submonolayer deposits of nickel oxo-hydroxides.²⁶ The electrochemistry of LNHs is strongly affected by its morphology.^{23,27}

Delamination of LDHs produces single hydroxide nanosheets that are appropriate building blocks for the construction of nanocomposites or ultrathin/thin films. Usually, high-polarity solvents, higher temperatures, or long reaction times are needed for successful delamination.^{14,28} The first water-based delamination was achieved by Hibino and Kobayashi using Mg/Al-based LDH with intercalated lactate anions.²⁹ Since then, more LDHs containing intercalated lactate,^{30,31} acetate³² or isothionate³³ anions have been delaminated in water. Delamination of layered simple hydroxides is sparse and has not been achieved in water so far.³⁴ Identifying new environmentally friendly methods of preparation of monometallic (composed of a transition metal) nanosheets is of great interest for the functionality of nanostructured devices.

In the present paper, we report that LNHs intercalated with lactate (LNH–lactate) and nitrate (LNH–NO₃) can be delaminated in water to form dense colloidal solutions of nickel hydroxide nanosheets. The synthetic methods affected the sample's crystallinity and the efficiency of the delamination process. The size and morphology of the nanosheets were analysed and the films of assembled nanosheets were studied using cyclic voltammetry.

2 Experimental

2.1 Materials

Nickel nitrate, sodium lactate, sodium dodecyl sulphate (SDS) (all obtained from Sigma-Aldrich), sodium nitrate, nickel chloride, hexamethylenetetramine (HMT) (all obtained from Lachema, Czech Republic), sodium hydroxide (Lachner, Czech Republic), and cetyltrimethylammonium bromide (CTAB) (Acros Organics) were used as purchased. Chloroform and 1-butanol (Penta, Czech Republic) were dried over molecular sieves (Sigma-Aldrich). Deionised water (conductivity < 0.15 μS cm⁻¹) was used throughout the experiments.

2.2 Syntheses

LNH–lactate and LNH–NO₃ synthesised by precipitation. 12.5 mL of 0.75 M NaOH (9 mmol) was added dropwise to 20 mL of 0.35 M nickel lactate or nitrate (7 mmol) under vigorous stirring during 1 hour. The green precipitate was centrifuged and washed three times with water. The products are referred to as LNH–lactate (p) and LNH–NO₃ (p).

LNH–lactate and LNH–NO₃ synthesised by anion exchange. 0.6 g of LNH–DS, 30 mmol of lactate or nitrate (sodium salt), and 2.19 g of CTAB (6 mmol) were dispersed in a mixture of 50 mL of deionised water and 150 mL of chloroform. The reaction mixture was vigorously stirred for 1 hour. The water phases containing the LNH salts were separated and centrifuged. The resulting green products were washed with acetone and three times with water. The products are denoted as LNH–lactate (ae) and LNH–NO₃ (ae).

Delamination of LNHs. Wet LNH–lactate (p) and LNH–NO₃ (p) were dispersed in deionised water and shaken overnight (approximately 20 h). The delaminated products formed dispersions; the highest concentration was 20 mg mL⁻¹. LNH–lactate (ae) was delaminated during the anion exchange reaction, and the nanosheets did not sediment, even after centrifugation at 10 000 rpm for 20 min. The dispersions contained up to 30 mg mL⁻¹ of delaminated nanosheets. At a concentration of 40 mg mL⁻¹, the nanosheets formed gel-like dispersions. LNH–NO₃ (ae) did not delaminate.

2.3 Characterisation techniques

Powder X-ray diffraction (XRD) was performed on a PANalytical X'Pert PRO diffractometer that allowed both reflection and transmission experiments on the same sample. Reflection-mode experiments were set up using the conventional Bragg–Brentano geometry. The incident X-ray beam (Cu X-ray tube, 40 kV, 30 mA) passed through a 0.02 rad Soller slit, a 1/8° divergence slit, a 15 mm fixed mask, and a 1/4° anti-scatter slit. The diffracted beam was detected by a PIXcel linear position-sensitive detector equipped with a β filter, a 0.02 rad Soller slit, and a 1/8° anti-scatter slit. The XRD patterns were recorded between 2 and 85° (2θ) with a step of 0.013° and an acquisition time of 500 s per step. Transmission-mode data were collected using an elliptic focusing mirror, a 0.5° divergence slit, a 0.5° anti-scatter slit, and a 0.02 rad Soller slit in the primary beam. A fast PIXcel detector with an anti-scatter shield and a 0.02 rad Soller slit was used to detect the diffracted beam. The XRD patterns were collected between 1 and 85° (2θ) with a step of 0.013° and an acquisition time of 490 s per step. Qualitative analysis was performed with the HighScorePlus software package (PANalytical, Almelo, The Netherlands, version 3.0) and the JCPDS PDF-2 database.³⁵

Small-angle X-ray scattering (SAXS) experiments were performed using a pinhole camera (Molecular Metrology SAXS System) attached to a microfocussed X-ray beam generator (Osmic MicroMax 002) operating at 45 kV and 0.66 mA (30 W). The camera was equipped with a multiwire, gas-filled area detector with an active area diameter of 20 cm (Gabriel design). Two experimental setups were used to cover the *q* range between 0.005 and 1.1 Å⁻¹ ($q = (4\pi/\lambda)\sin \Theta$, where $\lambda = 1.54$ Å is the wavelength and 2Θ is the scattering angle). The scattering intensities were established on an absolute scale using a glassy carbon standard. The SAXS curves were corrected for scattering using an empty capillary. For $q > 0.5$ Å⁻¹, the intensity was identified using the scattering from the solvent and was fitted to the empirical formula $Iw(q) = a + bq^\alpha$, where the exponent α is close to 3. The obtained intensity was subtracted from the experimental scattering curves. The validity of this procedure was supported by the fitted values of *a*, which are close to the forward scattering intensity of water (0.01632 cm⁻¹) calculated from the isothermal compressibility.³⁶

Atomic force microscopy (AFM) images were collected using a Nanoscope IIIa Multimode instrument (Bruker, USA) in the semicontact (tapping) mode using Si cantilevers (OTESPA, Bruker, USA) with ~300 kHz resonant frequency to minimise

tip-surface interaction and avoid surface alteration upon scanning. The AFM samples were prepared by spin-coating or drop-casting on mica and highly ordered pyrolytic graphite (HOPG). The samples on the HOPG support were also utilised for electrochemical studies.

Transmission electron microscopy (TEM) analyses were performed with a spherical aberration (Cs) probe-corrected JEOL 2100F transmission electron microscope with a field emission gun operating at 200 kV using a cryo-holder. A drop of the nanoparticle dispersion was deposited on a TEM grid covered by a thin carbon membrane. The specimen was cooled to liquid nitrogen temperature after its introduction into the microscope. For the LNH-lactate (ae) sample, a more sophisticated preparation protocol was used, consisting of the vitrification of the specimen before introduction into the microscope. In this protocol, a drop of solution is deposited on a carbon membrane TEM grid. Then, the size of the drop is reduced to form a 2D layer using absorbing paper. In the third step, the grid is plunged into liquid nitrogen, and finally, the frozen grid is introduced into pure ethane to form a protective layer covering the specimen.

The Fourier transform infrared spectra (FTIR) were collected on a Nicolet NEXUS 670-FT spectrometer using KBr pellets. Thermal analyses (TGA/DTA/MS) were carried out using a Setaram SETSYS Evolution-16-MS instrument coupled with a mass spectroscopy system.

3 Results and discussion

3.1 Synthesis and elemental analysis

Layered nickel hydroxides with intercalated lactate (LNH-lactate) and nitrate (LNH-NO₃) anions were prepared by two methods: precipitation (p) and anion exchange of dodecyl sulphate (ae) in parent LNH-DS. The synthesis and characterisation of LNH-lactate are described for the first time.

The precipitation was performed by mixing the corresponding nickel salt solutions with sodium hydroxide at room temperature, similar to previously described procedures.^{3,15,37} In contrast to the previous studies,^{15,37} no postsynthesis hydrothermal treatment was applied because this treatment leads to the formation of β-Ni(OH)₂. However even with this precaution, elemental analyses (Table S1, ESI†) and XRD (see below) revealed some presence of β-Ni(OH)₂ in the samples.

The anion exchange method was developed as a general procedure for obtaining highly crystalline LNHS without the presence of the β-phase. The first step involved the hydrothermal synthesis of parent LNH-DS from nickel nitrate and sodium dodecyl sulphate induced by HMT (see ESI†).^{21,38} The obtained LNH-DS had high crystallinity with no signs of the β-phase (see below), and the indicated presence of some nitrogen was due to the traces of HMT.^{21,22,38} The second step followed a reaction scheme originally developed for the intercalation of LDHS.³⁹ The DS anions in LNH-DS were replaced by nitrate or lactate anions in a biphasic water/chloroform system of CTAB. The anion exchange reaction was fast at room temperature because the resulting LNHS remain in the water phase, whereas the nonpolar CTAB-DS ion pair is removed with

chloroform. We found this method to be very efficient for obtaining crystalline LNH materials. The elemental analyses indicated the presence of traces of DS and HMT (Table S1, ESI; also see the FTIR results†).

3.2 Characterisation of the prepared materials

The as-prepared materials were investigated by TGA/DTA/MS, XRD, and FTIR. The thermal behaviour of all samples showed similar features (Fig. S1–S4, ESI†). The first broad endothermic peak between 50 and 150 °C was associated with a weight loss of up to 13% and was attributed to the removal of surface and interlayer water molecules on the basis of mass spectroscopy of the gas products released from the sample. The second step between 250 and 400 °C involved two simultaneous processes: the dehydroxylation of the hydroxide layers and the decomposition of the interlayer anions. In the LNH-lactate samples, the latter process was exothermic and dominated. The onset of this process was shifted to a higher temperature for LNH-lactate (ae) when compared to LNH-lactate (p) due to its better crystallinity (see below). The second step was endothermic for LNH-NO₃ (p) because of nitrate decomposition, as indicated by the NO₂ release. In the case of LNH-NO₃ (ae), the energy consumption of the dehydroxylation and nitrate anion decomposition processes overlapped with the exothermicity of the combustion of minor components (HMT, DS). Additionally, for LNH-NO₃ samples, the good crystallinity of LNH-NO₃ (ae) shifted the second step to higher temperatures. The mass losses for LNH-DS and LNHS (ae) slightly differed from the theoretical values because of some HMT, as described in the literature^{21,38} and confirmed by FTIR spectra and elemental analysis (Table S1, ESI†).

The prepared LNH-DS, LNH-lactate, and LNH-NO₃ samples had a layered structure with 00l diffraction lines between 3 and 20° (Fig. 1, Fig. S5, ESI†). The basal spacing of LNH-DS was 27.2 Å, in good agreement with the literature.²¹ The high efficiency of the anion exchange reaction was revealed by the shrinking of the basal spacing to 10.5 and 10.0 Å for LNH-lactate (ae) and LNH-NO₃ (ae), respectively; good sample

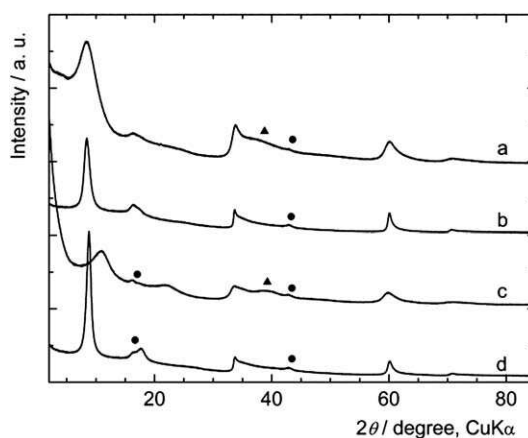


Fig. 1 Powder XRD patterns: (a) LNH-lactate (p); (b) LNH-lactate (ae); (c) LNH-NO₃ (p); and (d) LNH-NO₃ (ae). The diffraction peaks of β-Ni(OH)₂ (▲) and the Mylar foil support (●) are labelled. The samples were measured in the transmission mode.

crystallinity and purity were obtained with all diffractions assigned to the pertinent phase. The obtained basal spacings of LNH-lactate (ae) (10.5 Å) and LNH-lactate (p) (10.4–10.6 Å) were smaller than those of lactate-intercalated Mg/Al and Zn/Al LDHs ($d_{003} = 13.5\text{--}14.5$ Å).^{29,30} The differences are evidently due to the covalent grafting of lactate anions into the nickel hydroxide layers, which leads to a tighter packing of the anions and water molecules in the interlayer space of LNHs, in contrast to the relatively weak hydrogen bonding interactions responsible for the anionic networks in the LDH galleries. The basal spacings of LNH-NO₃ (p) and LNH-NO₃ (ae) were 8.1 and 10.0 Å, respectively. It should be noted that the basal spacing varied slightly from sample to sample, reflecting the variation in the amount of intercalated water and, most likely, the variation in the arrangement of the intercalated nitrate anions. For comparison, the reported basal spacings for LNH-NO₃ are within the broad region of 7–10 Å.^{5,15,21} The nonbasal diffractions of all samples were at approximately 34, 60, and 70° (2θ) and confirmed that the nickel hydroxide layers are not affected by the intercalated anions.

The basal diffraction peaks of LNHs (p) were considerably broadened, indicating their low crystallinity, and some peaks confirmed the presence of the β-Ni(OH)₂ phase (JCPDS-00-014-0117) (Fig. 1). In contrast, LNHs prepared by anion exchange exhibited intense and sharp diffraction peaks with no β-Ni(OH)₂ phase detected. These observations indicate that the anion exchange method is well-suited for obtaining crystalline LNHs intercalated with various anions.

The FTIR spectrum of LNH-DS (Fig. S6, ESI†) exhibited the peaks of intercalated DS molecules^{5,34} and the low-intensity peaks of HMT that remained as an impurity.^{21,38} LNH-lactate (ae) and LNH-lactate (p) (Fig. 2A and B) showed broad peaks at 3430 cm⁻¹ (a), which were attributed to the hydrogen-bonded OH stretching vibrations. The bands in the 3000–2800 cm⁻¹ range (b) belong to the C–H stretching vibrations of the intercalated lactate and, in the case of LNH-lactate (ae), of some remaining DS. The presence of DS was also indicated by the two absorption bands at 1196 cm⁻¹ (f) and 1074 cm⁻¹ (g) assigned to the asymmetric and symmetric stretching modes of the

sulphate group. These bands were missing from the FTIR spectrum of LNH-lactate (p). The strong broad band at 1600 cm⁻¹ (c), which overlaps with the δ(H₂O) band, corresponds to the asymmetric stretching mode, ν_{as} , of the lactate carboxyl group. The corresponding symmetric stretching mode, ν_s , appeared at approximately 1350 cm⁻¹ (d). The differences ($\nu_{as} - \nu_s$) represent a measure of the carboxylate interactions with the environment⁴⁰ and were 226 and 278 cm⁻¹ for LNH-lactate (p) and LNH-lactate (ae), respectively. This splitting indicates the unidentate coordination of the carboxylate group to the nickel atoms of the hydroxide layers. The peaks at 1133 cm⁻¹ for LNH-lactate (p) and at 1157 cm⁻¹ for LNH-lactate (ae) (e) correspond to the C–O stretching vibrations of the lactate hydroxide group.⁴¹

The FTIR spectra of the LNH-NO₃ samples (Fig. 2C and D) had broad peaks at approximately 3400 cm⁻¹ (a) accompanied by the peak at 1632 cm⁻¹ (c) of the δ(H₂O) vibration mode, similar to the LNH-lactate samples. The intense absorption at 1384 cm⁻¹ (j) in LNH-NO₃ (ae) arises from the ν_3 vibration mode of the nitrate ions with D_{3h} symmetry.^{3,15} The presence of the other bands (b, f, g, h and m) indicated DS and HMT impurities.^{21,38} The FTIR spectrum of LNH-NO₃ (p) showed the ν_3 vibration mode of NO₃⁻ at 1384 cm⁻¹ (j), and additional bands at 1495 and 1300 cm⁻¹ (i and k) were attributed to the asymmetric and symmetric stretching modes of the nitrate anions coordinated to the nickel cations. The band at 993 cm⁻¹ (l) was identified as the O–NO₂ stretching vibration. The splitting of the nitrate vibrations in LNH-NO₃ (p) indicated the decreased symmetry of the nitrate anions from D_{3h} to C_{2v} due to the strong nitrate coordination to nickel cations.^{3,5,15,40} The strong interaction of nitrate anions in the interlayer gallery of LNH-NO₃ (p) was also corroborated by smaller basal spacing (8.1 Å) when compared with the more extended structure of LNH-NO₃ (ae) (10.0 Å).

3.3 Delamination and preparation of the films

Shaking fresh and wet LNH-lactate (ae), LNH-lactate (p), and LNH-NO₃ (p) samples in water overnight (~20 h) led to the formation of green colloidal dispersions of nickel hydroxide nanosheets. The resistance of LNH-NO₃ (ae) to delamination was most likely due to high sample crystallinity (Fig. 1).

The most effective delamination was achieved with LNH-lactate (ae). In this case, the delamination occurred quantitatively during the anion exchange reaction, as indicated by the high transparency of the dispersions and the occurrence of the Tyndall effect (Fig. 3A). The delaminated nanosheets did not sediment, even after centrifugation at 10 000 rpm. Therefore, purification of LNH-lactate (ae) by washing with water was associated with a large loss of the delaminated material, and as a result, these dispersions contained some DS as an impurity. Concentrations of the prepared dispersions were scalable up to 40 mg mL⁻¹. At the highest concentrations, the dispersions turned into gels (Fig. 3B). The precipitated LNH-NO₃ (p) and LNH-lactate (p) samples formed dispersions with concentrations up to 20 mg mL⁻¹. In all presented cases, the dispersions were stable over a month.

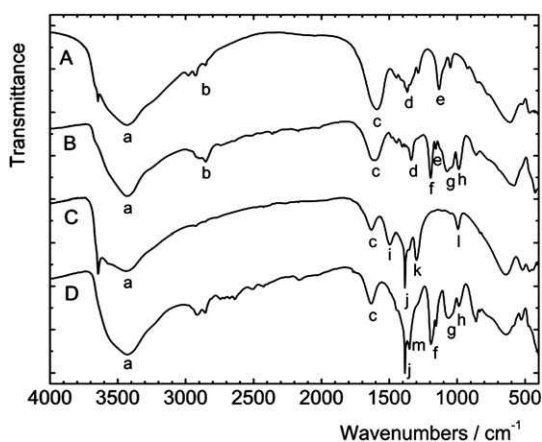


Fig. 2 FTIR spectra: (A) LNH-lactate (p); (B) LNH-lactate (ae); (C) LNH-NO₃ (p); and (D) LNH-NO₃ (ae). The labelling refers to the discussion in the text.

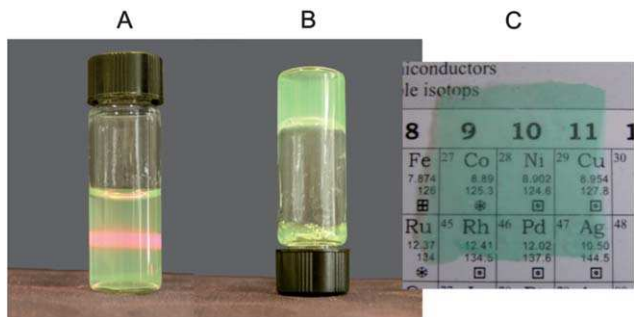


Fig. 3 Delamination of LNH-lactate (ae): (A) dispersion of LNH nanosheets documented by the Tyndall scattering of red laser light; (B) gel-like LNH nanosheets (40 mg mL^{-1}); (C) self-standing film prepared from the LNH nanosheets.

The dispersions were green coloured, and the broad absorption bands at approximately 1090, 750, 650, and 380 nm were attributed to the d-d electronic transitions of Ni(II) with octahedral coordination (Fig. S7, ESI[†]).⁴² The LNH nanosheets can be easily assembled into large-scale films by drop casting, dip coating, or layer-by-layer techniques with an adjustable thickness. It was also possible to cast the nanosheets into self-standing films by evaporating dense dispersions on a polypropylene plate (Fig. 3C). The UV-Vis absorption spectra of these films had features that were very similar to those observed for dispersions. It indicates that the nanosheet structure is stable during restacking (see XRD below). The films were transparent due to the regular arrangement of the nanosheets, which was also confirmed by SEM images showing the parallel arranged sheets (Fig. S8, ESI[†]). The self-standing films allowed careful manipulations without breakage.

The XRD patterns of drop-casted films prepared from delaminated LNH-lactate (ae), LNH-lactate (p), and LNH-NO₃ (p) showed the basal diffraction lines in the reflection mode (Fig. 4, Fig. S9 and S10, ESI[†]). The nonbasal diffractions located at approximately 34, 60, and 70° (2θ) completely disappeared. The same samples measured in the transmission mode yielded patterns with suppressed basal diffractions and clearly visible nonbasal diffraction peaks that were located at the same positions as in the XRD of the powders (Fig. 1). These measurements demonstrated that the delaminated nickel hydroxide nanosheets retained the original hydroxide structure and that the nanosheets were restacked in a preferential orientation along the support surface. The basal spacings of the restacked films prepared from LNH-lactate (p) and LNH-NO₃ (p) were shifted to smaller angles and broadened when compared with the parent powders, indicating a considerable amount of water in the interlayer space and ill-defined stacking of the nanosheets. In contrast, the film prepared from delaminated LNH-lactate (ae) exhibited high crystallinity and a basal spacing of 10.5 Å, which was also found for the crystalline powder (Fig. 1b and 4). Based on these results, LNH-lactate (ae) was selected as the most suitable material for the preparation of highly oriented films for further electrochemical studies.

The XRD patterns of LNH-lactate (ae) self-standing films (Fig. S11, ESI[†]) were similar to those of the drop-casted films. The intensive basal diffraction at 11.0 Å in the reflection mode

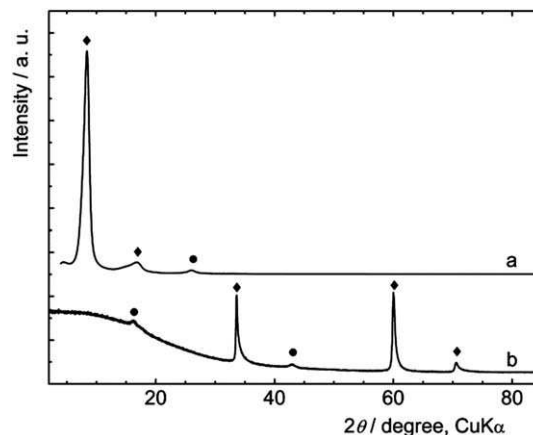


Fig. 4 XRD patterns of the film prepared from delaminated LNH-lactate (ae): (a) in the reflection mode; (b) in the transmission mode. The diffractions of LNH-lactate (ae) (◆) and the Mylar foil support (●) are labelled. The diffractograms are vertically shifted to avoid overlaps.

and the nonbasal diffractions detected only in the transmission mode indicate that the self-standing films had a unified orientation of the restacked nanosheets.

3.4 Morphology of the nanosheets

The size and shape of the nanosized particles in the dispersions were analysed using SAXS experiments. The obtained scattering curves were typical for planar particles, as shown in Fig. S12 (see ESI[†]) for the LNH-lactate (ae) dispersions. The concentration independence of the curves after normalisation to unit concentration indicates the absence of structural factor effects.

The thickness and diameter of the particles were obtained by fitting the corrected SAXS curves with the scattering function derived for planar particles of homogeneous cross-sections. The particles were assumed to be monodisperse in diameter with a thickness characterised by the Schulz-Zimm distribution.^{43,44} The analysis was also performed using the normalised thickness factor of a lamellar particle extrapolated to $q = 0$. Both approaches led to very similar results. The obtained diameters varied between 50 and 80 nm for all dispersions. In contrast to the diameters, the thickness of the particles was evidently affected by the preparation procedure. The LNH-lactate (ae) and LNH-lactate (p) particles were found to be very thin (<1 nm), whereas the thickness of the LNH-NO₃ (p) particles had a broad distribution from 3 to 6 nm. The differences in the thickness were visualised by casting the data into the Iq^2c^{-1} vs. q graph (c is the particle concentration) showing that the thin lactate-derived particles exhibit a flat thickness factor, whereas the relatively thick particles of LNH-NO₃ (p) exhibit a strong dependence (Fig. 5). These results indicate that the delaminated particles consisted of nanosheets with large aspect ratios.

The nanosheet morphology was also preserved in highly concentrated viscous gels. The increase of the thickness factor for $q < 0.2 \text{ \AA}^{-1}$ in Fig. 5 indicated that the thickness of the nanosheets was larger than 1 nm. In accordance, the curve fitting analysis afforded a diameter and thickness of 72 nm and approximately 2 nm, respectively. The latter value well

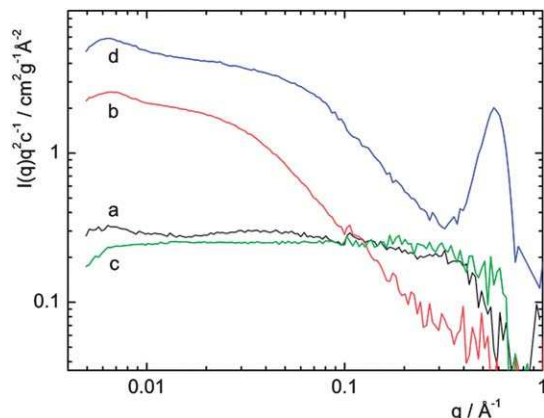


Fig. 5 Thickness factors of the nanosheets dispersed in water: (a) LNH–lactate (p); (b) LNH–NO₃ (p); (c) LNH–lactate (ae), all 4 mg mL⁻¹; (d) LNH–lactate (ae) gel (40 mg mL⁻¹).

correlates with the thickness of 4 nm obtained from the broadening of the correlation peak at $q = 0.57 \text{ \AA}^{-1}$ using the Scherrer equation. The thickness and location of the correlation peak corresponding to a basal spacing of 11 Å showed that the nanosheets in these dense dispersions were composed of two to four stacked nickel hydroxide layers with lactate anions in the interlayer space.

We employed tapping mode-AFM to study the topographic morphology of the pertinent nanosheets. The deposited LNH–lactate (p) nanosheets showed single nanolamellar units and their aggregates lying flat on a mica support (Fig. 6, S13 and S14 in ESI†). In both cases, the thickness was approximately 1 nm as followed from profile analyses (Fig. 6) and height distribution statistics (Fig. S15, ESI†). It documents a preference of the single units in the two-dimensional growth. Similar to the LNH–lactate (p) nanosheets, the nanosheets prepared from LNH–lactate (ae) exhibited single units with a thickness of approximately 1 nm (Fig. 7). The dendrite-like aggregates were extended

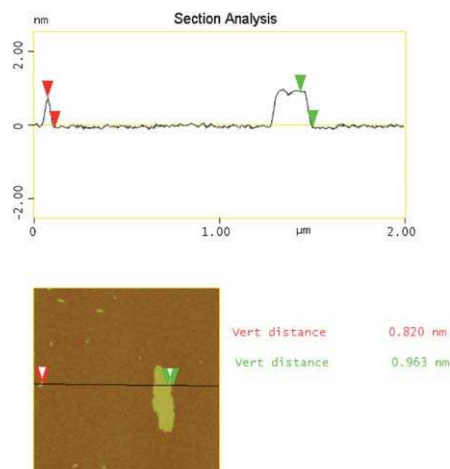


Fig. 6 Profile analysis of the LNH–lactate (p) nanoparticles imaged by tapping-mode AFM. The figure shows that the heights of both the nanolamellar units (red marks, left) and their two-dimensional aggregates (green marks, right) are the same.

over large areas of up to several μm^2 . The height distribution maximum for the LNH–lactate (ae) aggregates was approximately 1 nm and this maximum was accompanied by the occurrence of heights of about 2.5 nm (Fig. S16, ESI†). It indicates prevailing two-dimensional (single layer) aggregation with approximately a 10% fraction of more stacked hydroxide layers. In the case of LNH–NO₃ (p), the height of the single units was approximately 0.8 nm. The aggregates with large lateral dimensions (approximately $10 \mu\text{m}^2$) showed a height of 1.3 nm and a pinhole structure (Fig. S17, ESI†). Similar to LNH–lactate (ae), the results on the aggregates indicated the stacking of at least two single nickel hydroxide nanosheets.

The nanosheets correspond to single nickel hydroxide layers with nickel atoms arranged in the central plane octahedrally surrounded by the hydroxide groups and the anions. The presented AFM results, in agreement with the SAXS data, revealed that the hydroxide nanosheets possess integrity and the sheet morphology in both the dispersions and the oriented films. The measured thickness of a single layer was approximately 1 nm and certain spread and scaling up of the height values, obtained by AFM, can be attributed to local differences in layer-to-layer compactness and to anion/solvent-hydroxide layer interactions. For comparison, the thickness of nanosheets obtained by the delamination of LDHs was reported to be in the range 0.8–0.9 nm.⁴⁵

The TEM and high-resolution TEM observations of LNH–lactate (p) and LNH–lactate (ae) nanosheets resulted in fast decomposition of the nanosheets to metallic nickel nanoparticles. As both nanosheets displayed similar sizes and shapes in AFM and SAXS measurements, we focused only on the nanosheets prepared from LNH–lactate (ae) and the pertinent information was obtained using protected samples (Fig. 8A). The LNH–lactate (ae) nanosheets were approximately 100 nm in size with strong shape anisotropy, in agreement with the SAXS and AFM data. Larger particles likely corresponded to aggregates.

The observation of the central part of a large nanoparticle indicated the apparent polycrystalline character of the

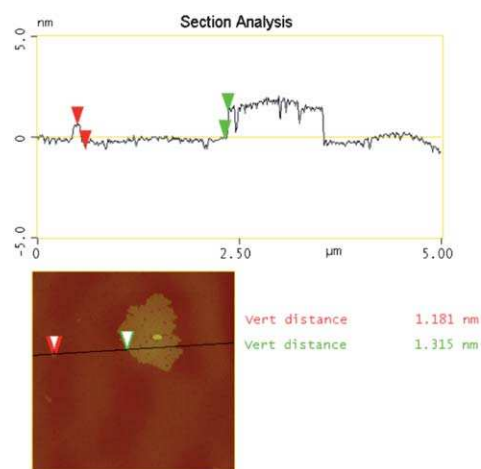


Fig. 7 Profile analysis of the LNH–lactate (ae) nanoparticles imaged by tapping-mode AFM. The aggregates (right) had a high preference for a two-dimensional growth.

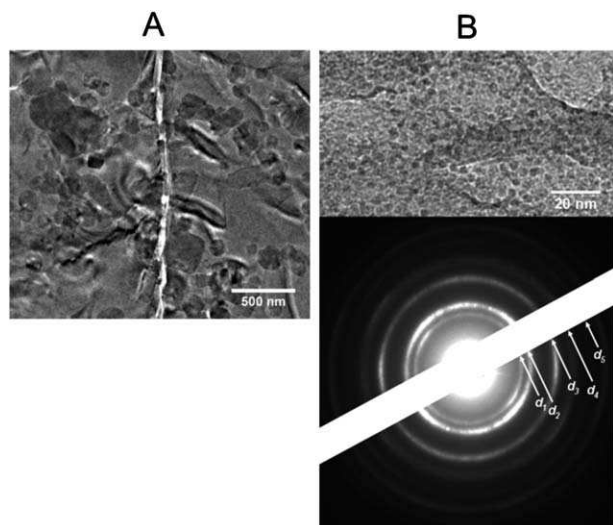


Fig. 8 (A) TEM image of several LNH-lactate (ae) nanosheets. (B) TEM image taken on the central part of one of the LNH-lactate (ae) nanosheets and the corresponding SAED pattern ($d_1 = 2.45 \pm 0.05 \text{ \AA}$, $d_2 = 2.10 \pm 0.05 \text{ \AA}$, $d_3 = 1.50 \pm 0.05 \text{ \AA}$, $d_4 = 1.30 \pm 0.05 \text{ \AA}$, $d_5 = 1.20 \pm 0.05 \text{ \AA}$). The dispersion was deposited on a microscope grid, frozen in liquid nitrogen, and trapped in ethane to protect the sample.

nanoparticles. Each nanosheet appeared to consist of several monocrystals with a mean size of approximately 5 nm and a random orientation (Fig. 8B), which is contradictory to the relatively sharp XRD diffractions (Fig. 1b). In addition, the distances measured using SAED and FFT patterns (Fig. S18, ESI†) correspond to nickel oxide (JCPDS-00-001-1239) and nickel oxide hydroxide (JCPDS-00-040-1179), which suggests a partial degradation of the nanosheets under the electron beam despite the ethane protection. This finding was further confirmed by the observation of small particles (2 to 5 nm in diameter) in the region of a thinner water droplet. These particles were not observed by SAXS or AFM and most likely resulted from the partial degradation of large nanosheets under the electron beam.

The LNH-NO₃ (p) nanosheets were much more stable under the electron beam, and their observation did not require the use of the ethane covering. The nanosheets were visible as well-defined hexagonal plates, with a lateral size distribution between 50 and 90 nm in good agreement with the SAXS and AFM data (Fig. 9A). High-resolution TEM observations of LNH-NO₃ (p) nanosheets showed discontinuous atomic planes within the nanosheets that were all oriented in the same direction, indicating the monocrystalline nature of the nanosheets (Fig. 9B and S19 in ESI†). The discontinuities of the atomic planes are likely due to the partial degradation of the upper layer under the electron beam. The SAED (Fig. S19, ESI†) and FFT patterns revealed planes at 2.50, 1.50, 1.45, and 1.27 Å, comparable to nonbasal XRD.

3.5 Nanomorphology and electrochemical properties of the nickel hydroxide films

Ex situ AFM images of drop-casted and spin-coated films deposited from aqueous dispersions of the LNH-lactate (ae)

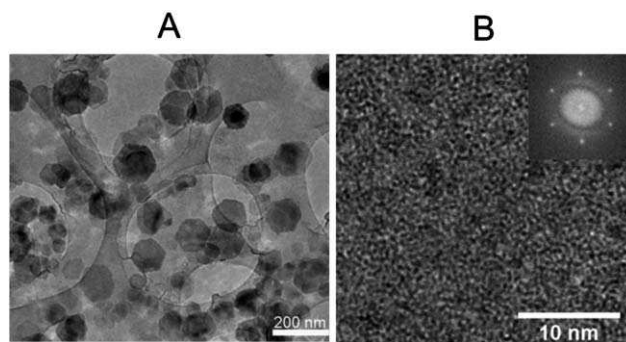


Fig. 9 (A) TEM image of LNH-NO₃ (p) showing a representative area of the carbon membrane supporting the nanosheets. (B) High-resolution image acquired for one of the nanoparticles and its corresponding FFT pattern, showing the monocrystalline character of the analysed area.

nanosheets on the basal plane of HOPG showed relatively uniform and homogeneous surfaces with no resolved nanostructures (Fig. 10A). Typically, the surface nanomorphology of the films had a low corrugation with surface roughness parameters of $\sim 6 \text{ nm}$ (R_a) and $\sim 70 \text{ nm}$ (R_{max}).

Repetitive voltammetric scanning of the nickel hydroxide films in the aqueous 1 M KOH electrolyte indicated a substantial rearrangement inside the films (Fig. 10B) that was manifested as a significant increase in the charge-transfer efficiency (Fig. 11). Indeed, the significant stepwise increase of peak currents and simultaneous peak narrowing showed the large increase in the ionic conductivity of the film, presumably resulting from the insertion of charge-compensating ions from solution. It is obvious that the transfer of the electron is reversible. The anodic peak is due to the oxidation of $\alpha\text{-Ni(OH)}_2$ to nickel oxyhydroxide (NiOOH), and the cathodic peak is attributed to the reverse process, both at the interface of $\alpha\text{-Ni(OH)}_2$ and the electrolyte (eqn (1)).⁴⁶ These peaks correspond to the conversion between different oxidation states of Ni according to the general scheme⁴⁷

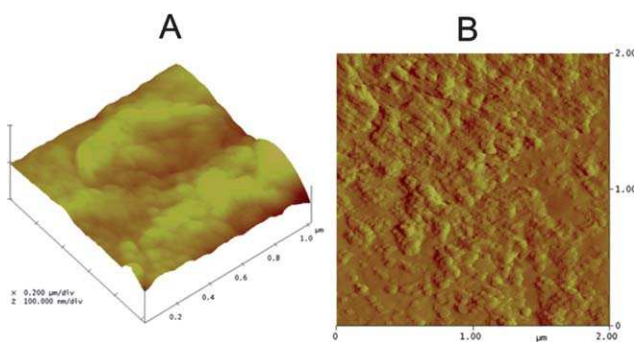


Fig. 10 (A) AFM topography (tapping) image of a nickel hydroxide film drop-casted on HOPG from an aqueous dispersion of the LNH-lactate (ae) nanosheets and (B) after repetitive potential cycling (50 cycles from -150 mV to $+500 \text{ mV}$ vs. SCE reference electrode) in aqueous 1 M KOH solution. The columnar stacking of lamellae after potential sweeping is well resolved.

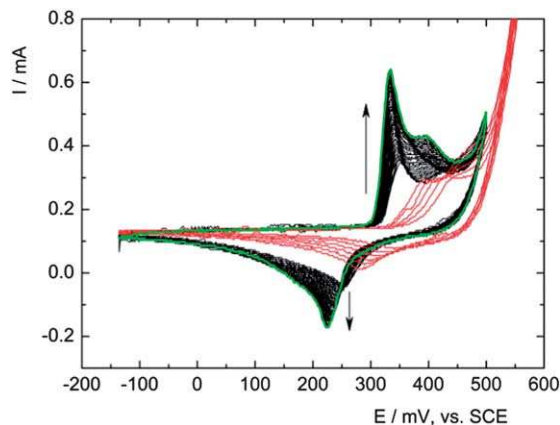


Fig. 11 Repetitive potential cycling of a spin-coated HOPG electrode with the LNH-lactate (ae) nanosheets in aqueous 1 M KOH solution deoxygenated by Ar. The scan rate was 100 mV s^{-1} . The voltammogram shows the first five cycles (red curves) and continuous cycling (50 cycles) until a steady state is reached (green curve). Vertical arrows indicate the development of current peaks during cycling.



The increase in ionic conductivity was accompanied by changes in the nanomorphology of the films recorded after repetitive potential cycling. The surface ordering and the appearance of stacked columnar nanostructures indicated an aggregation of the nickel hydroxide nanoplatelets accompanying the repetitive charge-transfer $\text{NiOOH}/\text{Ni(OH)}_2$ reaction (Fig. 10B). These morphological changes are common for $\alpha\text{-Ni(OH)}_2$ and can be caused by a slow replacement of the intercalated anions by the hydroxide groups in the alkaline electrolyte. These changes are usually accompanied by the contraction of the interlayer distance.^{24,25} A second oxidation peak at approximately 400 mV vs. SCE appeared during repetitive potential cycling (Fig. 11) and indicated the occurrence of the reaction, described by eqn (2), taking place within the volume of the film. The reaction may lead to compositionally resolved layered nanostructures, often found at bulk Ni electrodes,^{46,47} whereas monolayers and sub-monolayers did not show such composition splitting.²⁶

The dependence of the peak current on the potential sweep rate ν (studied using sweep rates of $10\text{--}100 \text{ mV s}^{-1}$) followed the $\nu^{1/2}$ linear course up to a rate of 50 mV s^{-1} , whereas faster potential sweeps led to a downward curvature of the scan rate dependence. The second characteristic, the peak-to-peak potential separation, changed mostly due to the shift of the anodic peak to more positive potentials with increasing scan rates. The peak-to-peak separation can be caused by differences in the ionic resistivity of the film, as is common for the oxide-based deposits, because the mobility of charge-compensating ions within the oxide/hydroxide layer depends on the form present at potential sweeping and because an increasing IR drop causes an additional potential shift towards higher potentials. Thus, charge mobility in the films becomes the rate-determining step and imposes surface reaction kinetics with pseudo-solution character. As a result, the charge-transfer

efficiency decreased by approximately 50% as the potential sweep rate increased from 10 to 100 mV s^{-1} .

Interestingly, the size of the intercalated anions in $\alpha\text{-Ni(OH)}_2$ was reported to affect the charge mobility in the films.²¹ The charge-transfer efficiency decreased for the intercalated anions in the order of $\text{Cl}^- > \text{NO}_3^- > \text{OAc}^- > \text{SO}_4^{2-}$ and the largest SO_4^{2-} anions decreased the charge capacity of the film most considerably. In our case, no effects of intercalated lactate and nitrate anions in the films prepared from LNH-lactate (ae) and LNH- NO_3 (p) nanosheets were observed.

Bulk films of $\alpha\text{-Ni(OH)}_2$ were reported to be unstable in alkaline solutions due to their transformation to $\beta\text{-Ni(OH)}_2$ and intermediate phases under potential cycling. The transformation is accompanied by a gradual decrease in charge capacity and electrochemical reversibility.²⁵ To keep the charge-transfer efficiency, the desired stability of $\alpha\text{-Ni(OH)}_2$ during cycling can be achieved by metal doping.^{25,48} In the case of the presented films, the transformation to $\beta\text{-Ni(OH)}_2$ was not indicated either by XRD or by the loss of the redox process efficiency during cyclic voltammetry experiments. The behaviour of the oriented films presented here is advantageous because the steady state of the oxidation/reduction process is reached rapidly and because the films are stable during repetitive potential sweeping.

4 Conclusions

For the first time, we successfully delaminated layered nickel hydroxides and obtained stable nanosheet dispersions in water. The delaminated nickel hydroxide nanosheets retained the original hydroxide structure and could be deliberately re-assembled in the form of transparent and oriented thin/ultra-thin films keeping the layered structure of $\alpha\text{-Ni(OH)}_2$ with intercalated interlayer anions. This work shows that delamination of layered nickel hydroxides and re-stacking of the nanosheets are feasible methods for the preparation of films with tunable thickness and charge-discharge properties in alkaline electrolyte solutions. The advantages of the presented $\alpha\text{-Ni(OH)}_2$ films are that the steady state of the oxidation/reduction process is reached quickly and that the electrochemically active nanosheets exhibit high stability during potential sweeping. These properties make the nickel hydroxide nanosheets very interesting materials for the design of electrochemical devices with a long cycle life.

Acknowledgements

This work was supported by the Czech Science Foundation (P207/10/1447, 13-09462P). We thank Petr Bezdička for XRD measurements and helpful discussions and Eva Večerníková for DTA measurements.

Notes and references

- 1 D. G. Evans and X. Duan, *Chem. Commun.*, 2006, 485.
- 2 X. Guo, F. Zhang, D. G. Evans and X. Duan, *Chem. Commun.*, 2010, **46**, 5197.

- 3 G. G. C. Arizaga, K. G. Satyanarayana and F. Wypych, *Solid State Ionics*, 2007, **178**, 1143.
- 4 F. Leroux and J. P. Besse, *Chem. Mater.*, 2001, **13**, 3507.
- 5 M. Taibi, S. Ammar, N. Jouini, F. Fiévet, P. Molinié and M. Drillon, *J. Mater. Chem.*, 2002, **12**, 3238.
- 6 G. Rogez, C. Massobrio, P. Rabu and M. Drillon, *Chem. Soc. Rev.*, 2011, **40**, 1031.
- 7 B. F. Sels, D. E. De Vos and P. A. Jacobs, *Catal. Rev.: Sci. Eng.*, 2001, **43**, 443.
- 8 H. Li, D. Zhang, P. Maitarad, L. Shi, R. Gao, J. Zhang and W. Cao, *Chem. Commun.*, 2012, **48**, 10645.
- 9 M. Jiříčková, J. Demel, P. Kubát, J. Hostomský, F. Kovanda and K. Lang, *J. Phys. Chem. C*, 2011, **115**, 21700.
- 10 J. Demel, P. Kubát, I. Jirka, P. Kovář and K. Lang, *J. Phys. Chem. C*, 2010, **114**, 16321.
- 11 J. Demel and K. Lang, *Eur. J. Inorg. Chem.*, 2012, 5154.
- 12 D. Yan, J. Lu, M. Wei, D. G. Evans and X. Duan, *J. Mater. Chem.*, 2011, **21**, 13128.
- 13 C. Sanchez, P. Belleville, M. Popall and L. Nicole, *Chem. Soc. Rev.*, 2011, **40**, 696.
- 14 Q. Wang and D. O'Hare, *Chem. Rev.*, 2012, **112**, 4124.
- 15 S. P. Newman and W. Jones, *J. Solid State Chem.*, 1999, **148**, 26.
- 16 P. Oliva, J. Leonardi, J. F. Laurent, C. Delmas, J. J. Braconnier, M. Figlarz, F. Fievet and A. De Guibert, *J. Power Sources*, 1982, **8**, 229.
- 17 J. Wang, H. Pang, J. Yin, L. Guan, Q. Lu and F. Gao, *CrystEngComm*, 2010, **12**, 1404.
- 18 L. Xu, Y.-S. Ding, C.-H. Chen, L. Zhao, C. Rimkus, R. Joesten and S. L. Suib, *Chem. Mater.*, 2008, **20**, 308.
- 19 M. Winter and R. J. Brodd, *Chem. Rev.*, 2004, **104**, 4245.
- 20 H. Wang, J. Gao, Z. Li, Y. Ge, K. Kan and K. Shi, *CrystEngComm*, 2012, **14**, 6843.
- 21 J. W. Lee, J. M. Ko and J.-D. Kim, *J. Phys. Chem. C*, 2011, **115**, 19445.
- 22 S. Ida, D. Shiga, M. Koinuma and Y. Matsumoto, *J. Am. Chem. Soc.*, 2008, **130**, 14038.
- 23 H. Wang, H. S. Casalongue, Y. Liang and H. Dai, *J. Am. Chem. Soc.*, 2010, **132**, 7472.
- 24 S. Yang, X. Wu, C. Chen, H. Dong, W. Hu and X. Wang, *Chem. Commun.*, 2012, **48**, 2773.
- 25 M. S. Kim and K. B. Kim, *J. Electrochem. Soc.*, 1998, **145**, 507.
- 26 Z. Bastl, J. Franc, P. Janda, H. Pelouchová and Z. Samec, *Nanotechnology*, 2006, **17**, 1492.
- 27 K. Watanabe and T. Kikuoka, *J. Appl. Electrochem.*, 1995, **25**, 219.
- 28 R. Ma and T. Sasaki, *Adv. Mater.*, 2010, **22**, 5082.
- 29 T. Hibino and M. Kobayashi, *J. Mater. Chem.*, 2005, **15**, 653.
- 30 C. Jaubertie, M. J. Holgado, M. S. San Román and V. Rives, *Chem. Mater.*, 2006, **18**, 3114.
- 31 T. Hibino, *Appl. Clay Sci.*, 2011, **54**, 83.
- 32 N. Iyi, Y. Ebina and T. Sasaki, *Langmuir*, 2008, **24**, 5591.
- 33 N. Iyi, Y. Ebina and T. Sasaki, *J. Mater. Chem.*, 2011, **21**, 8085.
- 34 J. Demel, J. Pleštil, P. Bezdička, P. Janda, M. Klementová and K. Lang, *J. Colloid Interface Sci.*, 2011, **360**, 532.
- 35 JCPDS PDF-2 database, International Centre for Diffraction Data, Newtown Square, PA, U.S.A. release 54, 2004.
- 36 D. Orthaber, A. Bergmann and J. O. Glatter, *J. Appl. Crystallogr.*, 2000, **33**, 218.
- 37 M. Rajamathi, P. V. Kamath and R. Seshadri, *J. Mater. Chem.*, 2000, **10**, 503.
- 38 M. Y. Cheng and B. J. Hwang, *J. Colloid Interface Sci.*, 2009, **337**, 265.
- 39 E. L. Crepaldi, P. C. Pavan and J. B. Valim, *Chem. Commun.*, 1999, 155.
- 40 K. Nakamoto, *Infrared and Raman Spectra of Inorganic and Coordination Compounds*, Wiley, New York, 4th edn, 1986, pp. 231–233.
- 41 R. M. Silverstein, G. C. Bassler and T. C. Morrill, *Spectrometric identification of organic compounds*, Wiley, New York, 5th edn, 1991, p. 111.
- 42 L. Poul, N. Jouini and F. Fiévet, *Chem. Mater.*, 2000, **12**, 3123.
- 43 G. V. Schulz, *Z. Phys. Chem., Abt. B*, 1939, **43**, 25.
- 44 B. H. Zimm, *J. Chem. Phys.*, 1948, **16**, 1093.
- 45 K. Okamoto, T. Sasaki, T. Fujita and N. Iyi, *J. Mater. Chem.*, 2006, **16**, 1608.
- 46 A. Seghioer, J. Chevalet, A. Barhoun and F. Lantelme, *J. Electroanal. Chem.*, 1998, **442**, 113.
- 47 P. Häring and R. Kötz, *J. Electroanal. Chem.*, 1995, **385**, 273.
- 48 W. K. Hu and D. Noréus, *Chem. Mater.*, 2003, **15**, 974.

ELECTRONIC SUPPLEMENTARY INFORMATION

Nickel hydroxide ultrathin nanosheets as building blocks for electrochemically active layers

Barbora Schneiderová,^{a,b} Jan Demel,^a Josef Pleštil,^c Pavel Janda,^d Jan Bohuslav,^{d,e} Dris Ihiwakrim,^f Ovidiu Ersen,^f Guillaume Rogez,^f and Kamil Lang*^a

^a Institute of Inorganic Chemistry of the AS CR, v. v. i., Husinec-Řež 1001, 250 68 Řež, Czech Republic, lang@iic.cas.cz

^b Faculty of Science, Charles University in Prague, Hlavova 2030, 128 43 Praha 2, Czech Republic

^c Institute of Macromolecular Chemistry of the AS CR, v. v. i., Heyrovského nám. 2, 162 06 Praha 6, Czech Republic

^d J. Heyrovský Institute of Physical Chemistry of the AS CR, v. v. i., Dolejškova 3, 182 23 Praha 8, Czech Republic

^e Institute of Chemical Technology, Prague, Technická 5, 166 28 Praha 6, Czech Republic

^f Institut de Physique et Chimie des Matériaux de Strasbourg, UMR CNRS-UdS 7504, 23 rue du Loess, BP 43, 67034 Strasbourg Cedex 2, France

*Corresponding author: Email address: lang@iic.cas.cz, Tel: +420 26617 2193. Fax: +420 22094 1502.

Contents

Syntheses

Voltammetric experiments

Table S1. Elemental analyses of the prepared LNHs.

Figures S1-S4. TGA/DTA/MS curves and the evolution of gases for LNH-Lactate(p), LNH-Lactate(ae), LNH-NO₃(p), and LNH-NO₃(ae).

Figure S5. Powder XRD patterns of LNH-DS.

Figure S6. FTIR spectrum of LNH-DS.

Figure S7. UV-Vis spectra of the LNH-Lac(ae) colloid and the self-standing film.

Figure S8. SEM image of the LNH-Lac(ae) self-standing film.

Figures S9-S10. XRD patterns of the restacked layers.

Figure S11. XRD patterns of the LNH-Lactate(ae) self-standing film.

Figure S12. SAXS curves of LNH-Lactate(ae) aqueous dispersions.

Figures S13-S17. AFM images.

Figure S18. HR-TEM image at the centre of a LNH-Lactate(ae) nanosheet and the computed FFT pattern.

Figure S19. HR-TEM image of the LNH-NO₃(p) nanosheets with the corresponding SAED pattern.

Syntheses

Nickel lactate. 6.8 mL (22 mmol) of 60 % solution of sodium lactate was added to 20 mL of 1 M solution of nickel chloride. The mixture was stirred at 60 °C for 1 hour. The green precipitate was filtrated and washed three times with water and twice with acetone. The product was air-dried at room temperature and used directly for the syntheses of LNHs.

Layered nickel hydroxide dodecyl sulphate salt (LNH-DS). 1.45 g (5 mmol) of $\text{Ni}(\text{NO}_3)_2 \cdot 6\text{H}_2\text{O}$, 5.77 g (20 mmol) of SDS, and 7.01 g (50 mmol) of HMT were dissolved in a mixture of deionised water (90 mL) and 1-butanol (10 mL) and heated to 90 °C for 2 hours. The green precipitate was filtrated, washed three times with water and acetone, and air-dried. The elemental and thermogravimetric analyses confirmed the chemical composition (Table S1).

Voltammetric experiments

Electrochemical experiments were performed using a computer-controlled potentiostat (Wenking POS2, Bank Elektronik, Germany) in a three-electrode arrangement. A low-volume electrochemical cell utilized the basal plane HOPG support for the film layers as a working electrode; a platinum wire and a saturated calomel electrode served as a counter and a reference electrode, respectively. Cyclic voltammetry was performed in aqueous (purified by Milli-Q system Gradient, Millipore, resistivity 18.2 M Ω cm) solution of 1M KOH as electrolyte, deoxygenated by argon.

Table S1 Elemental analyses of the prepared LNHs. The values in parenthesis were calculated using the formula $\text{Ni}_2(\text{OH})_3\text{A}\cdot m\text{H}_2\text{O}$.

LNHs	Elemental analysis / %			Water content ^a %, [m]	Mass loss %
	C	H	N		
LNH-DS	26.82 (30.67)	5.74 (6.88)	2.28 (0)	7.0 (7.9) [2]	58.6 (65.7)
LNH-Lactate(p) ^b	7.81 (7.81)	2.33 (2.98)	0 (0)	13.1 (12.3) [2]	38.1 (37.2)
LNH-Lactate(ae)	12.58 (13.08)	3.06 (3.67)	2.55 (0)	7.7 (6.5) [1]	40.3 (49.1)
LNH-NO ₃ (p) ^c	1.82 (0)	1.83 (2.11)	1.69 (2.82)	6.8 (7.3) [1]	31.6 (29.6)
LNH-NO ₃ (ae)	8.45 (0)	2.22 (2.83)	5.06 (5.64)	7.9 (7.3) [1]	41.2 (39.9)

^a The content of water was determined using DTA/DTG analysis, m is the number of water molecules. ^b Assuming 40 % $\beta\text{-Ni}(\text{OH})_2$. ^c Assuming 50 % $\beta\text{-Ni}(\text{OH})_2$.

Figure S1. TGA/DTA/MS curves and the evolution of gases for LNH-Lactate(p).

The measurements were performed in a synthetic air atmosphere (flow rate 30 mL min⁻¹) from 30 to 1050 °C with a heating rate of 5 °C min⁻¹.

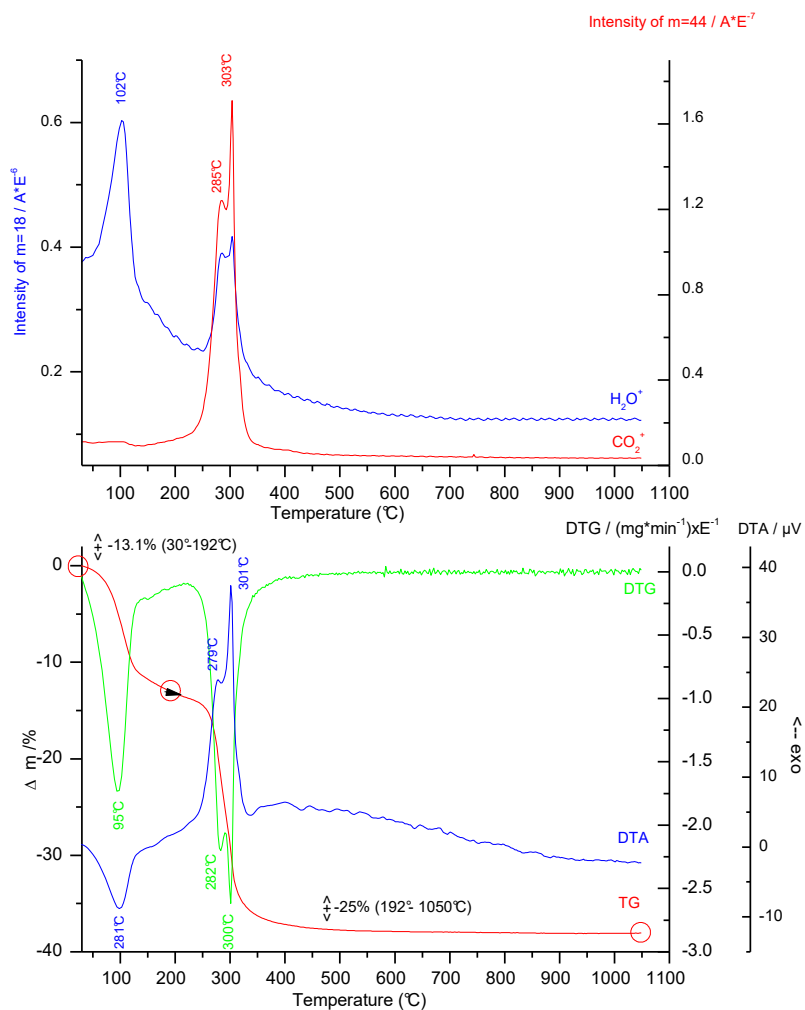


Figure S2. TGA/DTA/MS curves and the evolution of gases for LNH-Lactate(ae).

The measurements were performed in a synthetic air atmosphere (flow rate 30 mL min⁻¹) from 30 to 1050 °C with a heating rate of 5 °C min⁻¹.

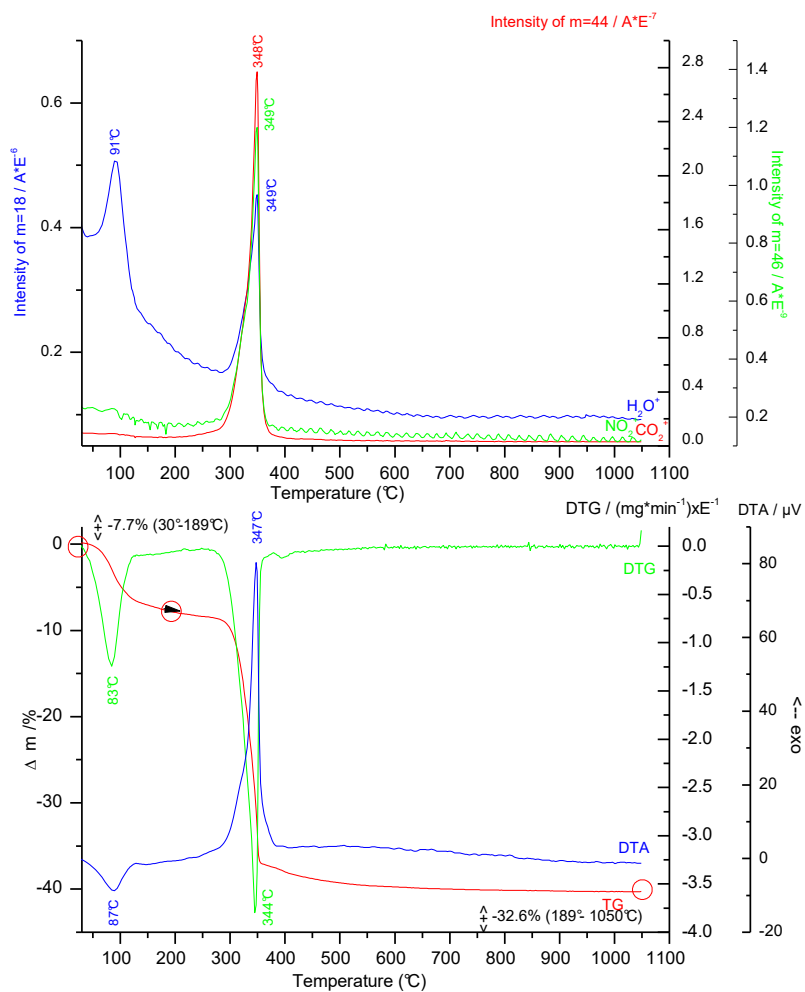


Figure S3. TGA/DTA/MS curves and the evolution of gases for LNH-NO₃(p).

The measurements were performed in a synthetic air atmosphere (flow rate 30 mL min⁻¹) from 30 to 1050 °C with a heating rate of 5 °C min⁻¹.

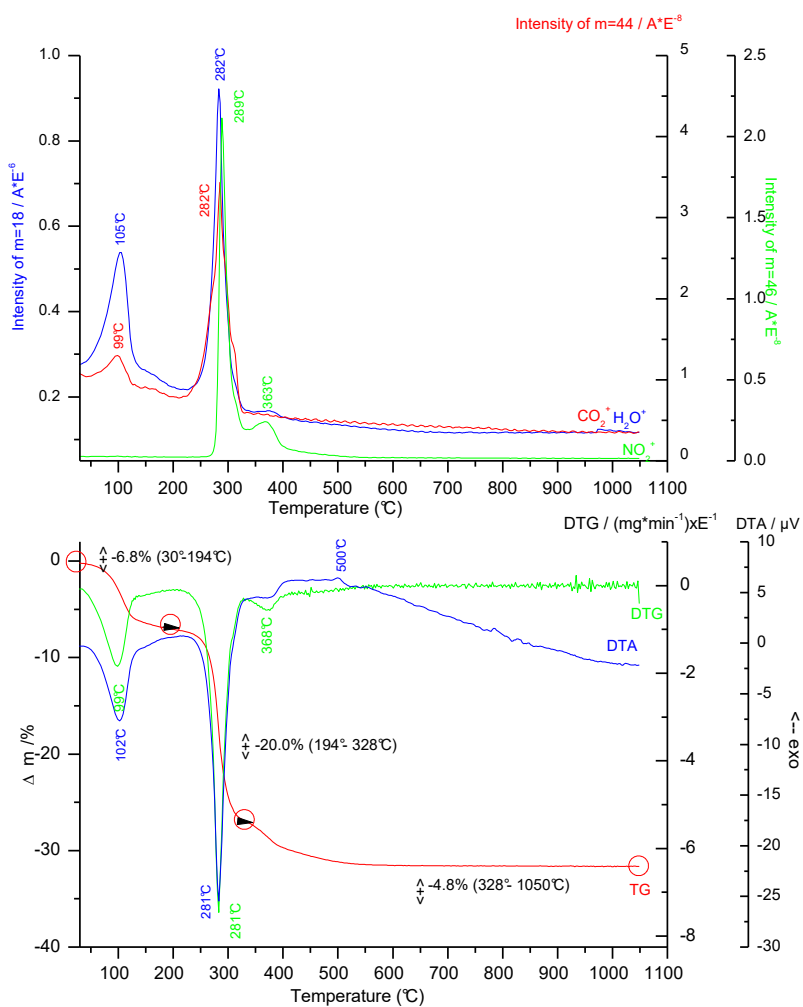


Figure S4. TGA/DTA/MS curves and the evolution of gases for LNH-NO₃(ae).

The measurements were performed in a synthetic air atmosphere (flow rate 30 mL min⁻¹) from 30 to 1050 °C with a heating rate of 5 °C min⁻¹.

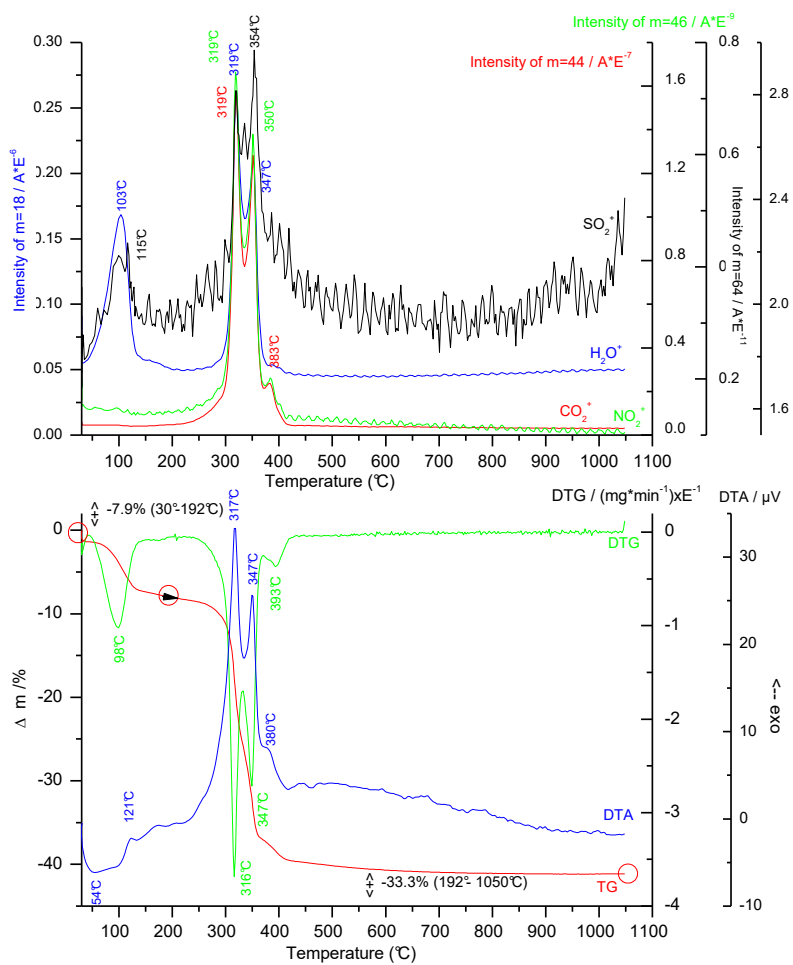


Figure S5. Powder XRD patterns of LNH-DS measured in the transmission mode. The diffraction peak of the Mylar foil support is labelled (●).

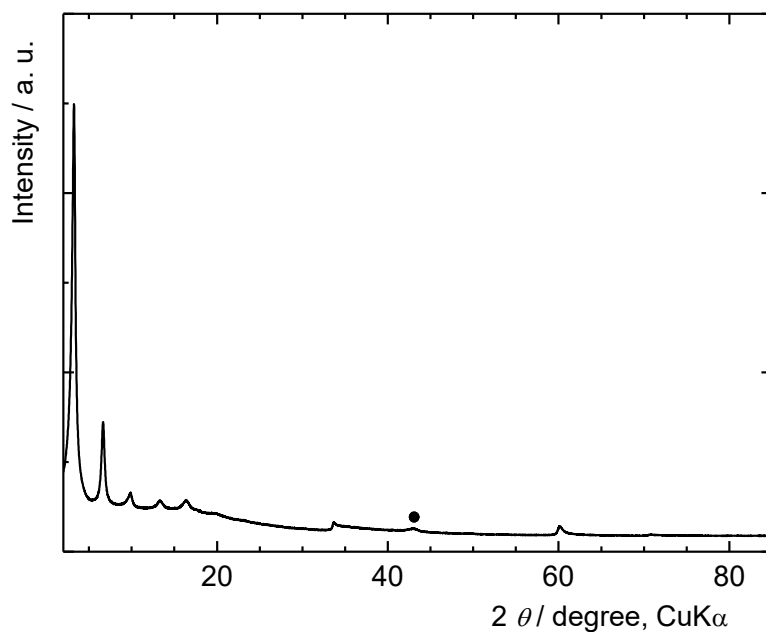


Figure S6. FTIR spectrum of LNH-DS: (a) Broad band between 3750 - 3100 cm^{-1} is due to the stretching vibrations of hydroxyl groups. (b) Sharp bands at 2956, 2924, and 2854 cm^{-1} arise from the C-H stretching vibrations of the dodecyl chain. (c) Peak at 1635 cm^{-1} corresponds to the $\delta(\text{H}_2\text{O})$ vibrations. (d) Peak at 1468 cm^{-1} is caused by the bending vibrations of the CH_2 groups. (f, g) 1193 and 1055 cm^{-1} peaks arise from the stretching vibrations of the SO_3 groups. These peaks together with the peak at 980 cm^{-1} (h) obscure three peaks of HMT, which is present as an impurity. (e) Peak at 1340 cm^{-1} belongs to HMT.

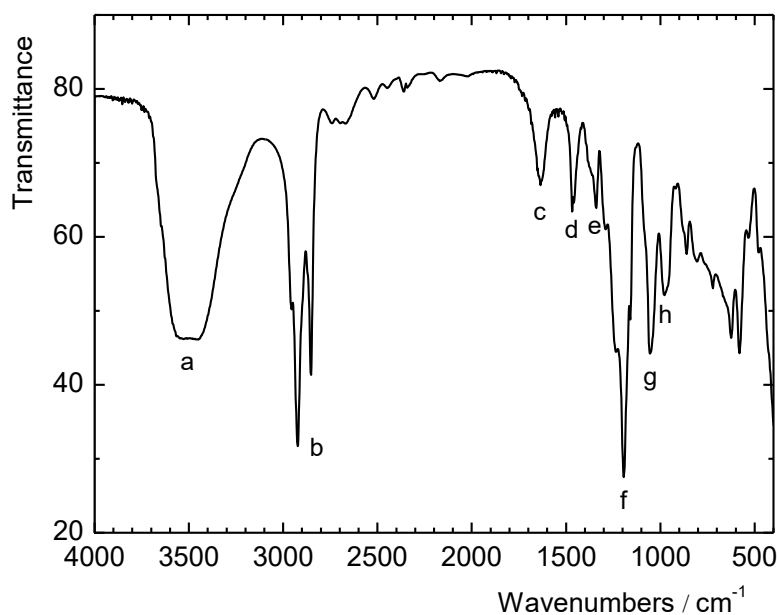


Figure S7. UV-Vis absorption spectra of the LNH-Lactate(ae) dispersion (a, red curve) and the self-standing film (b, black curve).

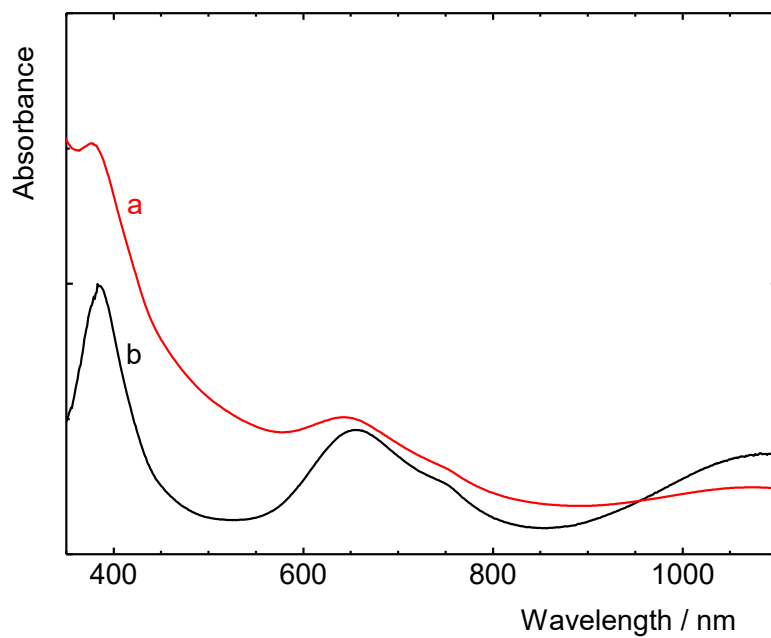


Figure S8. SEM image of the LNH-Lactate(ae) self-standing film.

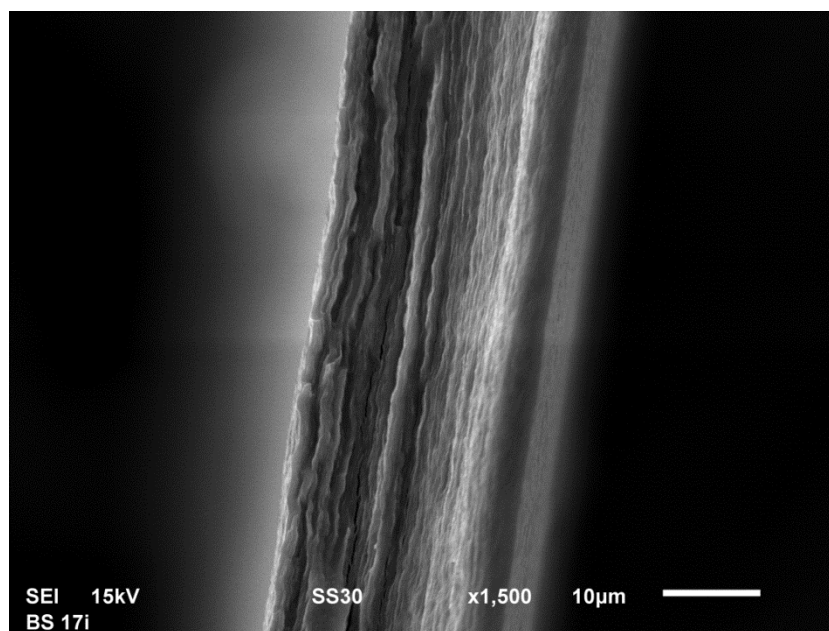


Figure S9. XRD patterns of the film prepared from delaminated LNH-Lactate(p) measured in the reflection (a) and transmission (b) modes. The diffractions of LNH-Lactate(p) (◆), β -Ni(OH)₂ (▲), and the Mylar foil support (●) are labelled. The diffractograms are vertically shifted to avoid overlaps.

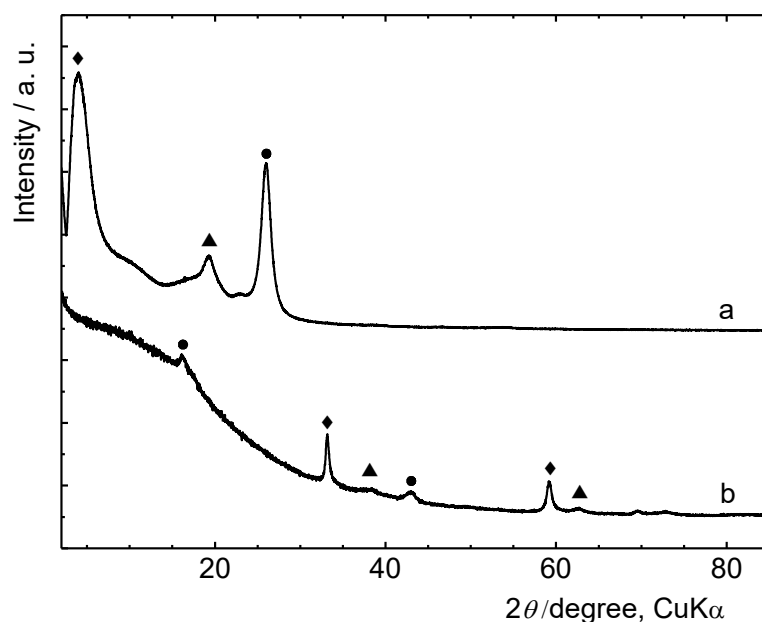


Figure S10. XRD patterns of the film prepared from delaminated LNH-NO₃(p) measured in the reflection (a) and transmission (b) modes. The diffractions of LNH-NO₃(p) (◆), β -Ni(OH)₂ (▲), and the Mylar foil support (●) are labelled. The diffractograms are vertically shifted to avoid overlaps.

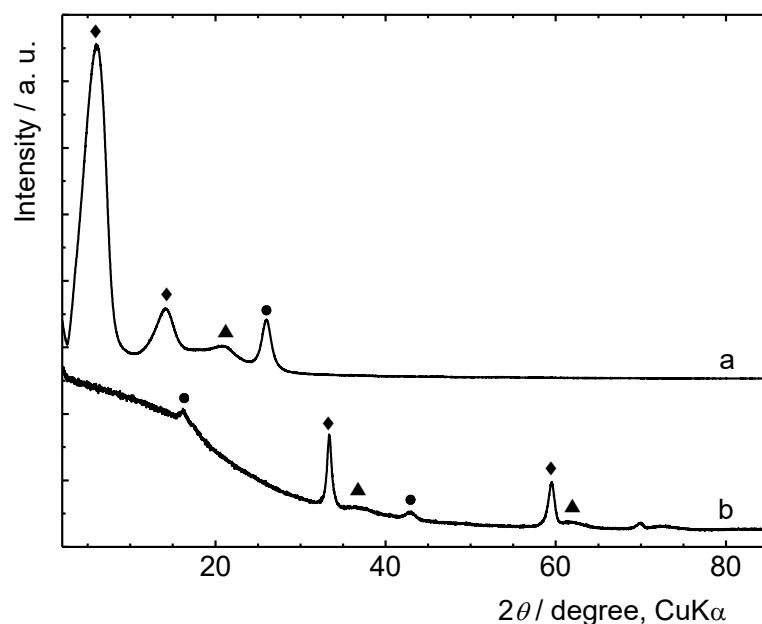


Figure S11. XRD patterns of the LNH-Lactate(ae) self-standing film in the reflection (a) and transmission (b) modes. The diffractions of LNH-Lactate(ae) (◆) and the Mylar foil support (●) are labelled. The diffractograms are vertically shifted to avoid overlaps.

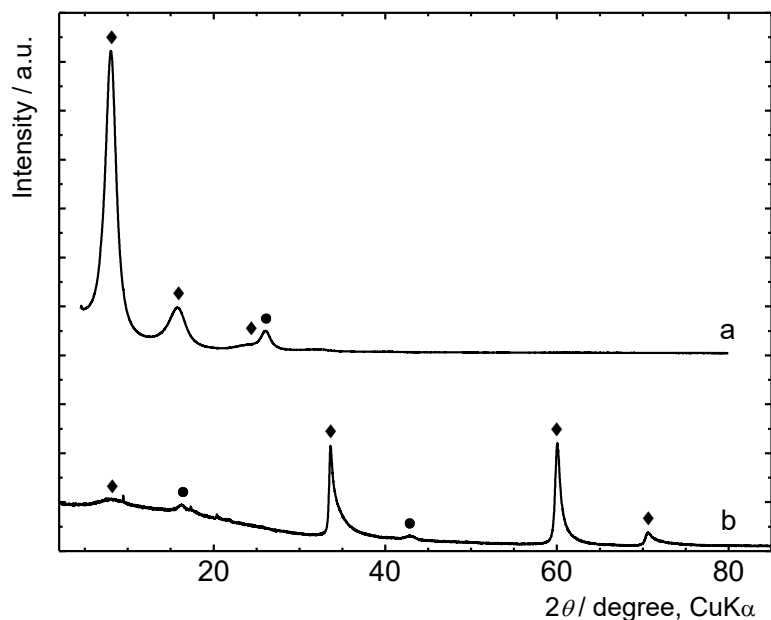


Figure S12. SAXS curves of LNH-Lactate(ae) aqueous dispersions at various concentrations: (a) 1 g L^{-1} ; (b) 2 g L^{-1} ; (c) 4 g L^{-1} . The tails of the curves for $q > 0.5 \text{ \AA}^{-1}$ obtained for various concentrations coincided, which suggest that the scattering contribution of the particles in this region can be neglected and that the measured intensity can be ascribed to scattering from the solvent.

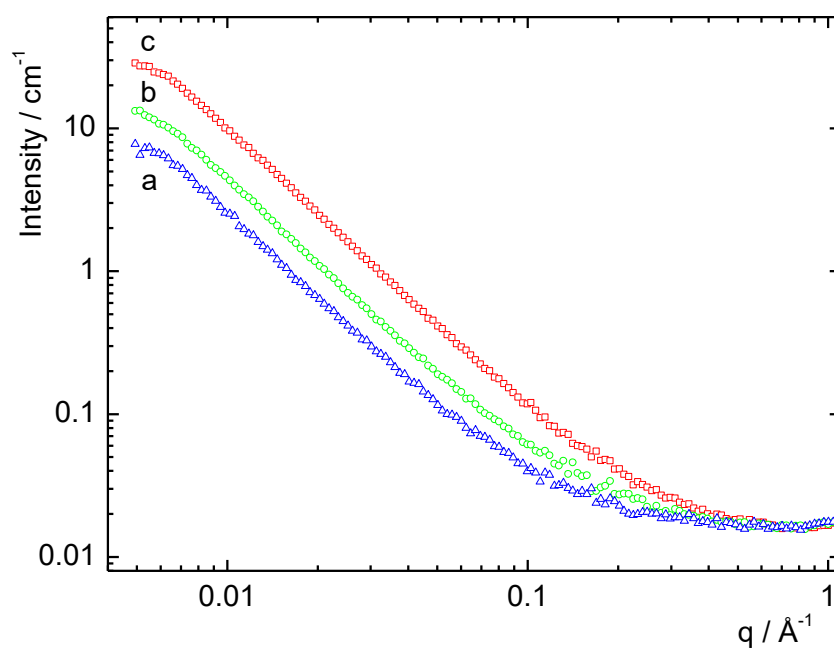


Figure S13. AFM image of LNH-Lactate(p) nanolamellar units (blue circle) and their prevailing 2D-aggregates (red circle) deposited by spin coating on a mica substrate.

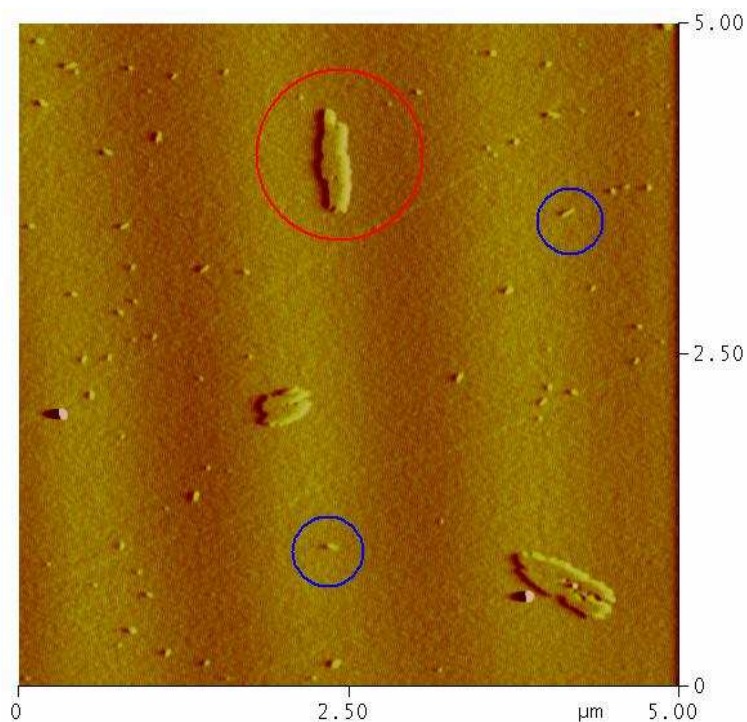


Figure S14. Profile analysis of the lateral size of LNH-Lactate(p) lamellar aggregates spin coated on a mica support. The height profiles revealed that both the nanolamellar units (left) and their aggregates (right) have almost identical thickness (~ 1 nm).

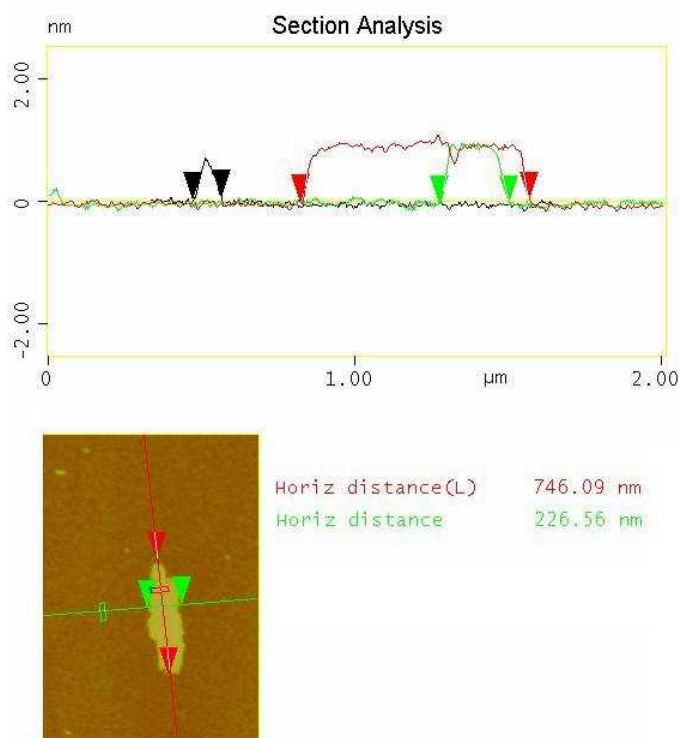


Figure S15. Maximum height (Z_{\max}) distribution curve (right, black dots) of the area covered by the LNH-Lactate(p) single units shows a maximum close to 1 nm. The best fit curve is shown in red (Gaussian). The plotted height data were acquired from AFM-imaged topography (left).

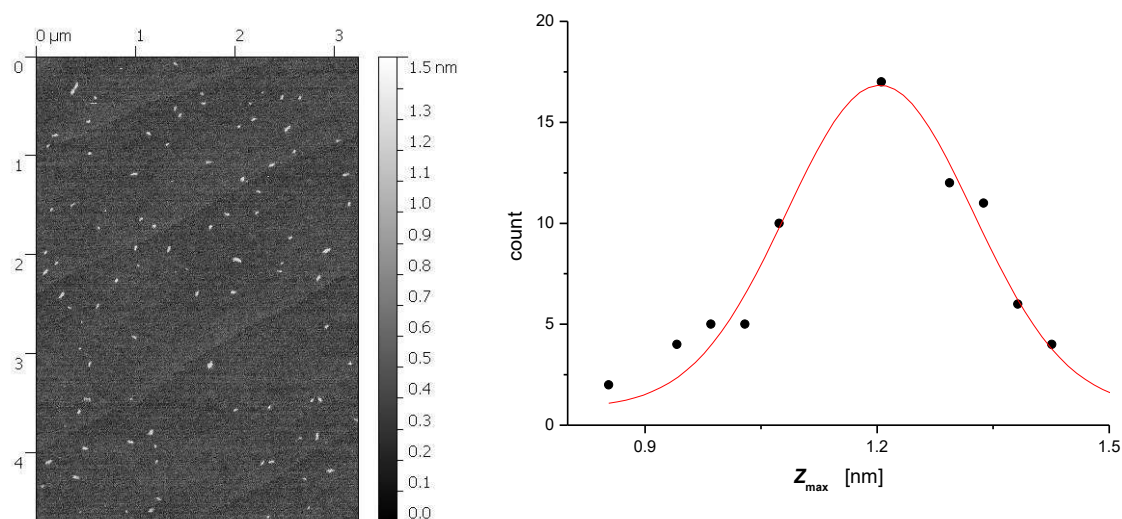


Figure S16. Height (Z) density distribution (σ) curve (right) measured on a LNH-Lactate(ae) deposit indicates a preferable single-layer (2D) growth, (Z maximum is close to 1 nm). A maximum Z approximately at 2.5-2.8 nm can be assigned to more stacked hydroxide layers (it is approximately a 10% fraction of the aggregate). The plotted height data (right) were acquired from AFM-imaged topography (left).

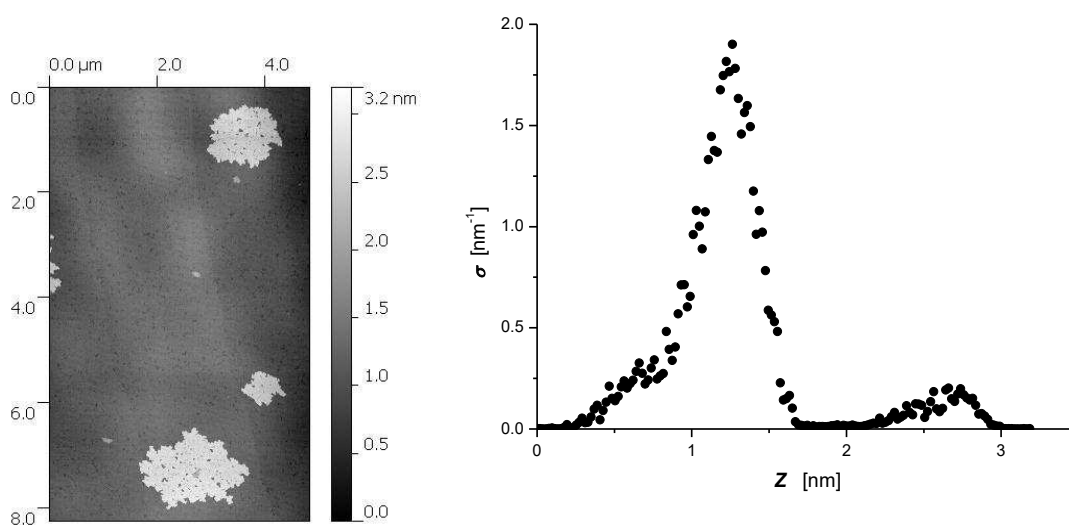


Figure S17. Profile analysis of aggregates of the LNH-NO₃(p) nanosheets prepared by spin coating on a mica support. The analysis shows an aggregate height of 1.3 nm.

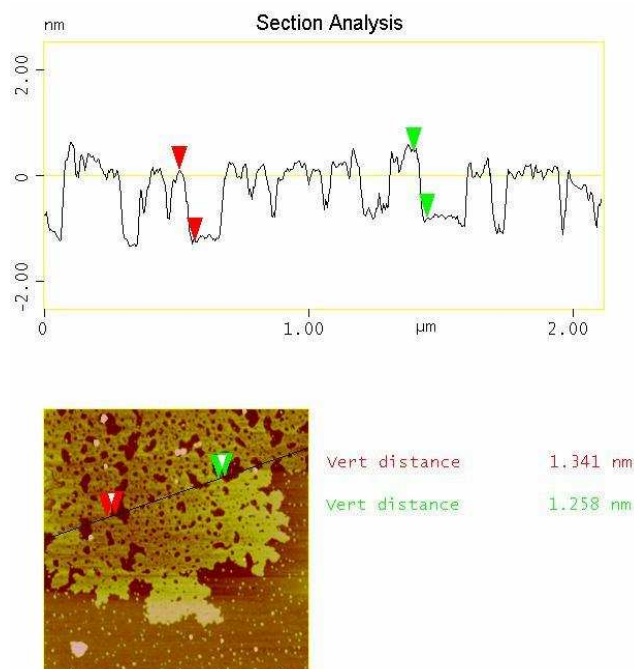


Figure S18. High-resolution TEM image at the centre of a LNH-Lactate(ae) nanosheet and the computed FFT pattern ($d_1 = 4.1 \pm 0.5 \text{ \AA}$, $d_2 = 2.3 \pm 0.5 \text{ \AA}$, $d_3 = 2.0 \pm 0.5 \text{ \AA}$).

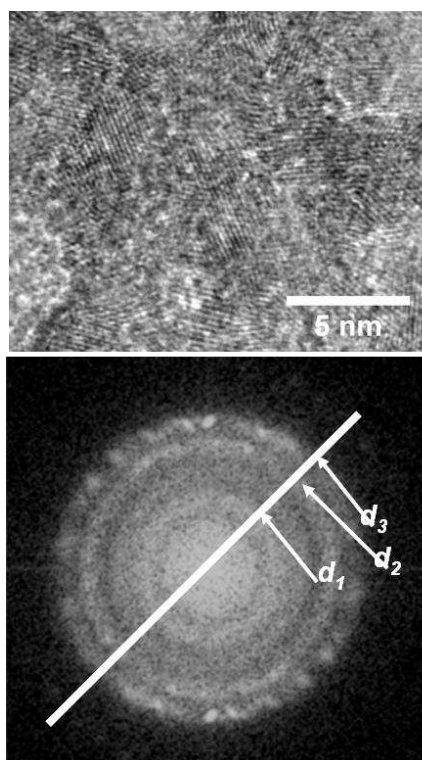
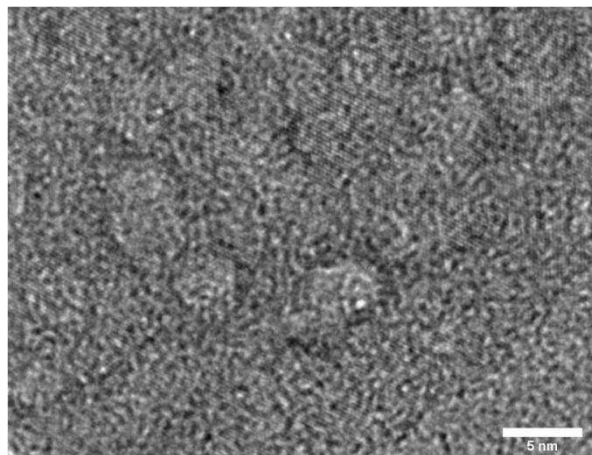


Figure S19. A) High-resolution TEM image of the LNH-NO₃(p) nanosheets showing the discontinuous atomic planes within a platelet. B) SAED pattern ($d_1 = 2.50 \pm 0.05 \text{ \AA}$, $d_2 = 1.50 \pm 0.05 \text{ \AA}$, $d_3 = 1.45 \pm 0.05 \text{ \AA}$, $d_4 = 1.27 \pm 0.05 \text{ \AA}$).

A)



B)



Apendix 3

Cite this: DOI: 10.1039/c4dt00141a

Electrochemical performance of cobalt hydroxide nanosheets formed by the delamination of layered cobalt hydroxide in water†

B. Schneiderová,^{a,b} J. Demel,^a J. Pleštil,^c H. Tarábková,^d J. Bohuslav^{d,e} and K. Lang^{*a}

We report the preparation of monometallic $\text{Co}^{2+}/\text{Co}^{3+}$ layered double hydroxide, intercalated with lactate anions (LCoH-Lactate), and its spontaneous delamination in water to form cobalt hydroxide nanosheets. These hydroxide nanosheets formed stable aqueous dispersions. The thickness of a nanosheet was estimated to be approximately 1 nm by atomic force microscopy and small angle X-ray scattering experiments, and corresponds to a single hydroxide layer. Some of the Co^{2+} cations were oxidised by oxygen, resulting in a mixed $\text{Co}^{2+}_{0.76}\text{Co}^{3+}_{0.24}$ layer composition. Upon water evaporation, the nanosheets restacked to form transparent self-standing films with a layered structure like that of the original material. The coverage of the surface with side-by-side stacks of nanosheets indicated two-dimensional agglomeration and suggested that these dispersions could be applied to prepare large monolayers of nanosheets. The layers prepared by spin-coating were stable and featured reversible and reproducible redox properties in an alkaline electrolyte. In an evaluation of their electrochemical performance, the cobalt hydroxide nanosheets exhibited durability and fast charge transfer kinetics during repetitive potential cycling up to 200 mV s^{-1} . The nanosheets prepared by the present method show promise for use in nanocomposite materials for energy storage applications.

Received 15th January 2014,
Accepted 19th February 2014

DOI: 10.1039/c4dt00141a

www.rsc.org/dalton

Introduction

The increasing consumption of energy in recent decades has continued to drive demands for effective electrochemical energy conversion and storage devices based on batteries, fuel cells, and electrochemical supercapacitors.^{1,2} Considerable effort has been devoted to developing inexpensive electrode materials with high specific capacitance. Interest has focused on nickel- and cobalt-based materials, which are inexpensive and have excellent redox reversibility and stability.^{3–6}

Layered transition metal hydroxides possess desirable electrochemical activity originating from their redox character. Their structure is derived from layered double hydroxides (LDHs) of the general formula $[\text{M}^{2+}_{(1-x)}\text{M}^{3+}_x(\text{OH})_2]^{x+}(\text{A}^{m-})_{x/m} \cdot n\text{H}_2\text{O}$, where M^{2+} and M^{3+} are divalent and trivalent metal cations, respectively, octahedrally coordinated by hydroxide groups and A^{m-} is the interlayer anion compensating for the positive charge of the brucite-like hydroxide layers.⁷ In contrast, layered simple hydroxides consist of hydroxide layers that contain a single type of metal cation and a positive charge that is created by hydroxyl vacancies.^{8,9} These compounds have promising electrochemical,^{1,2} magnetic,¹⁰ and photo-physical properties,¹¹ or are good metal oxide precursors.¹²

Many studies have been performed to synthesise layered cobalt hydroxides and control their composition, structure, morphology, size, and crystallinity.^{13–20} These compounds are known for their structural variability. There are two polymorphs; $\beta\text{-Co}(\text{OH})_2$ is of a brucite-like origin, where Co^{2+} ions are octahedrally coordinated by hydroxyl ions and form two-dimensional charge-neutral layers stacked tightly together *via* hydrogen bonding interactions. The second polymorph, $\alpha\text{-Co}(\text{OH})_2$, contains vacant octahedral sites, and each vacancy is capped by two tetrahedrally coordinated divalent cobalt cations on opposite sides of the layer. The charge compensating anions are located in the interlayer space, and thus, the

^aInstitute of Inorganic Chemistry of the AS CR, v. v. i., Husinec-Řež 1001, 250 68 Řež, Czech Republic. E-mail: lang@iic.cas.cz; Fax: +420 22094 1502;

Tel: +420 26617 2193

^bFaculty of Science, Charles University in Prague, Hlavova 2030, 128 43 Praha 2, Czech Republic

^cInstitute of Macromolecular Chemistry of the AS CR, v. v. i., Heyrovského nám. 2, 162 06 Praha 6, Czech Republic

^dJ. Heyrovský Institute of Physical Chemistry of the AS CR, v. v. i., Dolejškova 3, 182 23 Praha 8, Czech Republic

^eInstitute of Chemical Technology, Prague, Technická 5, 166 28 Praha 6, Czech Republic

†Electronic supplementary information (ESI) available: Elemental analysis, charge reversibility, TGA/DTA/MS curves, powder XRD patterns, FTIR and UV-Vis spectra, SAXS curves, AFM images, electrochemical properties. See DOI: 10.1039/c4dt00141a

basal spacing depends on the anion size. New synthetic techniques have enabled the bulk synthesis of α - and β -Co(OH)₂ platelets.¹⁶ The transformation of β -Co(OH)₂ into a mixed Co²⁺/Co³⁺ LDH phase can be achieved by using oxidizing agents to partially convert Co²⁺ to Co³⁺.^{21,22} This method produced a highly crystalline LDH phase composed of a single transition metal with mixed oxidation states.

Layered cobalt hydroxides have interesting properties owing to cobalt coordination variability, unpaired electrons, and the presence of various anions in the interlayer space. The electrochemical applications, mainly capacitors^{4,23,24} and rechargeable batteries,^{3,6} are based on the redox transformation of Co²⁺ to CoOOH or cobalt oxides and can be enhanced by nanostructuring cobalt hydroxide deposits^{23,25} or mixing Co and Ni ions in hydroxide nanosheets.⁶ The rate determining step of the redox reaction is the diffusion of compensating ions in a bulk electrode, and thus, the efficiency of the electron transfer reaction decreases with the scan rate.²⁶ This behaviour leads to the concept of electrodes of nanosized thickness with extremely fast electrochemical response. Monolamellar cobalt hydroxide nanosheets with high specific capacitance and cyclic stability⁶ are potential materials for such electrodes.

The preparation of hydroxide nanosheets is based on one of the most intriguing properties of layered hydroxides, *i.e.*, the splitting of layered hydroxides into two-dimensional hydroxide lamellae with thickness of approximately one nanometre and lateral size ranging from several tens of nanometres to micrometres.^{27,28} Adachi-Pagano *et al.* first reported that Zn/Al LDH intercalated with dodecyl sulphate could be refluxed in butanol at 120 °C to produce a colloidal solution with a translucent appearance indicative of delamination.²⁹ Bulky organic intercalants, such as dodecyl sulphate, make the interlayer galleries hydrophobic in nature and weaken the interactions between host layers.

The identification of new ecologically friendly and soft methods of nanosheet separation, especially delamination in water under gentle conditions, remains a challenge. In 2005, Hibino and Kobayashi reported for the first time that Mg/Al LDH intercalated with lactate anions can be delaminated in water.³⁰ Since then, only a small number of layered hydroxides containing acetate, lactate, propionate, 2-hydroxyethane-sulfonate, or 4-aminobenzoate anions have been successfully swelled and delaminated in water.^{31–34} Very recently, we used a simple, one-pot method to delaminate layered nickel hydroxides intercalated with lactate and nitrate anions and obtained stable aqueous dispersions of nanosheets.³⁵ These nanosheets were re-assembled into macroscopic films with well-defined nanosheet orientation, adjustable thickness, and interesting electrochemical behaviour.

In this paper, we describe a new method for delaminating monometallic Co²⁺/Co³⁺ layered double hydroxide in water. This approach involves the preparation of α -Co(OH)₂ with intercalated dodecyl sulphate anions, followed by anion exchange for lactate anions, and spontaneous delamination to form positively charged hydroxide nanosheets with mixed Co²⁺/Co³⁺ ions and LDH structure. The concentrations of these

aqueous colloids were as high as 30 mg mL⁻¹. These nanosheets can be assembled easily into ultrathin films with fast electrochemical responses as well as transparent self-standing films.

Experimental

Materials

Cobalt chloride, hexamethylenetetramine (HMT), and potassium hydroxide (all from Lachema, Czech Republic), sodium lactate and sodium dodecyl sulphate (both from Sigma-Aldrich), cetyltrimethylammonium bromide (CTAB) (Acros Organics), and acetone (Lachner, Czech Republic) were used as purchased. Chloroform and 1-butanol (Penta, Czech Republic) were dried over molecular sieves (Sigma-Aldrich). Deionised water (conductivity <0.15 μ S cm⁻¹) was used for these experiments.

Synthesis procedures

Synthesis of layered cobalt hydroxide with intercalated dodecyl sulphate anions (LCoH-DS) by precipitation. The amount of HMT (in equivalents of CoCl₂), the reaction time, and the solvent are given in Table S1 (see ESI).[†] In most cases, CoCl₂ × 6H₂O (0.004 mol), sodium dodecyl sulphate (0.02 mol), and HMT were dissolved in 100 mL of a water–alcohol mixture (9 : 1, v/v) and stirred at 90 °C. In one case, the starting materials were dissolved in 80 mL of water and placed in an autoclave at 100 °C for 24 h. The precipitates were centrifuged (High-speed Centrifuge Z36 HK, 5 min, 15 000 rpm) and washed with acetone and twice with deionised water. The resulting green/beige products were air-dried at room temperature. The results of elemental analyses are in Table S1 (see ESI).[†]

Synthesis of layered cobalt hydroxide with intercalated lactate anions (LCoH-Lactate) by anion exchange. LCoH-DS (0.15 g), sodium lactate (1.1 mL; 0.0077 mol), and CTAB (0.547 g; 0.0015 mol) were dispersed in a mixture of 25 mL of CHCl₃ and 12.5 mL of deionised water. The mixture was stirred for 1 hour at room temperature. The water phase containing LCoH-Lactate was collected in a separatory funnel and centrifuged (High-speed Centrifuge Z36 HK, 20 min, 20 000 rpm). The resulting brown product was washed with acetone to remove the traces of CHCl₃, and twice with deionised water. After centrifugation to remove the water phase, the product was air-dried at room temperature. The results of elemental analysis were (in %): Co 41.85, C 10.10, S 0.08, N 2.74, and H 2.28, corresponding to the formula Co(OH)₂(Lactate)_{0.24}(HMT)_{0.07}·0.7H₂O. The average oxidation state of cobalt ions was determined by the iodometric titration: a weighted sample of LCoH-Lactate was dissolved in a solution of KI in 6 M HCl in the dark and the solution was titrated with standard solution of 0.1 M Na₂S₂O₃ to obtain the amount of formed iodine.

Delamination. LCoH-Lactate undergoes delamination during the anion exchange reaction of LCoH-DS and subsequent washing with deionised water. LCoH-DS samples

behaved identically; therefore, all other experiments were performed with sample 4 (Table S1, ESI†). Most of the nanosheets were separated by centrifugation at 20 000 rpm for 20 min (High-speed Centrifuge Z36 HK). After washing for the second time, the sediment was dispersed in deionised water to form colloid solutions with concentrations up to approximately 30 mg mL⁻¹ of the delaminated nanosheets. Alternatively, dry LCoH-Lac powder was mixed with deionised water, and the particles delaminated completely with stirring.

Characterisation techniques

Powder X-ray diffraction (XRD) patterns in the reflection mode were recorded with a PANalytical X'Pert PRO diffractometer in the Bragg–Brentano geometry. The diffractometer was equipped with a conventional X-ray tube (CoK α , 40 kV, 30 mA) and a multichannel X'Celerator detector with an anti-scatter shield. The beam passed through a 1/8° divergence slit, a 1/4° anti-scatter slit, and a 0.02 rad Soller slit. The diffraction patterns were recorded in the range of 2–80° with a step size of 0.0167° and an acquisition time of 80.01 s per step, corresponding to a scan time of 50.38 min. Transmission-mode XRD experiments were performed with a PANalytical X'Pert diffractometer equipped with a Cu X-ray tube (40 kV, 30 mA), an elliptic focusing mirror, a 0.5° divergence slit, a 0.5° anti-scatter slit, and a 0.02 rad Soller slit in the primary beam. A fast PIXcel detector with an anti-scatter shield and a 0.02 rad Soller slit was used to detect the diffracted beam. The XRD patterns were collected in the range between 1 and 85° (2 θ) with a step of 0.013° and an acquisition time of 97.92 s per step. Qualitative analysis was performed with the HighScorePlus software package (PANalytical, Almelo, The Netherlands, version 3.0) and the JCPDS PDF-2 database.

Atomic force microscopy (AFM) images were collected using a Bruker Dimension Icon in Scanasyt mode using Scanasyt-air cantilevers (silicon tip on a silicon nitride lever). The samples were prepared by spin-coating diluted dispersions of nanosheets (4 mg mL⁻¹, diluted with water 1 : 10 000) on a mica surface. For electrochemical studies, layers were deposited by spin-coating on highly ordered pyrolytic graphite (HOPG) and examined with a Multimode Nanoscope IIIa microscope (Bruker, USA) in semicontact (tapping) mode in air. The same area was analysed before and after repetitive potential cycling. Nanoscope software, version 5.12r5, (Bruker, USA) was used for surface imaging and image analysis. Surface roughness is expressed in terms of roughness Ra and ISAD (image surface area difference) parameters.

Small angle X-ray scattering (SAXS) experiments were performed using a pinhole camera (Molecular Metrology SAXS System) attached to a microfocussed X-ray beam generator (Osmic MicroMax 002) operating at 45 kV and 0.66 mA (30 W). The camera was equipped with a multiwire gas-filled area detector with an active area diameter of 20 cm (Gabriel design). Two experimental arrangements were used to cover the q range of 0.05–10 nm⁻¹ ($q = (4\pi/\lambda) \sin \theta$, where λ is the wavelength and 2θ is the scattering angle). The dispersions contained 1 to 4 mg mL⁻¹ of the LCoH-Lactate nanosheets.

Fourier transform infrared spectra (FTIR) were collected with a Nicolet NEXUS 670-FT spectrometer using KBr pellets. The UV/vis absorption spectra were recorded using a Perkin-Elmer Lambda 35 spectrometer equipped with an integral sphere. The samples were diluted with BaSO₄. Thermal analyses (TGA/DTA/MS) were carried out using a Setaram SETSYS Evolution-16-MS instrument coupled with a mass spectroscopy system. The measurements were performed in synthetic air (flow rate 30 mL min⁻¹) from 30 to 1050 °C with a heating rate of 5 °C min⁻¹.

Charge transfer reactions were performed in a three-electrode cell equipped with a Pt counter electrode, a saturated calomel reference electrode (SCE), and nanosheets deposited on a basal plane HOPG as the working electrode. The electrolyte was an aqueous solution of 1 M KOH deoxygenated with argon. A three-electrode Wenking POS2 potentiostat (Bank Elektronik, Germany) was used to apply a potential to the working electrode.

Results and discussion

Characterisation of the prepared materials

LCoH-DS was prepared by mixing cobalt chloride with sodium dodecyl sulphate and hexamethylenetetramine (HMT) followed by performing a hydrothermal treatment.^{16,35} All the syntheses conditions and some sample characteristics are summarised in Table S1 (see ESI)†. The samples were probed by powder XRD (Fig. S1, ESI†), FTIR (Fig. S2 and discussion in ESI†), UV/vis absorption spectroscopy, and thermal analyses (Fig. S3, ESI†), and the results were consistent with those of α -Co(OH)₂ intercalated with DS reported earlier.^{16,19,36–38} In some cases, we observed partial oxidation of Co²⁺ to Co³⁺ ions by air during the synthesis.

XRD patterns confirm the formation of a crystalline layered cobalt hydroxide intercalated with the large anion, *i.e.*, they show a series of 00 l diffractions below 20° (2 θ , CoK α) indicating ordering along the layer stacking direction and broad non-basal diffractions at approximately 39, 71, and 84° (2 θ , CoK α) with tails that extended towards higher 2 θ values due to turbostratic disorder (Fig. S1, ESI†). The synthesis conditions affected the basal spacings, which were between 19.5 and 26.1 Å as calculated from the 00 l diffraction lines, and led to variability in the DS content obtained by elemental analyses. The molar ratios Co/DS were between 0.25 and 0.30 (Table S1, ESI†) and were similar to those reported in the literature.^{6,19} The anions interact with the hydroxide layers and the alkyl chains of adjacent layers interpenetrate each other. Thus, variations in the alignment of the alkyl chains of DS in the interlayer space combined with variations of the amount of intercalated water affect the basal spacing.

The UV/vis absorption spectra reflect the coordination environment of the cobalt atoms (Fig. 1). A broad absorption band at 420–580 nm due to d–d transitions of octahedrally coordinated Co²⁺ is consistent with the pink colour of Co(Lactate)₂ or β -Co(OH)₂. The green α -Co(OH)₂ samples contain

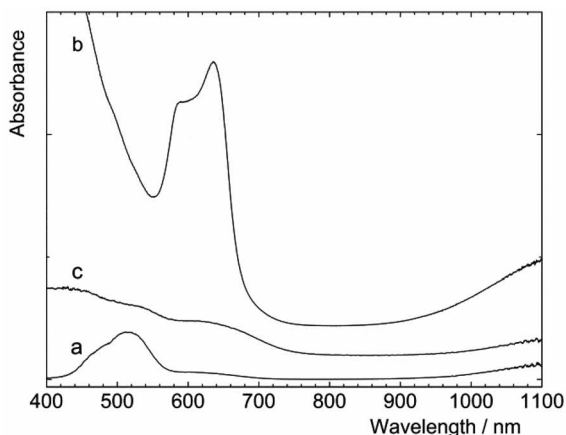


Fig. 1 UV/vis absorption spectra of Co(Lactate)_2 (a), LCoH-DS (sample 6 from Table S1, ESI[†]) (b), and LCoH-Lactate (c). These spectra are shifted vertically.

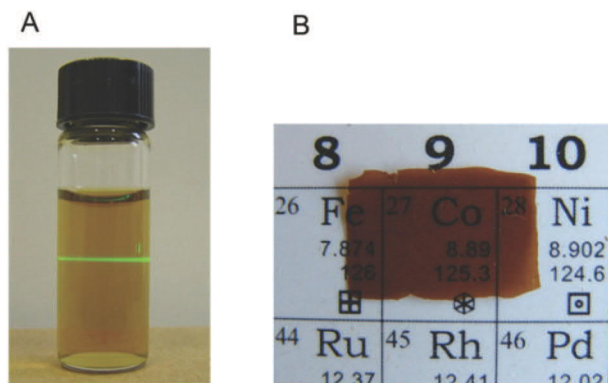


Fig. 2 Delamination of LCoH-Lactate: (A) dispersion of the cobalt hydroxide nanosheets documented by the Tyndall scattering of green laser light; and (B) self-standing film prepared from the nanosheets.

Co^{2+} in both octahedral and tetrahedral sites. Tetrahedrally coordinated cobalt cations exhibit two absorption peaks between 550 and 700 nm, and because these transitions are more intense than those of octahedrally coordinated Co^{2+} , the sample colour is green. In some cases, beige samples were observed, indicating partial oxidation of Co^{2+} to Co^{3+} ions by air during the synthesis.^{14,18}

The LCoH-DS samples underwent a procedure for lactate anion exchange in a biphasic water–chloroform system of CTAB, which removed DS from the interlayer spaces by forming ion pairs and dissolving them in the chloroform phase.³⁵ Surprisingly, this anion exchange was accompanied by the formation of brown colloidal dispersions (Fig. 1; Fig. S5, ESI[†]) as visualised by the Tyndall effect (Fig. 2A). These observations indicated that the product underwent immediate delamination into hydroxide nanosheets and partial oxidation of cobalt ions since brown colour is a sign of the presence of Co^{3+} .³⁹ It is well known that Co(OH)_2 can be oxidized by oxygen^{14,18} or other oxidation agents^{21,22,39} leading

to new LDH phases. Evidently, nanometre thickness of the nanosheets (see below) makes them very susceptible to air oxidation and no other oxidation agents are needed. The average oxidation state of cobalt ions obtained by iodometric titration was 2.23 and the elemental analysis showed consistent content of lactate anion per cobalt atom (*i.e.*, 0.24). These results allowed us to determine the chemical composition of LCoH-Lactate to be $\text{Co}^{2+}_{0.76}\text{Co}^{3+}_{0.24}(\text{OH})_2(\text{Lactate})_{0.24}(\text{HMT})_{0.07} \cdot 0.7\text{H}_2\text{O}$. Traces of DS and HMT that could not be removed by washing the products were noted.

The high efficiency of the anion exchange reaction was confirmed after the water evaporated; the basal spacing in LCoH-Lactate shrank to 11.8 Å, and the diffraction line intensities were unchanged, suggesting that anion exchange did not affect the original sample crystallinity. The basal spacing of 11.8 Å is slightly larger than that of lactate-intercalated $\alpha\text{-Ni(OH)}_2$ (10.5 Å)³⁵ and Mg/Al LDHs ($d_{003} = 9.9\text{--}11.1$ Å),⁴⁰ but it is smaller than the values reported for Zn/Al LDHs ($d_{003} = 13.5\text{--}14.5$ Å).³³ Possible explanations for this discrepancy between the gallery heights are different orientations of lactate anions in the interlayers and different levels of hydration of the interlayer spaces.

The thermal behaviour of LCoH-Lactate has features similar to those of LCoH-DS (Fig. S3 and S4, ESI[†]). The first broad endothermic peak between 30 and 145 °C with a weight loss of 8.8% corresponds to the release of surface and interlayer water molecules on the basis of mass spectroscopy of gas products. Exothermic peaks between 210 °C and 310 °C are accompanied by the release of water, carbon dioxide, and traces of nitrogen oxides (HMT decomposition) due to dehydroxylation of the hydroxide layers and the thermal decomposition of the interlayer lactate anions. The endothermic peak with a maximum at 920 °C corresponds to the thermal decomposition of the spinel oxide Co_3O_4 to form CoO .

The FTIR spectra of LCoH-Lactate (Fig. S2, ESI[†]) display vibrations of intercalated lactate anions, water molecules (the OH stretching vibrations at approximately 3440 cm^{-1} and the OH deformation vibration at 1633 cm^{-1}), and the skeletal vibrations of cobalt hydroxide layers (below 1000 cm^{-1}). These spectra are dominated by the asymmetric and symmetric stretching modes of the lactate carboxyl group at 1587 cm^{-1} and 1405 cm^{-1} , respectively, and the stretching C–OH vibrations at 1120 cm^{-1} . Some lactate peaks are superimposed with peaks corresponding to HMT and DS traces.

Delamination and preparation of the films

As shown above, colloidal dispersions of the $\text{Co}^{2+}_{0.76}\text{Co}^{3+}_{0.24}$ hydroxide nanosheets were formed during the synthesis of LCoH-Lactate. Neither sonication nor heating was needed. The dispersions were at concentrations up to 30 mg mL^{-1} and did not sediment over a month. Also, dry LCoH-Lactate powder delaminated quantitatively but required shaking. The brown dispersions of these nanosheets have broad UV/vis absorption bands at approximately 530 and 620 nm (Fig. S5, ESI[†]), which are similar to those observed for the LCoH-Lactate powder (Fig. 1).

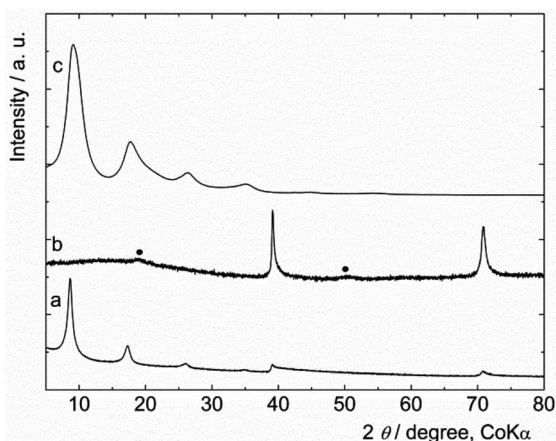


Fig. 3 XRD patterns of the LCoH-Lactate powder (a), and the LCoH-Lactate self-standing film in transmission (b) and reflection (c) modes. The diffractograms are shifted vertically to avoid overlap. The diffraction peaks of the Mylar foil support (●) are labelled.

After slow evaporation of water from the dispersions on a polypropylene tray at room temperature, the LCoH-Lactate nanosheets restack to form large self-standing films that can be peeled off the support (Fig. 2B). These brown films are transparent, suggesting a regular arrangement of the nanosheets that was also confirmed by XRD experiments (see below). The composition of the nanosheets remains unchanged after stacking because the UV/vis spectra are identical for the films and the dispersions (Fig. S5, ESI†). The films were manipulated carefully without breakage.

The XRD patterns of a film are shown in Fig. 3. In reflection mode, the non-basal diffractions disappear completely. In transmission mode, the diffractogram for the same sample has well-developed non-basal diffraction lines at 39.0 and 70.7° (2θ , $\text{CoK}\alpha$), and the basal diffractions are completely suppressed. The positions of the non-basal diffractions for the film, which are identical to those of the LCoH-Lactate powder, signify that the nanosheets retain the original hydroxide structure of LCoH-Lactate. The disappearance of the non-basal diffractions in reflection mode and the absence of the basal diffractions in transmission mode are clear evidence that the orientation of the nanosheets is parallel to the film surface. The basal spacing of 11.2 \AA in the restacked film is in good agreement with that of LCoH-Lactate (11.8 \AA).

Morphology of the nanosheets

The shapes of the dispersed nanosize particles were analysed by SAXS. The scattering curves follow power-law behaviour (eqn (1)), with exponent α equal to 2.0, which is typical for planar particles with large aspect ratios (Fig. S6, ESI†).

$$I(q) = Aq^{-\alpha} + B \quad (1)$$

The first term, $Aq^{-\alpha}$, is ascribed to scattering by homogeneous particles, and the second term, B , which is proportional to particle concentration, represents local fluctuations of the scattering density. The absence of

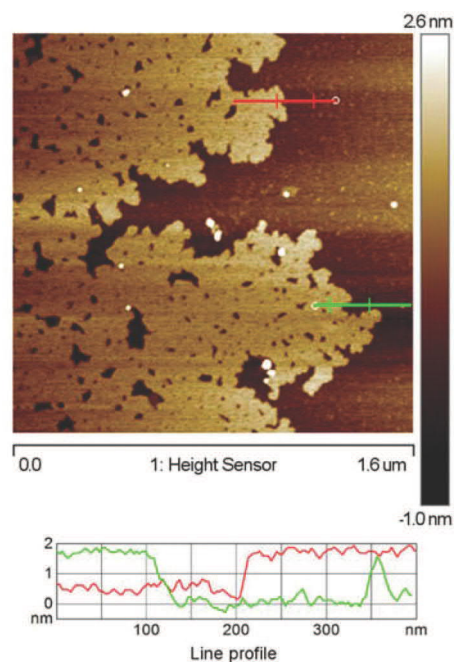


Fig. 4 Profile analysis of the LCoH-Lactate nanosheets imaged by AFM on a mica surface.

diffraction peaks in the scattering curves indicates that the dispersed nanoparticles do not stack together. The overlap of the corrected scattering curves, normalised to unit concentration, shows that there is no intraparticle interference (Fig. S6, ESI†) and facilitates the interpretation of the scattering data. The thickness and diameter of the particles were obtained by fitting the corrected SAXS curves with the scattering function derived for planar particles with a homogeneous cross-section (Fig. S7, ESI†). The result for lateral size is approximately 70 nm . The estimated thickness of the nanosheets is in the $0.7\text{--}0.9 \text{ nm}$ range. Because there was only a limited amount of information in the q -range relevant for determining the particle thickness ($q \sim 0.3\text{--}1.0 \text{ \AA}^{-1}$), a more precise analysis could not be performed.

The AFM image and line profile analysis of LCoH-Lactate deposits clearly show the separated nanosheets and large two-dimensional aggregates (Fig. 4). The section analysis reveals a uniform height, approximately 1 nm , which corresponds to a hydroxide monolayer.^{27,28} A roughness factor (R_a) of approximately 0.3 nm suggests that the surface of the deposited film is very smooth. Thus, spin-coating these nanosheet dispersions is a simple and quick method for fabricating ultrathin cobalt hydroxide films with large areas. Both AFM and SAXS results show that a large portion of the LCoH-Lactate sample is delaminated into single hydroxide layers.

Nanomorphology and electrochemical properties of the cobalt hydroxide nanosheets

An AFM was used to investigate the nanomorphology of the cobalt hydroxide films that were deposited from aqueous dispersions of the nanosheets. The spin-coated deposits,

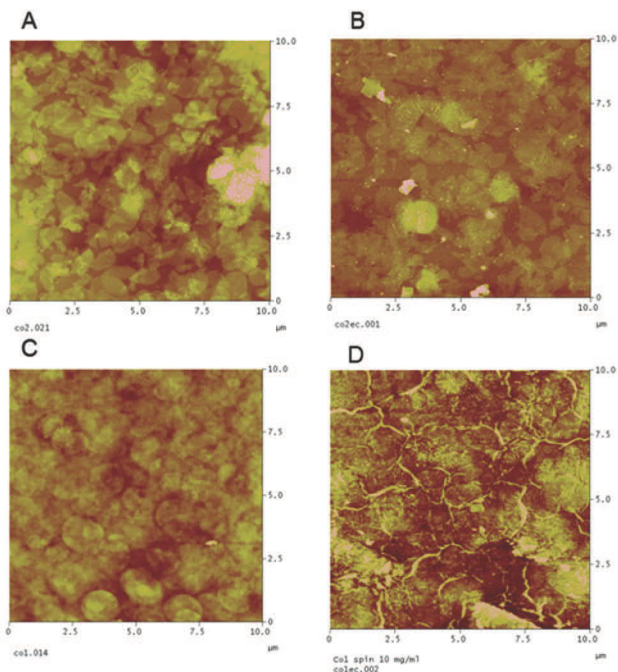


Fig. 5 AFM topography image (tapping mode) of the spin-coated deposits on the basal plane HOPG that were prepared from 2 mg mL^{-1} (A, B) and 10 mg mL^{-1} (C, D) aqueous dispersions of the LCoH-Lactate nanosheets. Deposits before (A, C) and after (B, D) repetitive potential cycling (from -800 mV to $+500 \text{ mV}$ vs. SCE) in aqueous 1 M KOH solution.

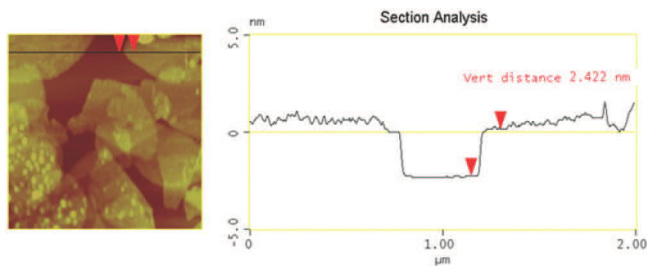


Fig. 6 Profile (line) analysis of the spin-coated cobalt hydroxide deposit (2 mg mL^{-1} dispersion) on the basal plane HOPG shows (i) a uniform nanosheet with a thickness of approximately 2.5 nm , (ii) partial overlapping of some nanosheets, and (iii) incomplete surface coverage.

prepared using 2 and 10 mg mL^{-1} dispersions (Fig. 5A and C), display relatively smooth surfaces with roughness parameters R_a of 1.6 and 5.4 nm (ISAD 0.22 and 0.56%), respectively, and exhibit a quasi-two-dimensional nanosheet structure with a uniform sheet thickness of approximately 2.5 nm (Fig. 6). Spin-coating does not ensure complete coverage of a highly ordered pyrolytic graphite (HOPG) support by the nanosheets, as documented by AFM images and profile analysis (Fig. 6). However, drop casting the 2 mg mL^{-1} dispersion yields uneven and rough surfaces with R_a of approximately 16 nm (ISAD 0.89%) and unresolved platelet nanostructures (Fig. S8, ESI†).

To investigate the kinetics of the charge transfer reaction and to ascertain the stability of the deposited nanosheets,

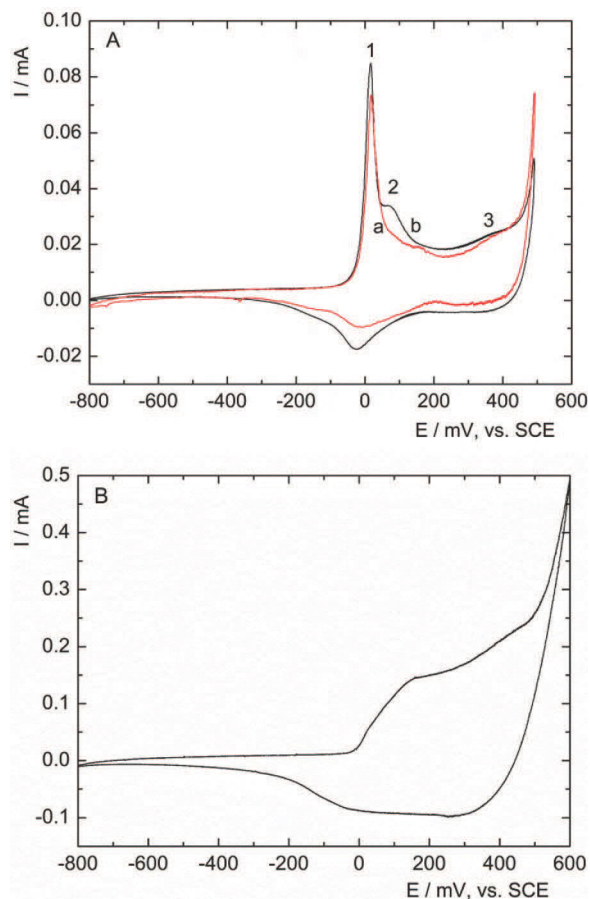
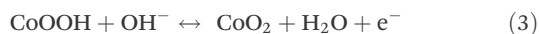


Fig. 7 Cyclic voltammetry of cobalt hydroxide deposits on the basal plane HOPG: (A) spin-coated deposits prepared using 2 mg mL^{-1} (a) and 10 mg mL^{-1} (b) dispersions (for better clarity, the current of deposit (a) was multiplied by 10); (B) drop-cast deposit prepared from the 2 mg mL^{-1} dispersion. Cyclic voltammetry was performed in aqueous 1 M KOH electrolyte solution deoxygenated with argon. The scan rate was 10 mV s^{-1} . The numbering of the peaks corresponds to the discussion in the text.

potential cycles were applied repeatedly to the deposits while immersed in aqueous 1 M KOH solution. The surface nanomorphology was also imaged by AFM after the repetitive electrochemical cycling and was assigned to the corresponding current–potential characteristics. The cyclic voltammograms scans exhibit three pairs of peaks (Fig. 7). The first anodic peak (at 0 mV vs. SCE) is attributed to oxidation of the Co(OH)_2 nanosheets to form cobalt oxyhydroxide, CoOOH , and the cathodic peak corresponds to the reverse reduction process (eqn (2)) at the interface between the cobalt hydroxide nanosheets and the electrolyte.

Both spin-coated deposits yield sharp and narrow first anodic peaks (Fig. 7A, peak 1) at the used sweep rates (10 – 200 mV s^{-1}). These voltammetric features are typical of fast surface oxidation. The dependence of the peak current vs. potential sweep rate is linear confirming that the peak is due to the surface-confined reaction (Fig. S9, ESI†). Cathodic peak potentials, $E_c = -30 \text{ mV}$ (10 mg mL^{-1}) and -10 mV (2 mg mL^{-1}),

do not change; however, the corresponding anodic peak potentials shift by approximately 100 mV in the positive direction (Fig. S10, ESI†). The second peak at approximately 70 mV vs. SCE, indicating the formation of distinct phases with different electrode kinetics, is almost absent for the deposits prepared using the 2 mg mL⁻¹ dispersion (Fig. 7A, peak 2). The appearance of the second peak may be related to a nanomorphological rearrangement and/or phase change in the deposit bulk that would be logically more pronounced in denser deposits prepared using the 10 mg mL⁻¹ dispersion. This behaviour was observed in thick nickel hydroxide films.^{35,41} The most positive anodic peak at approximately 400 mV vs. SCE is poorly developed (Fig. 7A, peak 3) and can be assigned to further oxidation of CoOOH according to eqn (3).⁴²



In contrast, the peaks of the thick drop-cast cobalt hydroxide films are less clearly resolved and almost merge together (Fig. 7B). These layers are evidently affected by the resistance drop and by the slow charge transfer kinetics caused by the limited mobility of charge compensating ions in the bulk.

The charge reversibility represents another important parameter characterising the stability of the deposits and the efficiency of charge transfer in the anodic and cathodic processes. In this study, the ratio (Q_a/Q_c) of the anodic (Q_a) and the cathodic (Q_c) charges oscillates between 0.8 and 1.2, and it is independent of the investigated sweep rate (10–200 mV s⁻¹) within experimental error (Table S2, ESI†). These results for the charge reversibility denote the good stability of the spin-coated deposits during multiple potential cycles, as is also documented in Fig. S11 (see ESI).† The observation that the charge reversibility Q_a/Q_c is independent of sweep rate also suggests that the charge-transfer reaction is fast and not controlled by diffusion processes due to the lamellar character of the electrode material.

A comparison of the voltammograms shows that only those cobalt hydroxide deposits prepared by spin-coating and not substantially exceeding monolamellar coverage can be used to prepare electrodes with fast charge transfer kinetics. The nanomorphology of the spin-coated deposits formed from the low concentration dispersion (2 mg mL⁻¹) does not change significantly after repetitive potential cycling (Fig. 5B). However, the multilamellar deposits prepared by spin-coating from the 10 mg mL⁻¹ dispersion (Fig. 5C) show lifting of the platelet boundaries (Fig. 5D). This edge lifting can be attributed to gas evolution in gaps between platelets where graphene surfaces are exposed, and thus, gas evolution occurs at lower over-voltages than at coated surfaces.

In conclusion, ultrathin deposits of the preferentially oriented hydroxide nanosheets were prepared by spin-coating LCoH-Lactate dispersions. During potential sweeps, these deposits may be more durable than thicker deposits. Additionally, the reaction occurs within the hydroxide nanosheets, and

thus, the electron transfer efficiency is unaffected by the scan rate, allowing for the construction of ultrathin electrodes with fast electrochemical responses.

Conclusions

In summary, we have successfully delaminated layered cobalt hydroxide in water and produced nanosheet dispersions at concentrations up to 30 mg mL⁻¹. Delamination occurs during the anion exchange of lactate anions with dodecyl sulphate anions intercalated in $\alpha\text{-Co(OH)}_2$, and delamination is associated with the partial oxidation of Co²⁺ in the hydroxide nanosheets. Hydroxide nanosheets with mixed Co²⁺_{0.76}Co³⁺_{0.24} composition have a thickness of approximately 1 nm, corresponding to a single hydroxide layer, and can be re-assembled easily into transparent, oriented thin/ultrathin films with LDH structure. The ease of Co²⁺ oxidation initiated the exploration of electrochemical properties of these nanosheets. This study shows that delaminating and re-stacking these nanosheets is a fast, easy approach for the preparation of films with tuneable thickness and controlled charge-discharge properties in alkaline electrolytes. These nanosheets are electrochemically stable, reversible, and exhibit fast electrochemical responses at sweep rates up to 200 mV s⁻¹. As result of their properties, these cobalt hydroxide nanosheets are very interesting materials for the construction of electrochemical devices with long cycle lives and fast charging properties.

Acknowledgements

This work was supported by the Czech Science Foundation (no. 13-09462P). We thank Petr Bezdička for XRD measurements and helpful discussions, Eva Večerníková and Jitka Večerníková for thermal analyses, Luboš Jankovič for elemental analyses, and Pavel Janda for helpful discussions on electrochemical properties.

Notes and references

- 1 G. Wang, L. Zhang and J. Zhang, *Chem. Soc. Rev.*, 2012, **41**, 797–828.
- 2 W. Deng, X. Ji, Q. Chen and C. E. Banks, *RSC Adv.*, 2011, **1**, 1171–1178.
- 3 J. Han, K. C. Roh, M. R. Jo and Y.-M. Kang, *Chem. Commun.*, 2013, **49**, 7067–7069.
- 4 E. Hosono, S. Fujihara, I. Honma, M. Ichihara and H. Zhou, *J. Power Sources*, 2006, **158**, 779–783.
- 5 R. R. Salunkhe, K. Jang, S. Lee and H. Ahn, *RSC Adv.*, 2012, **2**, 3190–3193.
- 6 X. Liu, R. Ma, Y. Bando and T. Sasaki, *Adv. Mater.*, 2012, **24**, 2148–2153.
- 7 D. G. Evans and R. C. T. Slade, in *Layered Double Hydroxides*, ed. X. Duan and D. G. Evans, Springer-Verlag, Berlin, 2006, vol. 119, pp. 1–87.

- 8 S. P. Newman and W. Jones, *J. Solid State Chem.*, 1999, **148**, 26–40.
- 9 G. G. C. Arizaga, K. G. Satyanarayana and F. Wypych, *Solid State Ionics*, 2007, **178**, 1143–1162.
- 10 G. Rogez, C. Massobrio, P. Rabu and M. Drillon, *Chem. Soc. Rev.*, 2011, **40**, 1031–1058.
- 11 J. Demel and K. Lang, *Eur. J. Inorg. Chem.*, 2012, 5154–5164.
- 12 J. Demel, J. Pleštil, P. Bezdička, P. Janda, M. Klementová and K. Lang, *J. Phys. Chem. C*, 2011, **115**, 24702–24706.
- 13 R. S. Jayashree and P. V. Kamath, *J. Mater. Chem.*, 1999, **9**, 961–963.
- 14 Z. P. Xu and H. C. Zeng, *J. Mater. Chem.*, 1998, **8**, 2499–2506.
- 15 R. Ma, Z. Liu, K. Takada, K. Fukuda, Y. Ebina, Y. Bando and T. Sasaki, *Inorg. Chem.*, 2006, **45**, 3964–3969.
- 16 Z. Liu, R. Ma, M. Osada, K. Takada and T. Sasaki, *J. Am. Chem. Soc.*, 2005, **127**, 13869–13874.
- 17 L. Poul, N. Jouini and F. Fiévet, *Chem. Mater.*, 2000, **12**, 3123–3132.
- 18 F. Leroux, E. M. Moujahid, C. Taviot-Guého and J.-P. Besse, *Solid State Sci.*, 2001, **3**, 81–92.
- 19 Y. Du and D. O'Hare, *Inorg. Chem.*, 2008, **47**, 11839–11846.
- 20 J. R. Neilson, B. Schwenzer, R. Seshadri and D. E. Morse, *Inorg. Chem.*, 2009, **48**, 11017–11023.
- 21 R. Ma, K. Takada, K. Fukuda, N. Iyi, Y. Bando and T. Sasaki, *Angew. Chem., Int. Ed.*, 2008, **47**, 86–89.
- 22 R. Ma, J. Liang, X. Liu and T. Sasaki, *J. Am. Chem. Soc.*, 2012, **134**, 19915–19921.
- 23 V. Gupta, T. Kusahara, H. Toyama, S. Gupta and N. Miura, *Electrochem. Commun.*, 2007, **9**, 2315–2319.
- 24 T. Zhao, H. Jiang and J. Ma, *J. Power Sources*, 2011, **196**, 860–864.
- 25 C. Mondal, M. Ganguly, P. K. Manna, S. M. Yusuf and T. Pal, *Langmuir*, 2013, **29**, 9179–9187.
- 26 J. M. Ko, D. Soundarajan, J. H. Park, S. D. Yang, S. W. Kim, K. M. Kim and K.-H. Yu, *Curr. Appl. Phys.*, 2012, **12**, 341–345.
- 27 Q. Wang and D. O'Hare, *Chem. Rev.*, 2012, **112**, 4124–4155.
- 28 R. Ma and T. Sasaki, *Adv. Mater.*, 2010, **22**, 5082–5104.
- 29 M. Adachi-Pagano, C. Forano and J.-P. Besse, *Chem. Commun.*, 2000, 91–92.
- 30 T. Hibino and M. Kobayashi, *J. Mater. Chem.*, 2005, **15**, 653–656.
- 31 N. Iyi, Y. Ebina and T. Sasaki, *Langmuir*, 2008, **24**, 5591–5598.
- 32 N. Iyi, Y. Ebina and T. Sasaki, *J. Mater. Chem.*, 2011, **21**, 8085–8095.
- 33 C. Jaubertie, M. J. Holgado, M. S. San Román and V. Rives, *Chem. Mater.*, 2006, **18**, 3114–3121.
- 34 C. Nethravathi, J. Machado, U. K. Gautam, G. S. Avadhani and M. Rajamathi, *Nanoscale*, 2012, **4**, 496–501.
- 35 B. Schneiderová, J. Demel, J. Pleštil, P. Janda, J. Bohuslav, D. Ihiwakrim, O. Ersen, G. Rogez and K. Lang, *J. Mater. Chem. A*, 2013, **1**, 11429–11437.
- 36 J. T. Rajamathi, A. Arulraj, N. Ravishankar, J. Arulraj and M. Rajamathi, *Langmuir*, 2008, **24**, 11164–11168.
- 37 M. Kurmoo, P. Day, A. Derory, C. Estournes, R. Poinot, M. J. Stead and C. J. Kepert, *J. Solid State Chem.*, 1999, **145**, 452–459.
- 38 C. Nethravathi, S. Sen, N. Ravishankar, M. Rajamathi, C. Pietzonka and B. Harbrecht, *J. Phys. Chem. B*, 2005, **109**, 11468–11472.
- 39 M. A. Woo, M.-S. Song, T. W. Kim, I. Y. Kim, J.-Y. Ju, Y. S. Lee, S. J. Kim, J.-H. Choy and S.-J. Hwang, *J. Mater. Chem.*, 2011, **21**, 4286–4292.
- 40 M. S. San Román, M. J. Holgado, C. Jaubertie and V. Rives, *Solid State Sci.*, 2008, **10**, 1333–1341.
- 41 Z. Bastl, J. Franc, P. Janda, H. Pelouchová and Z. Samec, *Nanotechnology*, 2006, **17**, 1492–1500.
- 42 C.-Y. Sun, Y.-G. Zhu, T.-J. Zhu, J. Xie, G.-S. Cao and X.-B. Zhao, *J. Solid State Electrochem.*, 2013, **17**, 1159–1165.

ELECTRONIC SUPPLEMENTARY INFORMATION

Electrochemical performance of cobalt hydroxide nanosheets formed by the delamination of layered cobalt hydroxide in water

Barbora Schneiderová,^{a,b} Jan Demel,^a Josef Pleštil,^c Hana Tarábková,^d Jan Bohuslav,^{d,e} and Kamil Lang^{*a}

^a *Institute of Inorganic Chemistry of the AS CR, v. v. i., Husinec-Řež 1001, 250 68 Řež, Czech Republic*

^b *Faculty of Science, Charles University in Prague, Hlavova 2030, 128 43 Praha 2, Czech Republic*

^c *Institute of Macromolecular Chemistry of the AS CR, v. v. i., Heyrovského nám. 2, 162 06 Praha 6, Czech Republic*

^d *J. Heyrovský Institute of Physical Chemistry of the AS CR, v. v. i., Dolejškova 3, 182 23 Praha 8, Czech Republic*

^e *Institute of Chemical Technology, Prague, Technická 5, 166 28 Praha 6, Czech Republic*

*Corresponding author: Email address: lang@iic.cas.cz, Tel: +420 26617 2193, Fax: +420 22094 1502.

Contents

- Table S1. Conditions of syntheses and characterizing data of LCoH-DS.
- Table S2. Charge reversibility of the LCoH-Lactate electrodes.
- Figure S1. Powder XRD patterns of LCoH-DS.
- Figure S2. FTIR spectra of LCoH-DS and LCoH-Lactate.
- Figure S3,S4. Thermal analyses of LCoH-DS and LCoH-Lactate.
- Figure S5. UV/vis absorption spectrum of the LCoH-Lactate colloid and self-standing film.
- Figure S6,S7. SAXS curves of the aqueous dispersions.
- Figure S8. AFM amplitude image (tapping mode) of the drop-casted deposit on the basal plane HOPG.
- Figure S9. Dependence of the peak current *vs.* potential scan rate (ν) for the spin-coated cobalt hydroxide deposits on the basal plane HOPG.
- Figure S10. Dependence of the peak potential *vs.* potential scan rate (ν) for the spin-coated cobalt hydroxide deposits on the basal plane HOPG.
- Figure S11. Cyclic voltammetry of the spin-coated cobalt hydroxide deposits on the basal plane HOPG.

Table S1. Conditions of syntheses and characterizing data of LCoH-DS.

Sample	HMT/eq	T/°C	Time/h	Solvent	d / Å	Colour	Molar ratio Co/DS ^b
1	20	90	2	H ₂ O,MeOH	24.1	green	0.30
2	20	90	2	H ₂ O,BuOH	19.5	beige	0.25
3	20	90	1	H ₂ O,BuOH	22.6	beige	0.27
4	10	90	2	H ₂ O,BuOH	19.9	beige	0.25
5	3	90	2	H ₂ O,BuOH	23.1	green	0.27
6 ^a	3	100	24	H ₂ O	26.1	green	0.28

^a Reaction was performed in an autoclave.

^b Composition of synthesized LCoH-DS was estimated using elemental analyses data; molar ratio of Co/HMT was 1/0.04.

Table S2. Charge reversibility expressed as the ratio of anodic (Q_a) and cathodic (Q_c) charges (Q_a/Q_c) was elucidated from cyclic voltammograms of the spin-coated cobalt hydroxide electrodes vs. potential scan rate (v).

$v/\text{mV s}^{-1}$	Q_a/Q_c^a	Q_a/Q_c^b
10	1.01	1.01
20	0.75	1.23
50	0.78	0.88
100	0.77	0.87
200	0.93	0.84

^a Deposit prepared by spin-coating using the 10 mg ml⁻¹ dispersion.

^b Deposit prepared by spin-coating using the 2 mg ml⁻¹ dispersion.

Figure S1. Examples of powder XRD patterns recorded for LCoH-DS **6** (a) and LCoH-DS **4** (b). The sample LCoH-DS **6** has a minor contribution of a more extended phase with a basal spacing of 33.6 Å (●).

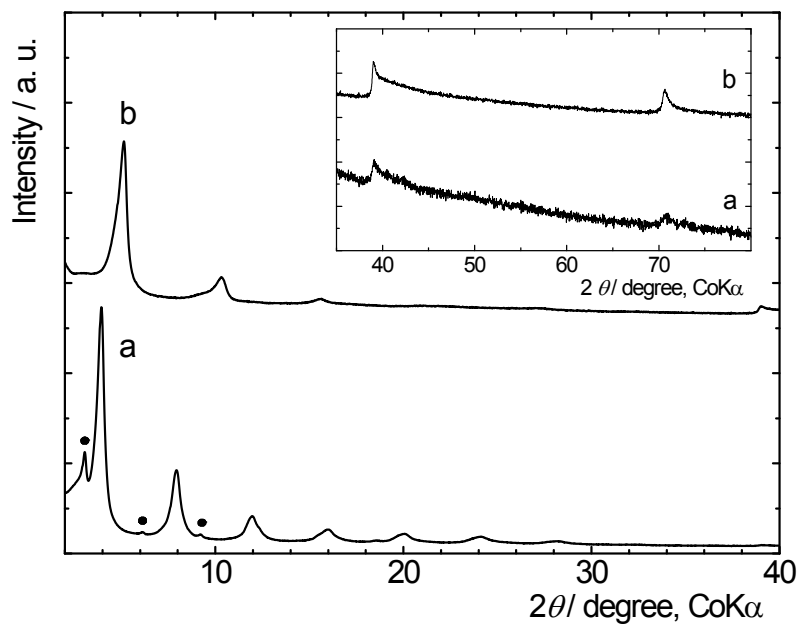
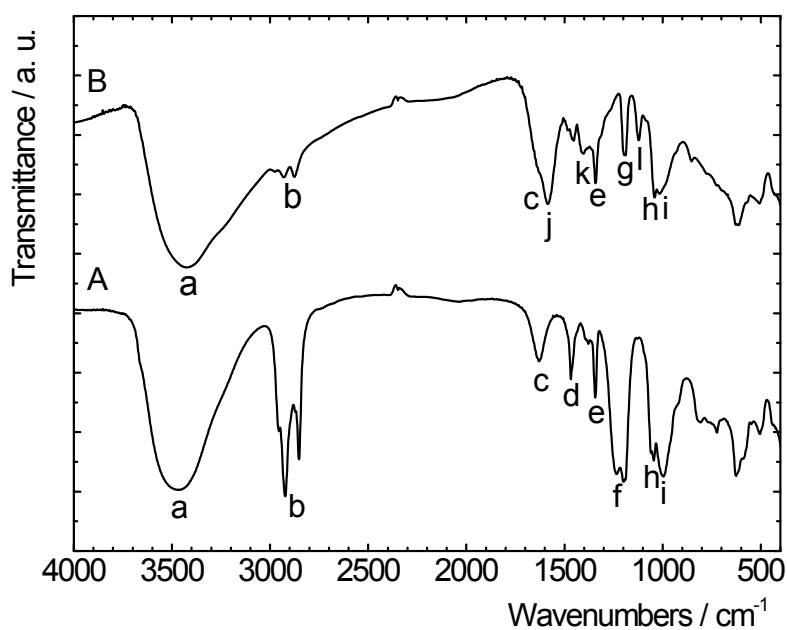


Figure S2. FTIR spectra of LCoH-DS **4** (A) and LCoH-Lactate (B). The spectra are vertically shifted and labelling refers to the discussion below.



FTIR spectra of LCoH-DS and LCoH-Lactate display vibrations of the intercalated anions, water molecules (the OH stretching vibrations at approximately 3440 cm^{-1} (a) and the OH deformation vibration at 1633 cm^{-1} (c)), and the skeletal vibrations of cobalt hydroxide (below 1000 cm^{-1}). Intercalated DS anions display the stretching vibrations of the C-H bonds in the range $3000 - 2780\text{ cm}^{-1}$ (b), the bending vibration of the organic chain at 1468 cm^{-1} (d), and the sulphate vibrations at 1234 and 1200 (f), 1045 (h), and 997 cm^{-1} (i). The traces of remaining HMT are indicated by the vibration at 1341 cm^{-1} (e), the other bands overlap with the signals of the sulphate groups.

Anion exchange of DS with the lactate anion is accompanied by the appearance of the stretching C-OH vibrations at 1120 cm^{-1} (l) and the asymmetric and symmetric stretching modes of the lactate carboxyl group at 1587 cm^{-1} (j) and 1405 cm^{-1} (k), respectively. The peaks at 2929 cm^{-1} and 2875 cm^{-1} (b), 1189 cm^{-1} (g), and the peaks (h, i) indicate the minor presence of HMT and DS, as was also confirmed by elemental analyses.

Figure S3. TGA/DTA/MS curves and the evolution of gases for LCoH-DS 4.

The measurement was performed in a synthetic air atmosphere (flow rate 30 mL min⁻¹) from 30 to 1100 °C with a heating rate of 5 °C min⁻¹.

The thermal behaviour of all the prepared samples is similar.

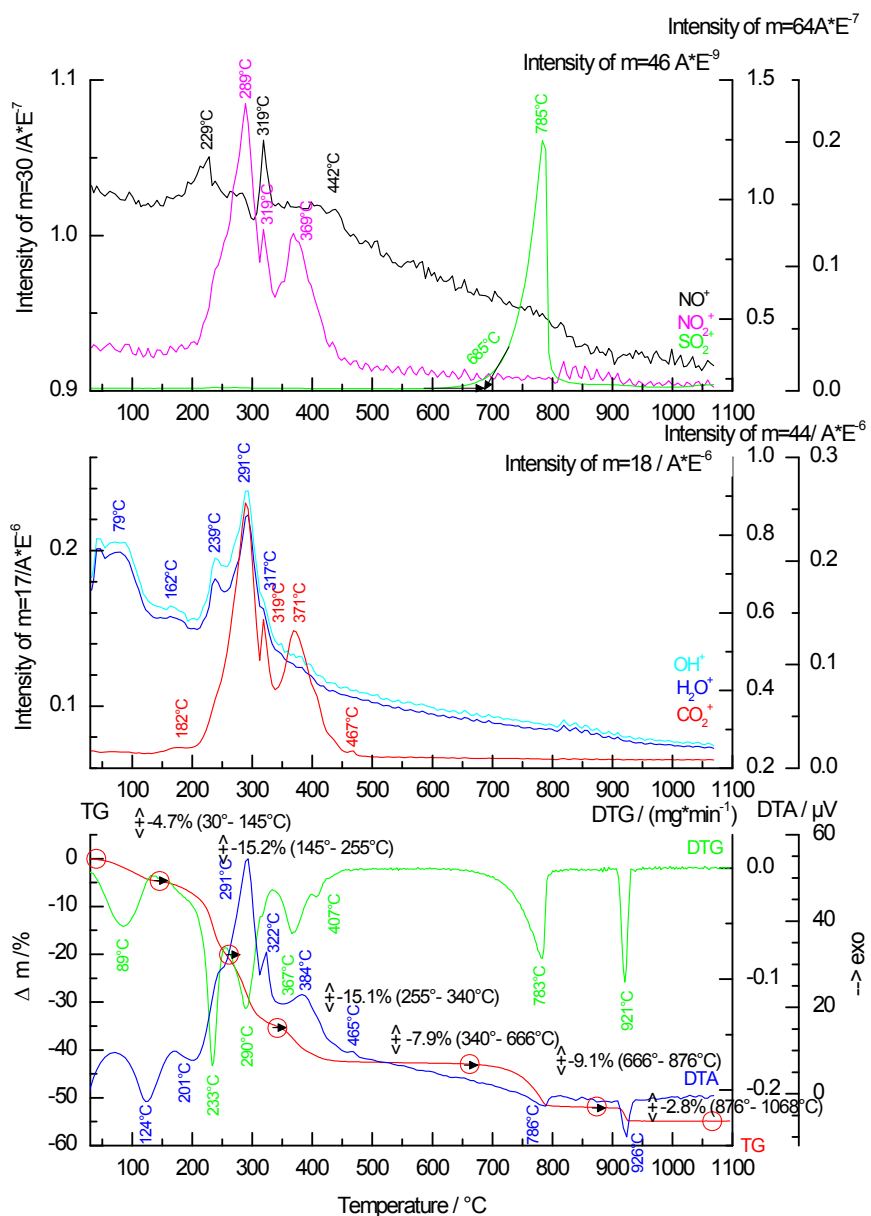


Figure S4. TGA/DTA curves for LCoH-Lactate.

The measurement was performed in a synthetic air atmosphere (flow rate 30 mL min⁻¹) from 30 to 1100 °C with a heating rate of 5 °C min⁻¹.

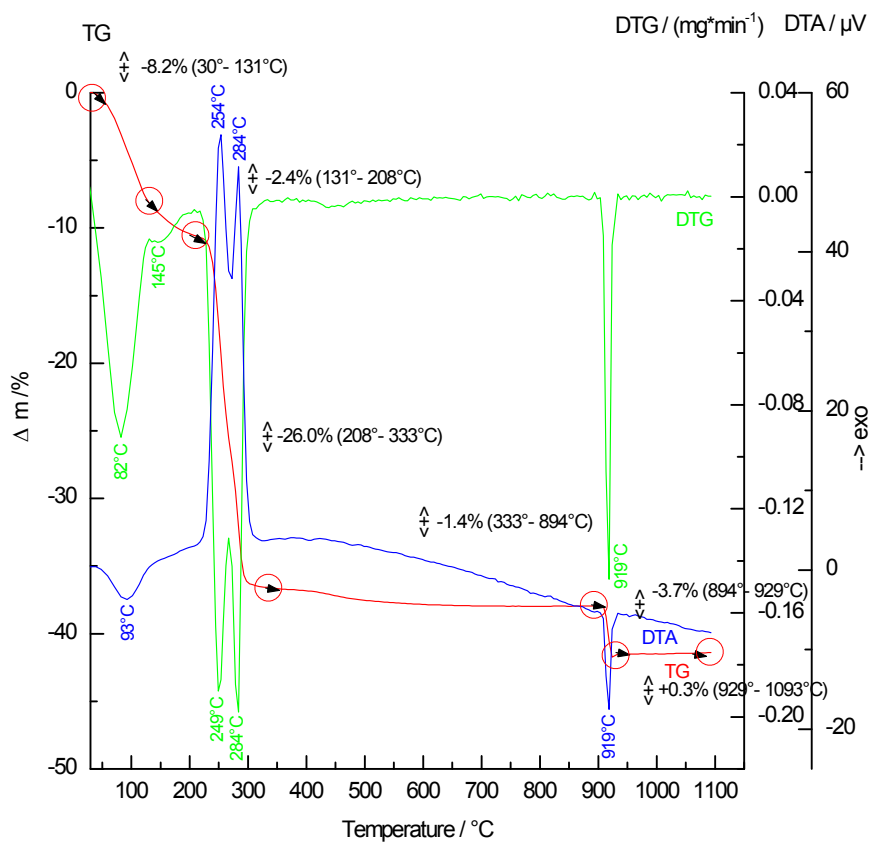


Figure S5. UV/vis absorption spectra of the LCoH-Lactate dispersion (a) and self-standing film (b). Spectra are vertically shifted.

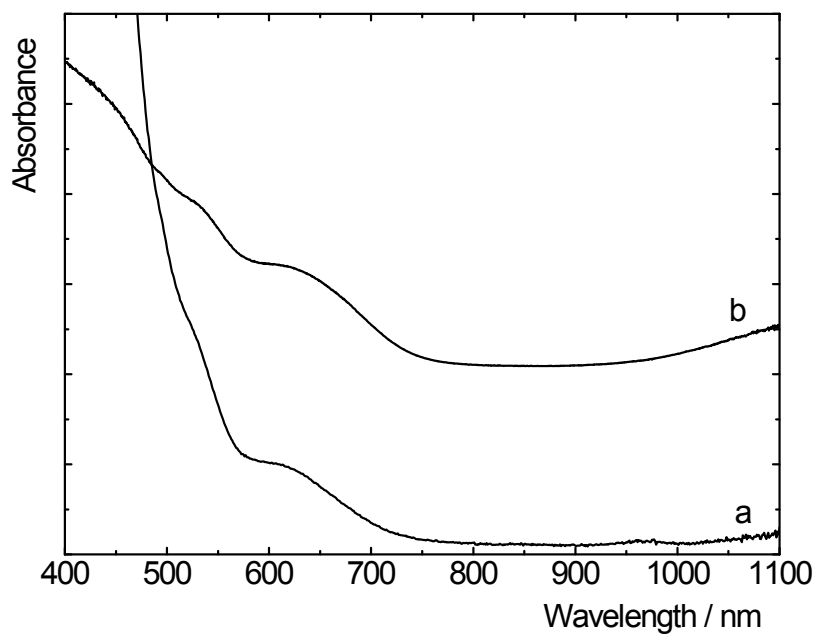


Figure S6. SAXS curves of the aqueous nanosheet dispersions were corrected for scattering from an empty capillary and solvent, intraparticle interference, and were normalized to unit concentration ($1 - 4 \text{ mg mL}^{-1}$).

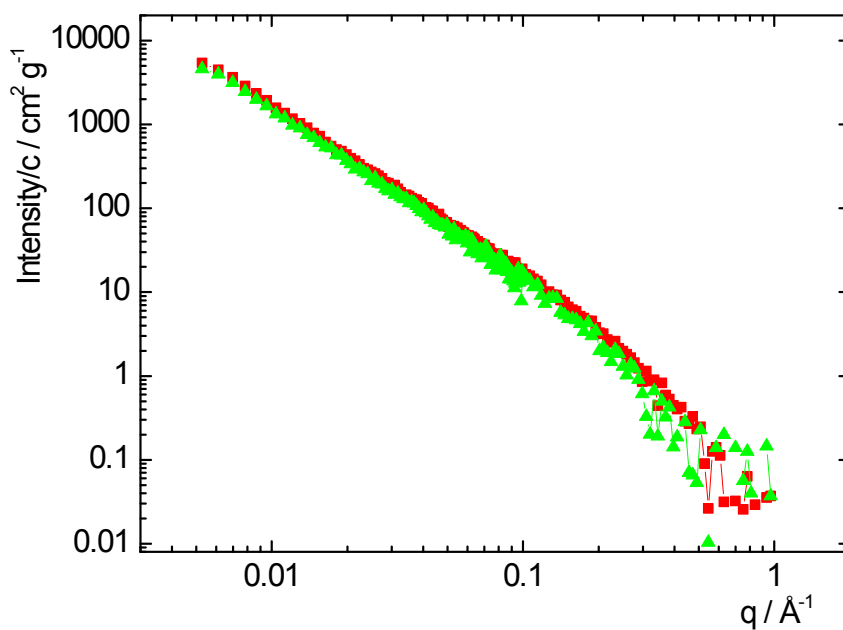


Figure S7. SAXS curve of the aqueous LCoH-Lactate dispersion (4 mg mL^{-1}). The red curve is a fitting scattering function of a model planar particle.

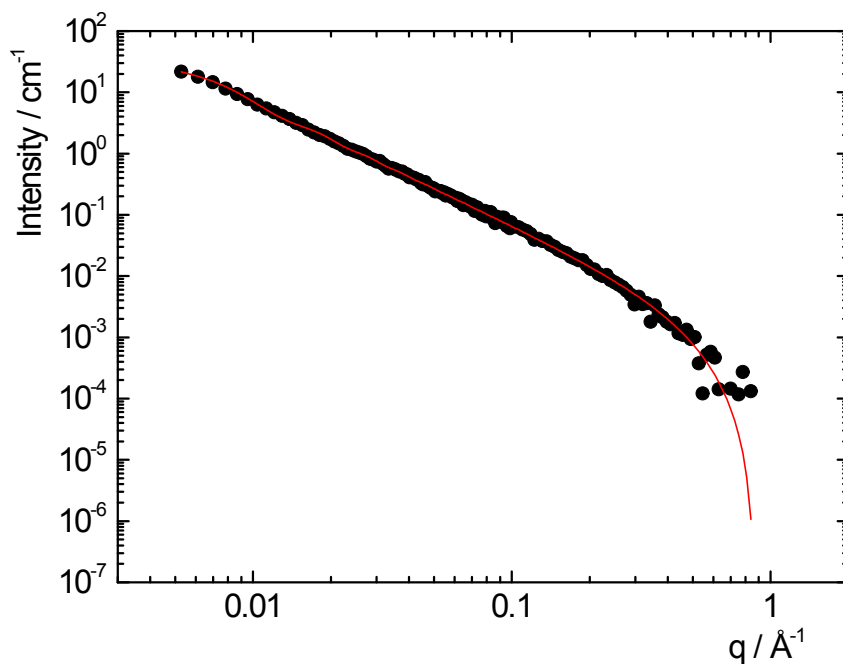


Figure S8. (A) AFM amplitude image (tapping mode) of the drop-casted deposit on the basal plane HOPG that was prepared from the aqueous dispersion of the LCoH-Lactate nanosheets (2 mg mL^{-1}); (B) the same after repetitive potential cycling (from -800 mV to $+500 \text{ mV}$ vs. SCE) in aqueous 1 M KOH solution.

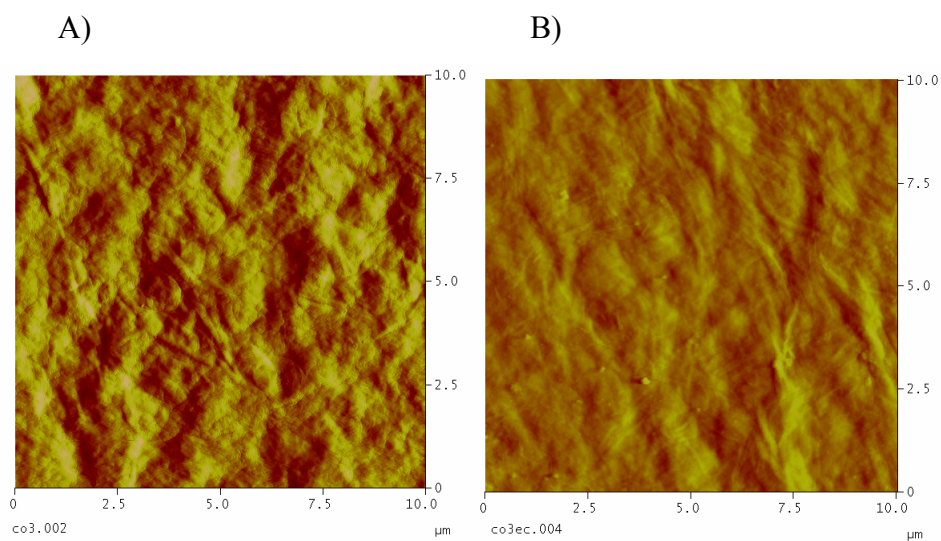


Figure S9. Dependence of the peak current (I_a is the anodic peak current; I_c is the cathodic peak current) vs. potential scan rate (v) for the spin-coated cobalt hydroxide deposits on HOPG. Measurements (A) and (B) represent the deposits prepared using 10 and 2 mg mL⁻¹ nanosheet dispersions, respectively.

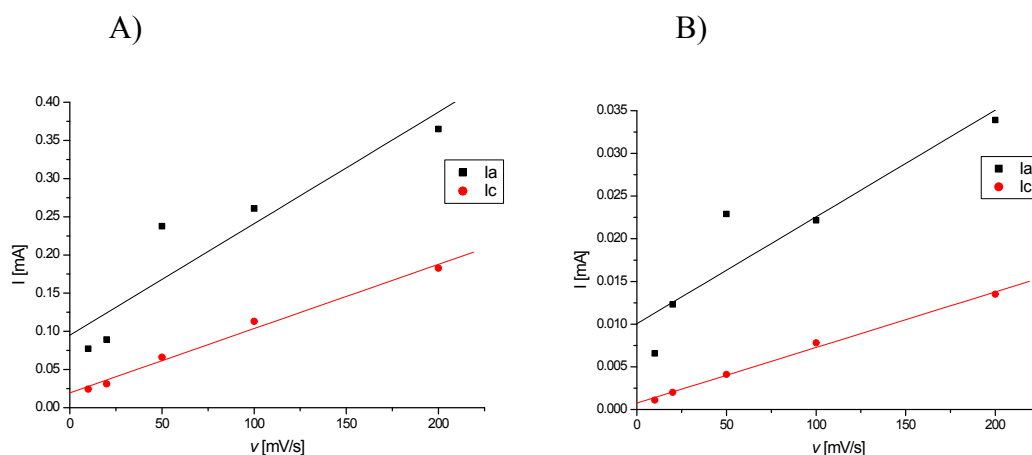


Figure S10. Dependence of the peak potential (E_a is the anodic peak potential; E_c is the cathodic peak current) vs. potential scan rate (v) for the spin-coated cobalt hydroxide deposits on the basal plane HOPG. Measurements (A) and (B) represent the deposits prepared using 10 and 2 mg mL⁻¹ nanosheet dispersions, respectively. Potentials are related to the saturated calomel reference electrode (SCE).

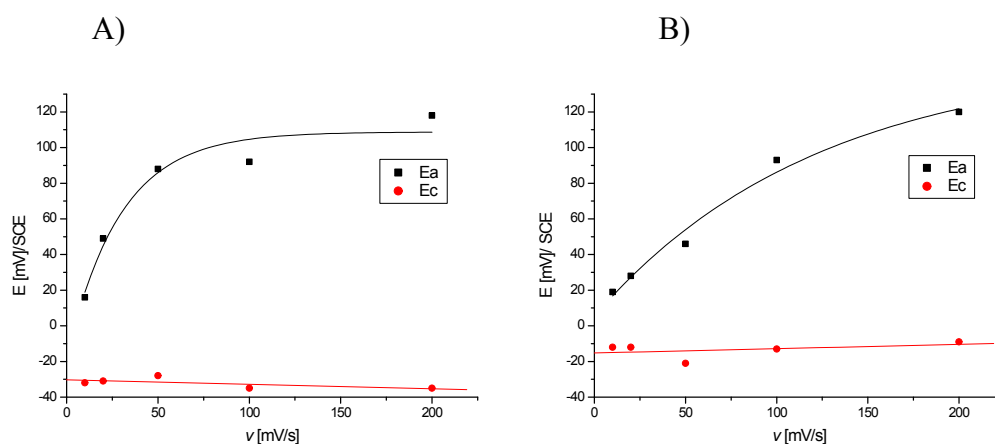
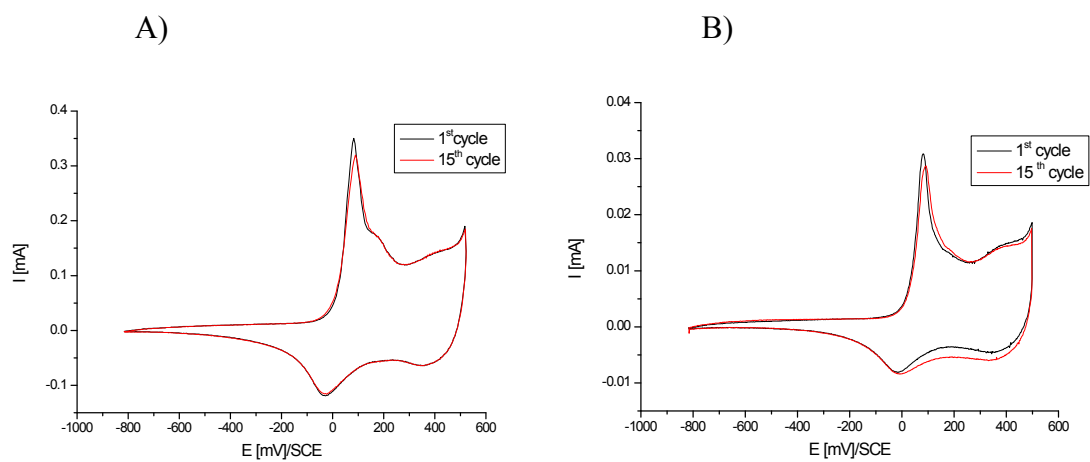


Figure S11. Cyclic voltammetry of the spin-coated nanosheet deposits on the basal plane HOPG. Voltammetry was performed in aqueous 1 M KOH electrolyte deoxygenated with Ar. Scan rate was 100 mV s⁻¹. Measurements (A) and (B) represent the deposits prepared using 10 and 2 mg mL⁻¹ dispersions, respectively. The potentials are related to SCE.



Apendix 4



Regular Article

Nickel-cobalt hydroxide nanosheets: Synthesis, morphology and electrochemical properties



Barbora Schneiderová^{a,b}, Jan Demel^a, Alexander Zhigunov^c, Jan Bohuslav^{d,e}, Hana Tarábková^d, Pavel Janda^d, Kamil Lang^{a,*}

^aInstitute of Inorganic Chemistry of the Czech Academy of Sciences, v.v.i., Husinec-Řež 1001, 250 68 Řež, Czech Republic

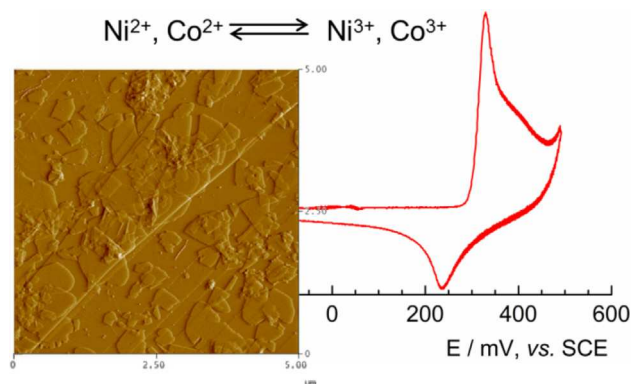
^bDepartment of Inorganic Chemistry, Faculty of Science, Charles University, Hlavova 2030, 128 43 Praha 2, Czech Republic

^cInstitute of Macromolecular Chemistry of the Czech Academy of Sciences, v.v.i., Heyrovského nám. 2, 162 06 Praha 6, Czech Republic

^dJ. Heyrovský Institute of Physical Chemistry of the Czech Academy of Sciences, v.v.i., Dolejškova 3, 182 23 Praha 8, Czech Republic

^eUniversity of Chemistry and Technology, Prague, Technická 5, 166 28 Praha 6, Czech Republic

GRAPHICAL ABSTRACT



ARTICLE INFO

Article history:

Received 2 January 2017

Revised 16 March 2017

Accepted 22 March 2017

Available online 25 March 2017

Keywords:

Hydroxide nanosheets

Delamination

Exfoliation

Layered nickel hydroxide

Layered cobalt hydroxide

Electrode material

ABSTRACT

This paper reports the synthesis, characterization, and electrochemical performance of nickel-cobalt hydroxide nanosheets. The hydroxide nanosheets of approximately 0.7 nm thickness were prepared by delamination of layered nickel-cobalt hydroxide lactate in water and formed transparent colloids that were stable for months. The nanosheets were deposited on highly oriented pyrolytic graphite by spin coating, and their electrochemical behavior was investigated by cyclic voltammetry in potassium hydroxide electrolyte. Our method of electrode preparation allows for studying the electrochemistry of nanosheets where the majority of the active centers can participate in the charge transfer reaction. The observed electrochemical response was ascribed to mutual compensation of the cobalt and nickel response via electron sharing between these metals in the hydroxide nanosheets, a process that differentiates the behavior of nickel-cobalt hydroxide nanosheets from single nickel hydroxide or cobalt hydroxide nanosheets or their physical mixture. The presence of cobalt in the nickel-cobalt hydroxide nanosheets apparently decreases the time of electrochemical activation of the nanosheet layer, which for the nickel hydroxide nanosheets alone requires more potential sweeps.

© 2017 Elsevier Inc. All rights reserved.

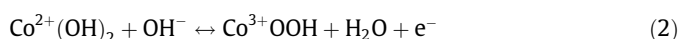
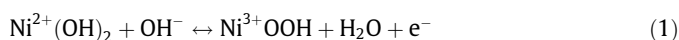
* Corresponding author.

E-mail address: lang@iic.cas.cz (K. Lang).

1. Introduction

Layered transition-metal hydroxides, including layered double hydroxides (LDHs) and layered simple hydroxides (LSHs), have attracted increasing attention as promising active electrode materials for electrochemical energy storage and conversion devices due to facile preparation and modification, good tunability, high capacitance capability, fast reversible redox reactions, and cost effectiveness [1–3]. The structure of these materials is derived from mineral brucite ($\text{Mg}(\text{OH})_2$) composed of edge sharing octahedra with metal cations in the middle coordinated by the hydroxide groups. LDHs contain alternating divalent (e.g., Mg^{2+} , Ni^{2+} , Co^{2+}) and trivalent (e.g., Al^{3+} , Co^{3+}) cations, bringing charge to the hydroxide layer [4]. In the case of LSHs, whose structures are composed of only one type of cation, the charge arises from coordination vacancies [5–7]. Analogously, layered double hydroxide salts (DHSs) are made of two different divalent metals in the hydroxide layer. In all these cases, the positive charge is balanced by exchangeable interlayer anions that strongly influence the resulting physico-chemical properties and can yield new properties, functions, and applications.

Pseudocapacitive electrode materials, based on layered nickel and cobalt hydroxides, have demonstrated a significant improvement in the energy density for the application in supercapacitors [1–3]. The charge storage capability is largely due to a reversible redox reaction, a one-electron process between hydroxide and corresponding oxide-hydroxide (Eqs. (1) and (2)). Both hydroxides crystallize in several polymorphs [8,9], of which the β -phase, the most stable and most often utilized, has the closely packed layered structure with a basal spacing of 4.6 Å and does not contain interlayer anions. On the other hand, the α -phase, an LSH, has more extended structure with interlayer anions between the hydroxide layers and shows promising properties for effective supercapacitive materials [10,11]. The main drawback of α -phase-based electrodes is their low stability towards commonly used alkaline electrolytes. Due to the greater variety of oxidation and coordination states, cobalt atoms form the β -phase or the α -phase with Co^{2+} located in tetrahedral and octahedral sites [12,13], and these phases can be converted into a new LDH phase which is stable and contains both Co^{2+} and Co^{3+} [9].



The range of properties of layered metal hydroxides is dramatically enhanced by their delamination into positively charged hydroxide nanosheets, which can be utilized as building blocks for the construction of nanocomposites or thin films [14,15]. It was reported that delamination occurred in some organic solvents, such as butanol, xylene, or formamide under heating or stirring [16–19]. Later, it was noticed that intercalation of polar and hydrophilic anions between the hydroxide layers can enhance the delamination ability even in water [20], for example, using acetates [21], lactates [22–24], or sulfonates [25]. Considering that most of the supercapacitor reactions occur at or near the surface of electrodes, the surface property of the electrode materials is crucial in determining its pseudocapacitance. High specific capacitance needs a large number of electroactive sites in the electrodes for the enhanced transport rate of electrolyte ions and electrons. Thus, the nanostructured architectures are favorable for improving the electrochemical utilization of the active materials. As described above, the presence of some interlayer anions between the hydroxide layers facilitates synthesis of the nanosized hydroxide sheets, therefore, the α -phase or LDH are preferable for the preparation of nanostructured films and composites [26–31].

Tremendous effort has been devoted to enhancing layered nickel and cobalt hydroxide electrochemical performance. One possible route is the incorporation of other transition metals such as Co^{2+} , Fe^{3+} , Mn^{2+} , Al^{3+} , or Zn^{2+} . These mixed layered hydroxides showed superior electrochemical behavior, differed from physical mixtures [32–38], explained by the improved redox reversibility and porous morphology [39], improved electronic conductivity [40,41], the synergic effect of both cations [42], or by the combination of these effects. Mixed nickel-cobalt hydroxides can be classified as LDHs where nickel is divalent and cobalt is trivalent or as a DHS with both nickel and cobalt in the divalent oxidation state. In some cases, the structures may contain both LDH and DHS motifs, i.e., Ni^{2+} , Co^{2+} , and Co^{3+} cations coexist in one hydroxide layer [43]. Alternatively, layered hydroxides combined with conductive materials such as graphene or carbon nanotubes significantly enhance the electron transport and increase the stability and electrochemical efficiency of α -phase-based electrodes [44–47]. The electrochemical performance could also be positively influenced by enlarging the surface area and thus enhancing the transport of charged particles from the electrolyte. The use of the hydroxide nanosheets allows the fabrication of thin monolayer electrodes, which reduces the slow charge transport in the bulk and significantly increases the efficiency of electrochemical processes [48–50].

In our previous reports, we described a simple, economical, and environmentally friendly preparation of single-layered nickel and cobalt hydroxide nanosheets by delamination of corresponding LSH in water [23,24]. The resulting colloids were used for the fabrication of ultrathin electrodes composed of restacked nanosheets. Herein, we report a facile process to synthesize the nickel-cobalt hydroxide nanosheets in order to explore their electrochemical performance and stability and to quantify the effects of the mixed nanosheet composition. Many reported hierarchical architectures based on nickel-cobalt hydroxides are composed of bulky nanoplatelet-like aggregates; in contrast, in this report we investigate the behavior of the separated hydroxide nanosheets.

2. Experimental section

2.1. Materials

Hexamethylenetetramine (HMT) (Lachema, Czech Republic), sodium dodecyl sulfate (SDS), nickel nitrate and sodium lactate (Sigma-Aldrich), cetyltrimethylammonium bromide (CTAB, Acros Organics), cobalt nitrate and acetone (Lachner, Czech Republic), and chloroform and 1-butanol (Penta, Czech Republic) were used as purchased. Reactions were performed in deionized water (conductivity $<0.15 \mu\text{S cm}^{-1}$). Basal planes of highly ordered pyrolytic graphite (HOPG, ZYB Grade; size $12 \times 12 \text{ mm}^2$, Structure Probe Inc., USA) and mica surface (SPI Supplies) cleaned by adhesive tape (Scotch) stripping served as a support for spin coating and drop casting procedures.

2.2. Characterization techniques

X-ray diffraction patterns of powder samples were collected with a PANalytical X'Pert PRO diffractometer in the Bragg-Brentano geometry in reflection mode. The diffractometer was equipped with a conventional X-ray tube ($\text{CoK}\alpha$, 40 kV, 30 mA) and a multichannel X'Celerator detector. XRD patterns of oriented films were recorded with a PANalytical X'Pert diffractometer allowing the measurement in both reflection and transmission mode. The diffractometer was equipped with a Cu X-ray tube (40 kV, 30 mA). Qualitative analysis was performed with the HighScorePlus software package (PANalytical, Almelo, The Netherlands, version 3.0) and the JCPDS PDF-2 database.

Fourier transform infrared spectra (FTIR) were recorded with a Nicolet NEXUS 670-FT spectrometer using KBr pellets. The UV/vis

absorption spectra were measured using a Perkin-Elmer Lambda 35 spectrometer with an integral sphere. The samples were diluted with barium sulfate. Thermal analyses (TGA/DTA/MS) were performed using a Setaram SETSYS Evolution-16-MS instrument coupled with a mass spectrometry system. The measurements were performed in synthetic air (flow rate 60 mL min^{-1}) from 30 to $1100 \text{ }^\circ\text{C}$ with a heating rate of $5 \text{ }^\circ\text{C min}^{-1}$. Atomic force microscopy (AFM) images were recorded using a Dimension Icon (Bruker) in the Scanasyt mode using Scanasyt-air cantilevers (silicon tip on a silicon nitride lever) and a Nanoscope IIIa Multimode (Bruker) with tapping cantilevers (TESPA, 42 N m^{-1} , $f_{\text{res}} \sim 300 \text{ kHz}$, Bruker, USA). The samples were prepared by spin-coating nanosheet dispersions on mica or basal plane HOPG. Small-angle X-ray scattering (SAXS) experiments were performed using a pinhole camera (Molecular Metrology SAXS System) attached to a microfocussed X-ray beam generator (Osmic MicroMax 002) operating at 45 kV and 0.66 mA (30 W). The camera was equipped with a multiwire gas-filled area detector with an active area diameter of 20 cm (Gabriel design). Two experimental setups were used to cover the q range of $0.004\text{--}1.1 \text{ \AA}^{-1}$; q is the scattering vector defined as $q = (4\pi/\lambda)\sin\theta$, where λ is the wavelength and 2θ is the scattering angle. Cyclic voltammetry was performed in aqueous 1 M KOH deoxygenated by argon with counter Pt and saturated calomel reference (SCE) electrodes. A three-electrode potentiostat Wenking POS2 (Bank Elektronik, Germany) was used for all electrochemical experiments. The samples for electrochemical measurements were prepared using the following procedure: 3 drops of the colloid of the nanosheets (2 mg mL^{-1}) were spin-coated on the HOPG surface. The amount of deposited material was analyzed using inductively coupled plasma mass spectrometry (ICP-MS) after the dissolution of the deposit in concentrated hydrochloric acid (3 h, $90 \text{ }^\circ\text{C}$). The loading mass of the active material on the electrode was between 0.7 and $1.0 \text{ } \mu\text{g cm}^{-2}$. The AFM profile analysis was performed before electrochemical measurements.

2.3. Syntheses

Preparation of layered nickel-cobalt hydroxide dodecyl sulfate (LNiCoH-DS). Nickel nitrate (0.7270 g, 2.5 mmol), 0.7276 g (2.5 mmol) of cobalt nitrate, 5.7678 g (20 mmol) of SDS, and 7.0096 g (50 mmol) of HMT were dissolved in 90 mL of deionized water and 10 mL of 1-butanol. The mixture was stirred and heated to $90 \text{ }^\circ\text{C}$ for 2 h. The resulting precipitate was centrifuged, washed three times by deionized water, and air-dried at room temperature. Elemental analysis (in %): Ni 19.73, Co 10.47, C 23.05, H 5.28, N 1.32, and S 5.03, corresponds to the formula $\text{Ni}_{0.65}\text{Co}_{0.35}(\text{OH})_{1.92}\text{DS}_{0.3}(\text{HMT})_{0.05}\cdot 0.6 \text{ H}_2\text{O}$.

Preparation of layered nickel-cobalt hydroxide lactate (LNiCoH-Lac). LNiCoH-DS (0.6 g), 2.1867 g (6 mmol) of CTAB, and 4.3 mL (30 mmol) of sodium lactate were dispersed in 50 mL of deionized water and 100 mL of chloroform. The mixture was stirred for 1 h at room temperature. The water phase with the product was separated and centrifuged, and the sediment was washed by acetone and three times by water. Then, the resulting colloid (approximately 10 mg mL^{-1}) was centrifuged (Hermle Z36 HK, 20,000 rpm for 20 min), and the green-brown gel was separated and air-dried. Elemental analysis (in %): Ni 27.14, Co 13.61, C 9.89, H 2.81, N 2.30, and S 0.61, corresponds to the formula $\text{Ni}_{0.67}\text{Co}_{0.33}(\text{OH})_2(\text{Lac})_{0.19}\text{DS}_{0.03}(\text{HMT})_{0.06}\cdot 0.7 \text{ H}_2\text{O}$.

Delamination of LNiCoH-Lac. LNiCoH-Lac undergoes delamination during the anion exchange of DS in the interlayer space of LNiCoH-DS for lactate anions. The resulting green-brown dispersion was centrifuged (20,000 rpm for 20 min) to form the greenish gel, which was dispersed in water to form the colloid at concentrations up to approximately 30 mg mL^{-1} . The product, a green-brown colloid dispersion, was transparent and stable for several

months. The dispersions with concentrations above 30 mg mL^{-1} formed gels.

Preparation of mixed layered nickel hydroxide lactate (LNiH-Lac) and layered cobalt hydroxide lactate (LCoH-Lac). LNiH-Lac and LCoH-Lac were synthesized and delaminated using previously developed procedures [23,24]. Water colloids of LNiH-Lac (3.1 mL, 13 mg mL^{-1}) and LCoH-Lac (6.9 mL, 6 mg mL^{-1}) were mixed in a vial to produce the green-brown colloid, which was centrifuged and air-dried at room temperature.

3. Results and discussion

3.1. Aqueous dispersions of the hydroxide nanosheets

The synthesis of LNiCoH-Lac was adapted from previously developed procedures [23,24]. Briefly, the hydrothermal precipitation of a mixed solution of nickel and cobalt salts in the presence of HMT led to LNiCoH-DS. Then, anion exchange of DS for lactate was performed in a biphasic water/chloroform system of CTAB, which removes DS from the hydroxide interlayer space of LNiCoH-DS by forming ion pairs soluble in the chloroform phase [51]. The anion exchange was accompanied by the formation of colloidal dispersions, visualized by the Tyndall effect (Fig. 1). These observations indicate that the synthesis of LNiCoH-Lac is accompanied by delamination yielding the nickel-cobalt hydroxide nanosheets.

XRD patterns of LNiCoH-DS confirm the formation of a microcrystalline layered hydroxide intercalated with the large anion, i.e., they show basal diffractions at 4.01° , 8.11° , and 12.18° (2θ , Cu $K\alpha$), indicating the high degree of ordering along the layer stacking direction, and broad nonbasal diffractions at approximately 34° , 60° , and 70° with tails that extend towards higher 2θ values due to turbostratic disorder (Fig. S1). A basal spacing of 21.98 \AA is comparable to those of monometallic LNiH-DS and LCoH-DS [23,24]. The anion exchange reaction for lactate anions was accompanied by the shrinking of the basal spacing to 9.47 \AA (Fig. 2A). The nonbasal diffractions were intact, confirming the preservation of nickel-cobalt hydroxide layers. The XRD patterns of drop-casted films prepared from the dispersions showed basal diffraction lines in reflection mode, whereas the nonbasal diffractions completely disappeared (Fig. 2B). In transmission mode, only sharp nonbasal diffraction peaks were clearly visible (Fig. 2C). These results document the preferential orientation of the nanosheets parallel to the support surface. The XRD patterns of

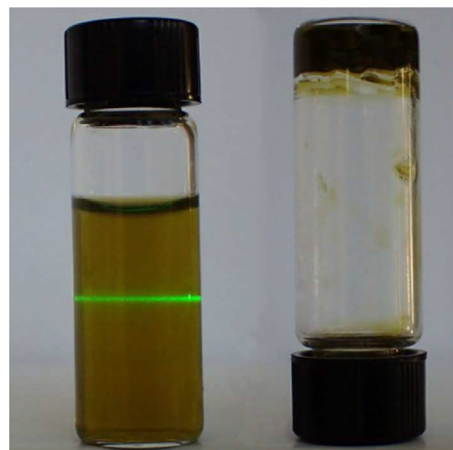


Fig. 1. Delamination of LNiCoH-Lac in water: dispersion of the nickel-cobalt hydroxide nanosheets documented by the Tyndall scattering of green laser light (left); Gel-like dispersion of nanosheets at a concentration above 30 mg mL^{-1} (right).

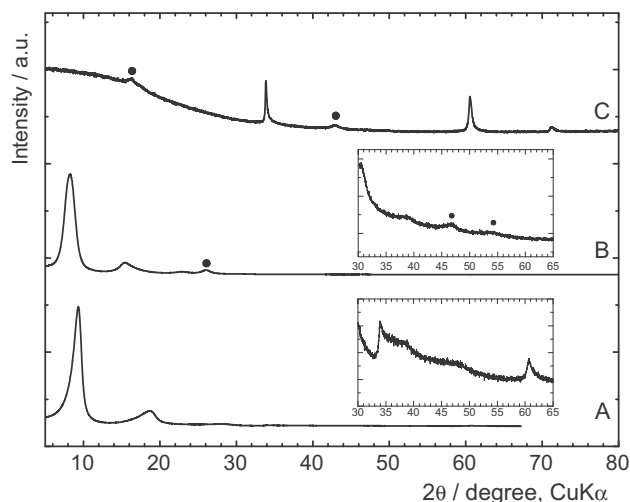


Fig. 2. XRD patterns of LNiCoH-Lac powder (A), and of the drop-casted film in reflection (B) and transmission (C) modes. The diffractograms are shifted vertically to avoid overlaps. The diffraction lines labelled by (●) belong to a Mylar foil used as a support. Inset: Details of nonbasal diffraction lines.

films made by mixing the nickel hydroxide and cobalt hydroxide nanosheets display the same features.

FTIR spectra of all prepared layered hydroxides display vibrations of the intercalated anions, water molecules (the OH stretching vibrations at approximately 3500 cm^{-1} (a) and the OH deformation vibration at 1633 cm^{-1} (c)), and the traces of HMT indicated by the vibration at 1340 cm^{-1} (e) (Fig. 3). The spectrum of LNiCoH-DS is dominated by the bands associated with C–H stretching vibrations in the range $3000\text{--}2800\text{ cm}^{-1}$ (b), the bending vibration of the organic chain at 1468 cm^{-1} (d), and the sulfate characteristic vibrations at 1232 and 1200 (f), 1061 (h), and 997 cm^{-1} (i). Anion exchange of DS for lactate is accompanied by the appearance of the stretching C–OH vibrations at 1122 cm^{-1} (l), and the asymmetric and symmetric stretching modes of the lactate carboxyl group at 1587 (j) and 1402 cm^{-1} (k), respectively. The peaks b, e, g, h, and i indicate a minor presence of adsorbed DS and HMT as the traces of DS and HMT cannot be removed. FTIR spectra of the physical mixture of LNiH-Lac and LCoH-Lac display the same features as that of LNiCoH-Lac (Fig. S2).

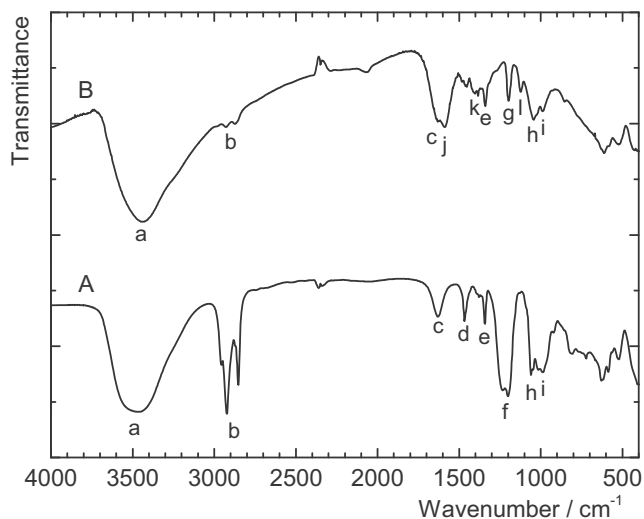


Fig. 3. FTIR spectra of LNiCoH-DS (A) and LNiCoH-Lac (B).

The UV/vis absorption spectra of layered hydroxides reflect the coordination environment of metal atoms in the hydroxide layers (Fig. 4D). LNiCoH-DS has a broad absorption band between 550 and 750 nm composed of two sets of electronic transitions - tetrahedrally coordinated Co^{2+} at 590 and 640 nm and octahedrally coordinated Ni^{2+} at 653 nm with a shoulder at 745 nm, in agreement with the respective spectra of LCoH-DS and LNiH-DS (Fig. 4A and B). The presence of tetrahedrally coordinated Co^{2+} atoms in LNiCoH-DS demonstrates that this hydroxide contains motifs characteristic of DHSs composed of Co^{2+} and Ni^{2+} [12,24]. According to the earlier report [24], Co^{2+} ions in LSH are easily oxidized to Co^{3+} by air, which is accompanied by the formation of a $\text{Co}^{2+}/\text{Co}^{3+}$ LDH phase. The diminishing of tetrahedral Co^{2+} absorption bands (Fig. 4C and E) documents the oxidation of Co^{2+} to Co^{3+} during the ion exchange reaction. This process is further corroborated by measuring the average oxidation state of cobalt ions in LNiCoH-Lac dispersions by iodometric titration. The obtained average oxidation number of 2.73 combined with the results of elemental analyses led to the formal formula of LNiCoH-Lac as $\text{Ni}_{0.67}^{2+}\text{Co}_{0.09}^{2+}\text{Co}_{0.24}^{3+}(\text{OH})_2(\text{Lac})_{0.19}\text{DS}_{0.03}(\text{HMT})_{0.06}\cdot 0.65\text{ H}_2\text{O}$. The traces of adsorbed DS and HMT cannot be removed by washing and were evidenced by FTIR (Fig. 3).

The thermal behavior of LNiCoH-Lac has features similar to those of LNiCoH-DS (Figs. S3 and S4). The first broad endothermic peak between 30 and $125\text{ }^\circ\text{C}$ with a weight loss of 8.1% corresponds to the release of surface and interlayer water molecules. An exothermic peak between approximately 250 and $360\text{ }^\circ\text{C}$ is accompanied by the release of water and carbon dioxide due to dehydroxylation of the hydroxide layers and the thermal decomposition of the interlayer lactate anions. In the case of LNiCoH-DS, there is one endothermic peak at approximately $780\text{ }^\circ\text{C}$, which corresponds to thermal decomposition of DS anions. The total weight losses of 56% and 42% for LNiCoH-DS and LNiCoH-Lac, respectively, are fully consistent with their chemical compositions.

3.2. Morphology of the hydroxide nanosheets

As shown above, the synthesis of LNiCoH-Lac at room temperature concludes with the colloidal dispersions of nickel-cobalt hydroxide particles. The dispersions can be concentrated up to 30 mg mL^{-1} and are stable without sedimentation for months. In contrast to many other layered hydroxides, LNiCoH-Lac powder

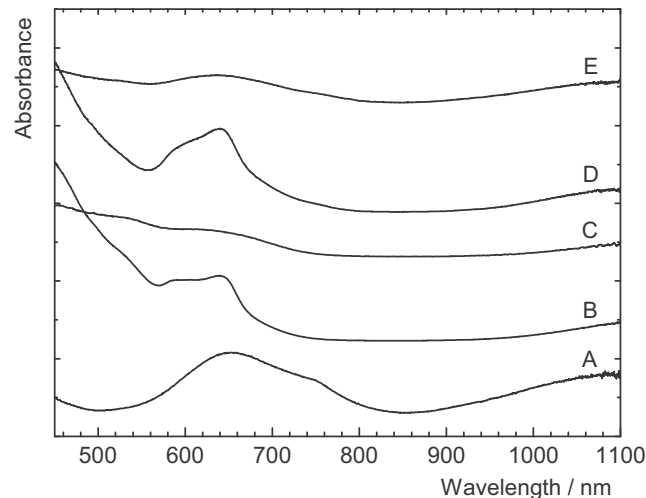


Fig. 4. Absorption spectra of solid LNiH-DS (A), LCoH-DS (B), LCoH-Lac (C), LNiCoH-DS (D), and LNiCoH-Lac (E).

can also form stable dispersions upon shaking in water. The nanomorphology of the dispersed particles was investigated by AFM of spin-coated deposits on a mica surface. In Fig. S5, large side-by-side aggregates with a thickness of approximately 1 nm are shown. The dispersed particles were also analyzed by SAXS at concentrations of 1, 2, and 4 mg mL⁻¹ (Fig. S6). Generally, the scattering intensities follow the equation $I(q) = Aq^{-\alpha} + B$, where the first term corresponds to the scattering of particles, and B is proportional to the particle concentration. The corrected and normalized scattering curves fit each other well, indicating that the particle shape and size do not change with particle concentration. The measured scattering curves decrease proportionally to q^{-2} in the region of lower and middle q -values (Fig. S7). According to the fractal theory, the dimensionality of 2.0 indicates the presence of planar structures. Fitting the corrected SAXS curves with the scattering function derived for planar particles of a homogeneous cross-section (Fig. S7) gives nanoparticle diameters larger than 70 nm with a thickness of 0.7 ± 0.1 nm. The obtained thickness is in good agreement with AFM results. Thus, both AFM and SAXS results show that LNiCoH-Lac is, similarly to monometallic LNiH-Lac or LCoH-Lac, effectively delaminated in water into single hydroxide nanosheets and that spin-coating these nanosheets is a suitable method for the fabrication of well-defined, ultrathin, and large nickel-cobalt hydroxide deposits.

3.3. Electrochemical performance of the hydroxide nanosheets

The electrochemical performance of the nickel-cobalt hydroxide nanosheets as electrode materials was characterized by cyclic voltammetry measurements in 1 M KOH. The colloids of nickel-cobalt hydroxide nanosheets were spin-coated on the basal plane of HOPG. The AFM profile analysis indicates two-dimensional side-by-side aggregates of the respective nanosheets, partially overlaid, with a maximal thickness of approximately 2.5 nm (Fig. 5). This electrode morphology is principal for an investigation of single nanosheet electrochemistry free of effects caused by the bulk material.

Cyclic voltammetry of these nanosheets shows, after an anomalous anodic peak at approximately +400 mV during the first sweep, a steady shift of both peak potentials towards values similar to the redox reaction of the pure nickel hydroxide nanosheets at approximately $E_p = +220$ mV/+310 mV (Fig. 6A and B). This behavior contrasts with the single nickel hydroxide nanosheets exhibiting a considerable rearrangement during the first several sweeps towards more efficient charge transfer (Fig. S8). In order to evaluate the effect of cobalt-doping performance, the voltammetry of

the cobalt hydroxide nanosheets was also investigated: it is characterized by the first anomalous scan, which is followed by a charge drop to the steady state at approximately 30% of the original peak magnitude (Fig. 6C). These changes can be explained by the layer instability upon redox sweeping.

Whereas peak potentials of the nickel-cobalt hydroxide nanosheets reflect a redox behavior of the nickel hydroxide nanosheets, peak currents, which are fully developed already from the first potential scan, resemble the behavior of the cobalt hydroxide nanosheets. Therefore, the slow reorganization occurring during the initial sweeps of the nickel hydroxide nanosheets is missing. The current drop observed between the first and subsequent peaks is milder than in the case of the monometallic cobalt hydroxide nanosheets (Fig. 6C). The charge reversibility of the double metal hydroxide redox reaction is shown in Fig. S9. The charge ratio typical for a reversible process, i.e., $Q_a/Q_c = 1$, declines with an increasing scan rate (v) to approximately 0.75 at $v = 500$ mV s⁻¹, indicating that the charge transfer kinetics are limited by counter-ion diffusion at high scan rates.

For comparison, voltammetric curves of deposited mixtures of the nickel hydroxide and cobalt hydroxide nanosheets show considerably different behavior than the nickel-cobalt hydroxide nanosheets (Fig. 6A and D). The peak couple at $E_p = -45$ mV/+50 mV during the first sweep corresponds to the cobalt hydroxide redox reaction (Eq. (2)). The current of the couple significantly decreases with continuous cycling, whereas a new peak couple, ascribed to the separated nickel hydroxide nanosheets, develops at $E_p = +200$ mV/+345 mV (Eq. (1)). Evidently, these voltammetric curves reflect the behavior of the respective hydroxide nanosheets.

The observed significant influence of both metals in the double metal hydroxide nanosheets can be ascribed to mutual compensation of the cobalt and nickel response via electron sharing between these metals in the hydroxide nanosheets. Considering a one-electron reaction, the charge of approximately 100 μ C exchanged in the electrochemical redox reaction (Fig. 6A) matches well (in order of magnitude) to the number of Co and Ni active centers found on the electrode by elemental analysis. This finding indicates the participation of a majority of the active centers in the charge exchange reaction.

4. Conclusions

This work presents the nanomorphology and electrochemical behavior of the double metal hydroxide nanosheets deposited on the basal plane of highly ordered pyrolytic graphite. Delamination of LNiCoH-Lac into the respective nanosheets and their deposition

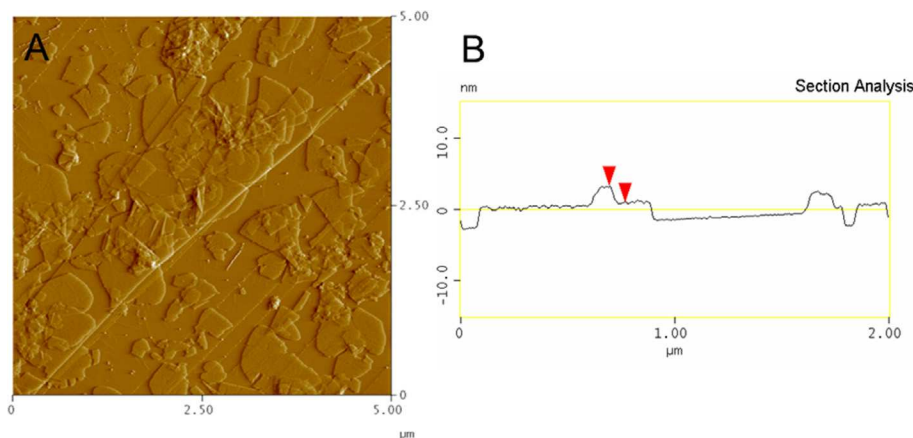


Fig. 5. 2D aggregates of the nickel-cobalt hydroxide nanosheets spin-coated on the basal plane of HOPG: AFM (tapping) topography (A); profile (line) analysis (B). Red arrows indicate a thickness of 2.5 nm. (For interpretation of the references to color in this figure legend, the reader is referred to the web version of this article.)

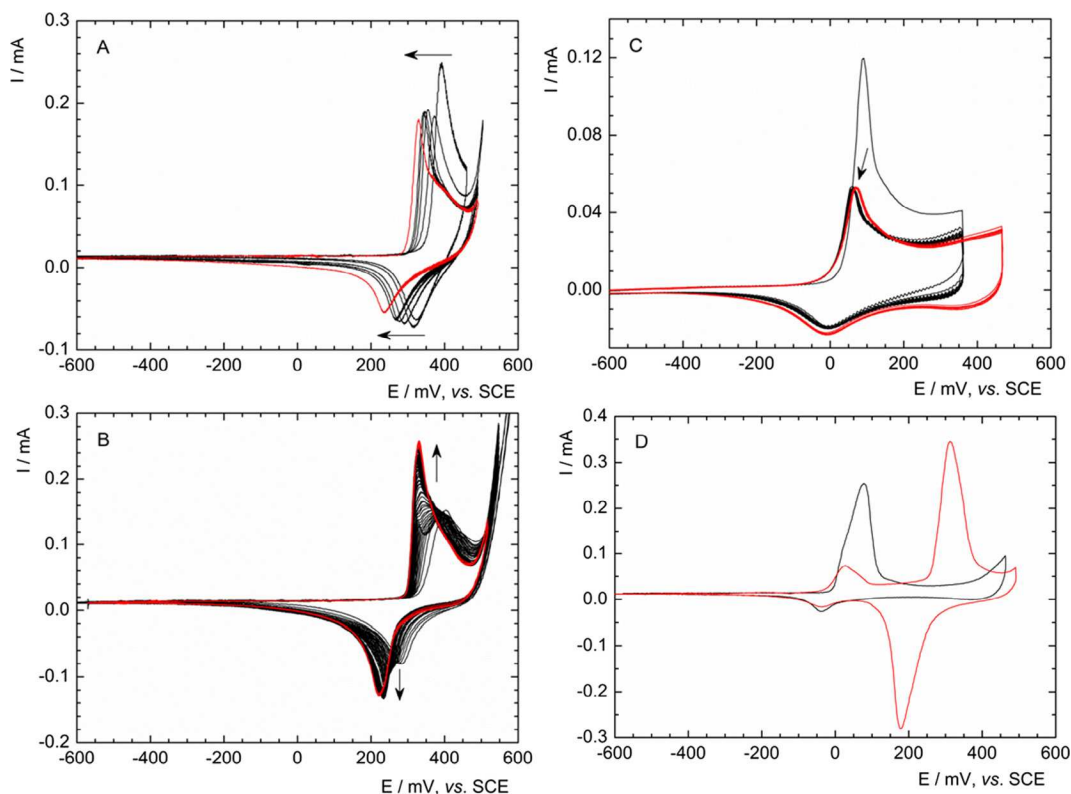


Fig. 6. Cyclic voltammetry of metal hydroxide nanosheets spin-coated on basal plane HOPG: (A) nickel-cobalt hydroxide nanosheets, (B) nickel hydroxide nanosheets, (C) cobalt hydroxide nanosheets, (D) mixed nickel hydroxide and cobalt hydroxide nanosheets (1:1). The arrows show the shifts of the peaks during cycling (black) to the steady-state voltammogram after 40–50 cycles (red). Scan rate $\nu = 100 \text{ mV s}^{-1}$, aqueous 1 M KOH deoxygenated by argon, SCE reference electrode. (For interpretation of the references to color in this figure legend, the reader is referred to the web version of this article.)

on the electrode allow an investigation of electrochemical behavior of the nickel-cobalt hydroxide nanosheets not affected by bulk effects. Voltammetric study indicates that Co-doping can effectively improve the performance of the nanosheets by decreasing the time of their electrochemical activation, which for the pure nickel hydroxide nanosheets requires much more potential sweeps. The observed electrochemical response can be ascribed to mutual compensation of the cobalt and nickel response *via* electron sharing between these metals in the hydroxide nanosheets. For comparison, the voltammograms obtained with bulk nickel-cobalt LDHs show only shifts in the redox peak towards less negative values by an increasing amount of cobalt in the layer [32,34,38]. Evidently, mutual interactions of both metal centers in the nanosheets are much stronger than in the bulk layered material. This effect may have significance for the utilization of metal hydroxide nanosheets in capacitors and other charge storage devices.

Appendix A. Supplementary material

Supplementary data associated with this article can be found, in the online version, at <http://dx.doi.org/10.1016/j.jcis.2017.03.096>.

References

- [1] M. Shao, R. Zhang, Z. Li, M. Wei, D.G. Evans, X. Duan, *Chem. Commun.* 51 (2015) 15880–15893.
- [2] J.P. Cheng, J. Zhang, F. Liu, *RSC Adv.* 4 (2014) 38893–38917.
- [3] H. Yin, Z. Tang, *Chem. Soc. Rev.* 45 (2016) 4873–4891.
- [4] D.G. Evans, R.C.T. Slade, in: X. Duan, D.G. Evans (Eds.), *Layered Double Hydroxides*, Springer, Berlin 119 (2006) 1–87.
- [5] G.G.C. Arizaga, K.G. Satyanarayana, F. Wypych, *Solid State Ionics* 178 (2007) 1143–1162.
- [6] S.P. Newman, W. Jones, *J. Solid State Chem.* 148 (1999) 26–40.
- [7] G. Rogez, C. Massobrio, P. Rabu, M. Drillon, *Chem. Soc. Rev.* 40 (2011) 1031–1058.
- [8] M. Rajamathi, P.V. Kamath, R. Seshadri, *J. Mater. Chem.* 10 (2000) 503–506.
- [9] Z.P. Xu, H.C. Zeng, *Chem. Mater.* 11 (1999) 67–74.
- [10] H. Du, L. Jiao, K. Cao, Y. Wang, H. Yuan, *ACS Appl. Mater. Interfaces* 5 (2013) 6643–6648.
- [11] W.-K. Hu, D. Noréus, *Chem. Mater.* 15 (2003) 974–978.
- [12] L. Poul, N. Jouini, F. Fiévet, *Chem. Mater.* 12 (2000) 3123–3132.
- [13] R. Ma, Z. Liu, K. Takada, K. Fukuda, Y. Ebina, Y. Bando, T. Sasaki, *Inorg. Chem.* 45 (2006) 3964–3969.
- [14] R. Ma, T. Sasaki, *Adv. Mater.* 22 (2010) 5082–5104.
- [15] Q. Wang, D. O'Hare, *Chem. Rev.* 112 (2012) 4124–4155.
- [16] M. Adachi-Pagano, C. Forano, J.-P. Besse, *Chem. Commun.* (2000) 91–92.
- [17] F. Leroux, M. Adachi-Pagano, M. Intissar, S. Chauvière, C. Forano, J.P. Besse, *J. Mater. Chem.* 11 (2001) 105–112.
- [18] T. Hibino, W. Jones, *J. Mater. Chem.* 11 (2001) 1321–1323.
- [19] L. Li, R. Ma, Y. Ebina, N. Iyi, T. Sasaki, *Chem. Mater.* 17 (2005) 4386–4391.
- [20] T. Hibino, M. Kobayashi, *J. Mater. Chem.* 15 (2005) 653–656.
- [21] N. Iyi, Y. Ebina, T. Sasaki, *Langmuir* 24 (2008) 5591–5598.
- [22] C. Jaubertie, M.J. Holgado, M.S. San Román, V. Rives, *Chem. Mater.* 18 (2006) 3114–3121.
- [23] B. Schneiderová, J. Demel, J. Pleštil, P. Janda, J. Bohuslav, D. Ihiwakrim, O. Ersen, G. Rogez, K. Lang, *J. Mater. Chem. A* 1 (2013) 11429–11437.
- [24] B. Schneiderová, J. Demel, J. Pleštil, H. Tarábková, J. Bohuslav, K. Lang, *Dalton Trans.* 43 (2014) 10484–10491.
- [25] N. Iyi, Y. Ebina, T. Sasaki, *J. Mater. Chem.* 21 (2011) 8085–8095.
- [26] C. Nethravathi, N. Ravishankar, C. Shivakumara, M. Rajamathi, *J. Power Sources* 172 (2007) 970–974.
- [27] D. Wang, W. Yan, G.G. Botte, *Electrochem. Commun.* 13 (2011) 1135–1138.
- [28] C. Qiao, Y. Zhang, Y. Zhu, C. Cao, X. Bao, J. Xu, *J. Mater. Chem. A* 3 (2015) 6878–6883.
- [29] P. Lu, Y. Lei, S. Lu, Q. Wang, Q. Liu, *Anal. Chim. Acta* 880 (2015) 42–51.
- [30] L. Wang, C. Lin, F. Zhang, J. Jin, *ACS Nano* 8 (2014) 3724–3734.
- [31] C. Zhang, J. Zhao, L. Zhou, Z. Li, M. Shao, M. Wei, *J. Mater. Chem. A* 4 (2016) 11516–11523.
- [32] X. Liu, R. Ma, Y. Bando, T. Sasaki, *Adv. Mater.* 24 (2012) 2148–2153.
- [33] J. Pu, Y. Tong, S. Wang, E. Sheng, Z. Wang, *J. Power Sources* 250 (2014) 250–256.
- [34] P. Vialat, F. Leroux, C. Taviot-Gueho, G. Villemure, C. Mousty, *Electrochim. Acta* 107 (2013) 599–610.

- [35] P. Vialat, F. Leroux, C. Mousty, *J. Solid State Electrochem.* 19 (2015) 1975–1983.
- [36] Y. Song, X. Cai, X. Xu, X.-X. Liu, *J. Mater. Chem. A* 3 (2015) 14712–14720.
- [37] H. Chen, L. Hu, M. Chen, Y. Yan, L. Wu, *Adv. Funct. Mater.* 24 (2014) 934–942.
- [38] V. Gupta, S. Gupta, N. Miura, *J. Power Sources* 175 (2008) 680–685.
- [39] N. Kumar, H.S. Panda, *RSC Adv.* 5 (2015) 25676–25683.
- [40] X. Wang, T. Song, *New J. Chem.* 40 (2016) 8006–8011.
- [41] D. Liang, S. Wu, J. Liu, Z. Tian, C. Liang, *J. Mater. Chem. A* 4 (2016) 10609–10617.
- [42] X. Zheng, Z. Gu, Q. Hu, B. Geng, X. Zhang, *RSC Adv.* 5 (2015) 17007–17013.
- [43] J. Liang, R. Ma, N. Iyi, Y. Ebina, K. Takada, T. Sasaki, *Chem. Mater.* 22 (2010) 371–378.
- [44] J.W. Lee, T. Ahn, D. Soundararajan, J.M. Ko, J.-D. Kim, *Chem. Commun.* 47 (2011) 6305–6307.
- [45] K.Y. Ma, W.J. Zhao, J.P. Cheng, F. Liu, X.B. Zhang, *J. Colloid Interf. Sci.* 468 (2016) 238–246.
- [46] J.P. Cheng, L. Liu, K.Y. Ma, X. Wang, Q.Q. Li, J.S. Wu, F. Liu, *J. Colloid Interf. Sci.* 486 (2017) 344–350.
- [47] X. Baia, Q. Liua, H. Zhang, J. Liu, Z. Li, X. Jing, Y. Yuan, L. Liu, J. Wang, *Electrochim. Acta* 215 (2016) 492–499.
- [48] L. Ye, L. Zhao, H. Zhang, B. Zhang, H. Wang, *J. Mater. Chem. A* 4 (2016) 9160–9168.
- [49] X. Hu, S. Liu, C. Li, J. Huang, J. Luv, P. Xu, J. Liu, X.-Z. You, *Nanoscale* 8 (2016) (1802) 11797–11802.
- [50] Z. Lv, Q. Zhong, Y. Bu, *Electrochim. Acta* 215 (2016) 500–505.
- [51] E.L. Crepaldi, P.C. Pavan, J.B. Valim, *Chem. Commun.* (1999) 155–156.

Supplementary material

Nickel-cobalt hydroxide nanosheets: synthesis, morphology and electrochemical properties

Barbora Schneiderová,^{a,b} Jan Demel,^a Alexander Zhigunov,^c Jan Bohuslav,^{d,e} Hana Tarábková,^d Pavel Janda,^d Kamil Lang*^a

^a Institute of Inorganic Chemistry of the Czech Academy of Sciences, v.v.i, Husinec-Řež 1001, 250 68 Řež, Czech Republic. E-mail: lang@iic.cas.cz; Fax: +420 22094 1502; Tel: +420 26617 2193

^b Department of Inorganic Chemistry, Faculty of Science, Charles University in Prague, Hlavova 2030, 128 43 Praha 2, Czech Republic

^c Institute of Macromolecular Chemistry of the Czech Academy of Sciences, v. v. i., Heyrovského nám. 2, 162 06 Praha 6, Czech Republic

^d J. Heyrovský Institute of Physical Chemistry of the Czech Academy of Sciences, v.v.i., Dolejškova 3, 182 23 Praha 8, Czech Republic

^e University of Chemistry and Technology, Prague, Technická 5, 166 28 Praha 6, Czech Republic

Content

Figure S1. XRD patterns of LNiCoH-DS.

Figure S2. FTIR spectra of LNiCoH-Lac and a mixture of LNiH-Lac and LCoH-Lac.

Figures S3, S4. DTA/TGA curves for LNiCoH-DS and LNiCoH-Lac.

Figure S5. AFM image of the deposited nickel-cobalt hydroxide nanosheets with the line profile analysis.

Figure S6, S7. SAXS curves of aqueous nanosheet dispersions.

Figure S8: Cyclic voltammetry of the nickel hydroxide nanosheets.

Figure S9. Charge reversibility of the redox reaction of the nickel-cobalt hydroxide nanosheets.

Figure S1. XRD patterns of LNiCoH-DS.

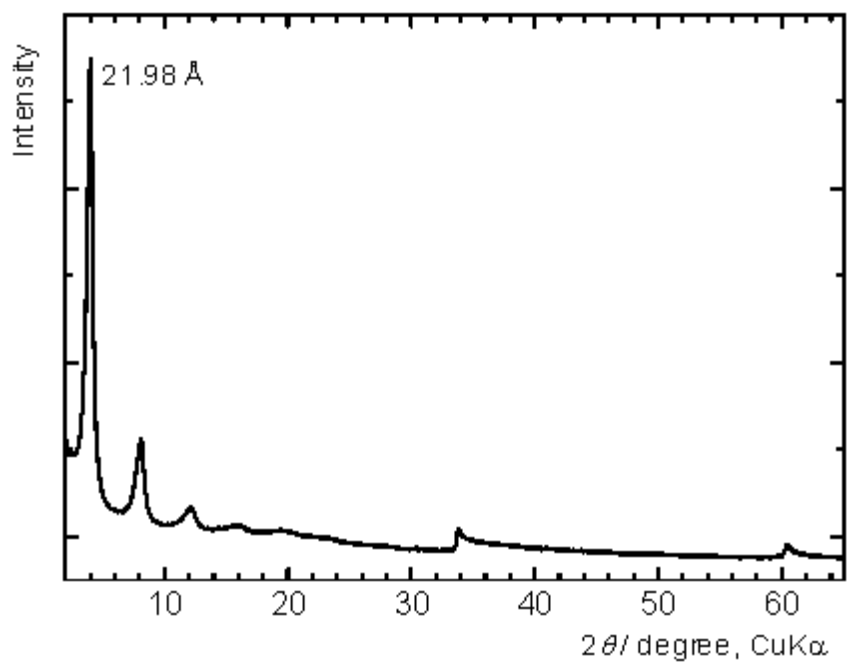


Figure S2. FTIR spectra of LNiCoH-Lac (A) and a mixture of LNiH-Lac and LCoH-Lac (B).

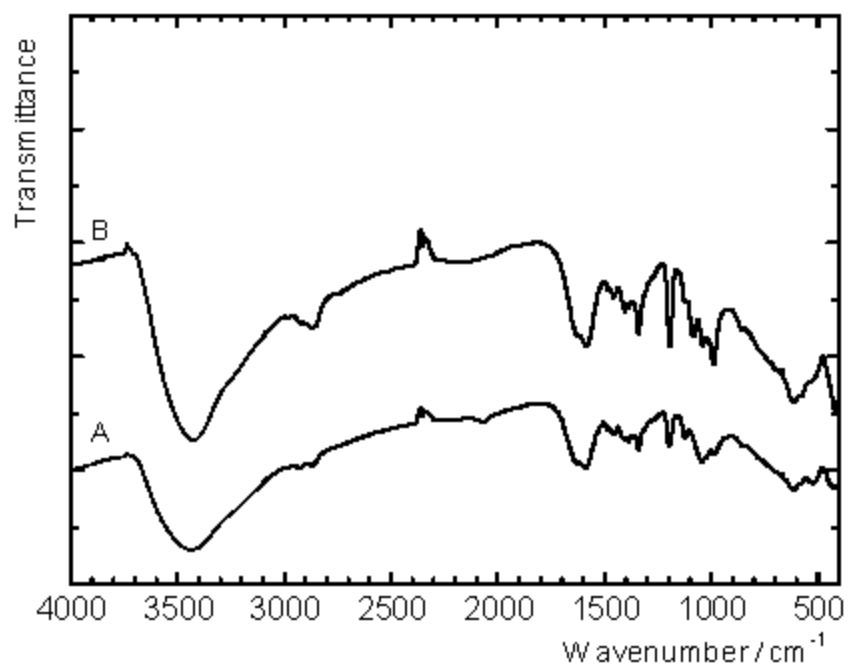


Figure S3. DTA/TGA curves and the evolution of gases for LNiCoH-DS. The measurements were performed in synthetic air (flow rate 60 mL min⁻¹) from 30 to 1100 °C with a heating rate of 5 °C min⁻¹.

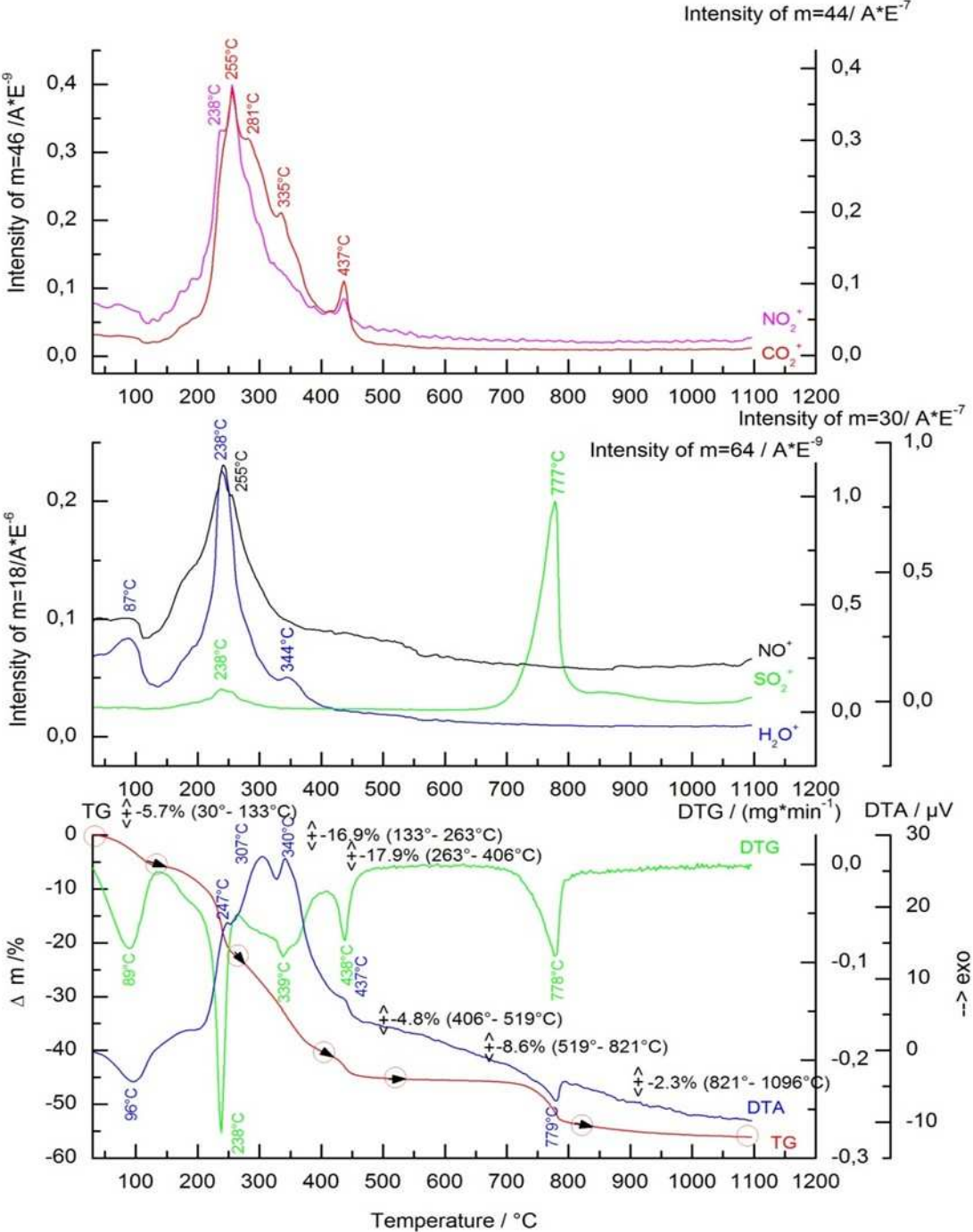


Figure S4. DTA/TGA curves and the evolution of gases for LNiCoH-Lac. The measurements were performed in synthetic air (flow rate 60 mL min⁻¹) from 30 to 1100 °C with a heating rate of 5 °C min⁻¹.

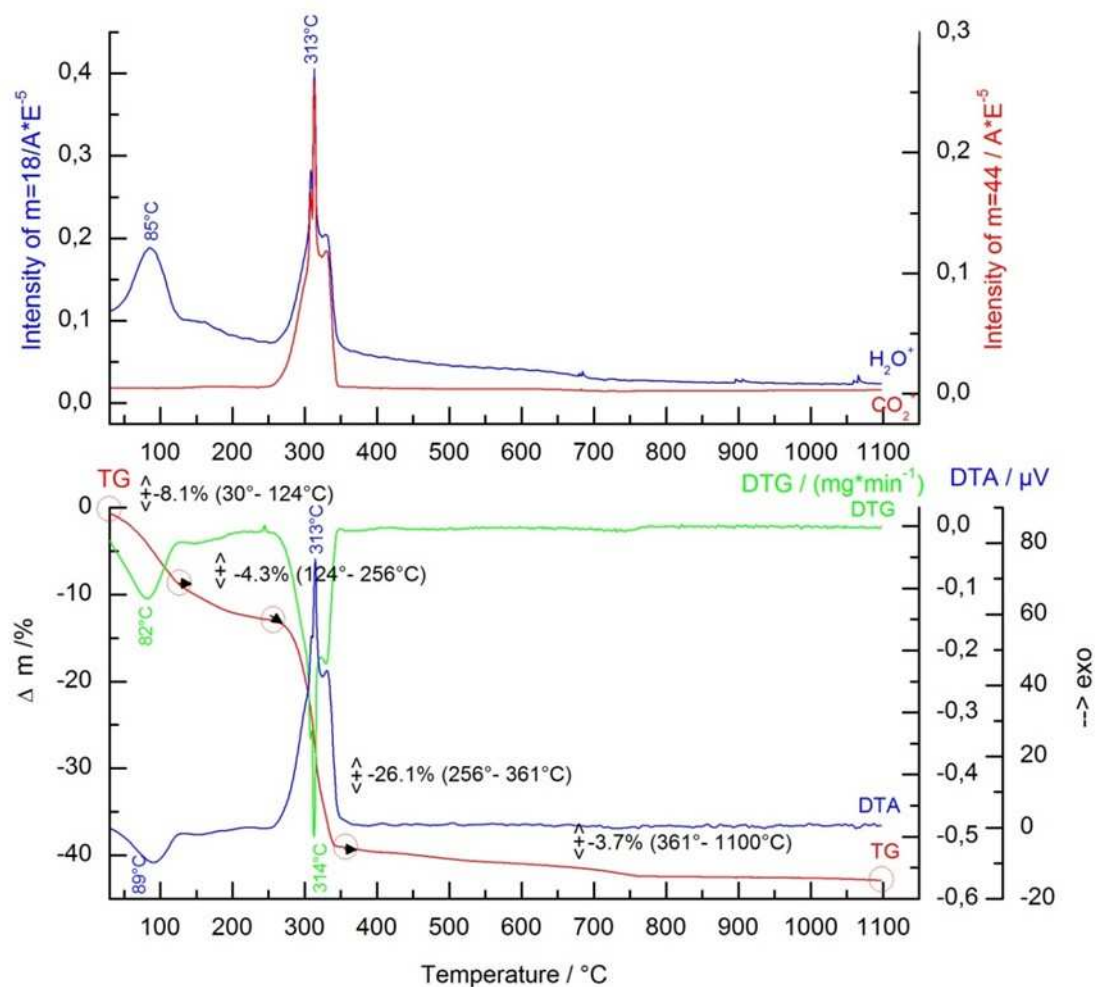


Figure S5. AFM image (top-view topography) of the deposited nickel-cobalt hydroxide nanosheets with the line profile analysis (bottom). The sample was prepared by spin-coating diluted nanosheet dispersion (4 mg mL^{-1} , diluted with water 1:10 000, water was purchased from Sigma-Aldrich, Chromasolv for HPLC,) on a mica support.

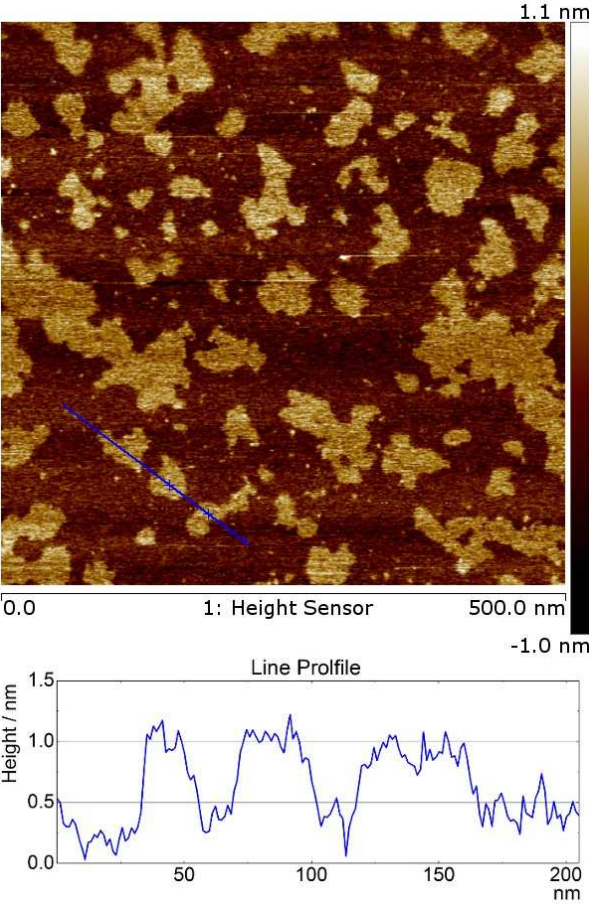


Figure S6. SAXS curves of the aqueous nanosheet dispersions with concentration of 1, 2, and 4 mg mL⁻¹ were corrected for scattering from an empty capillary.

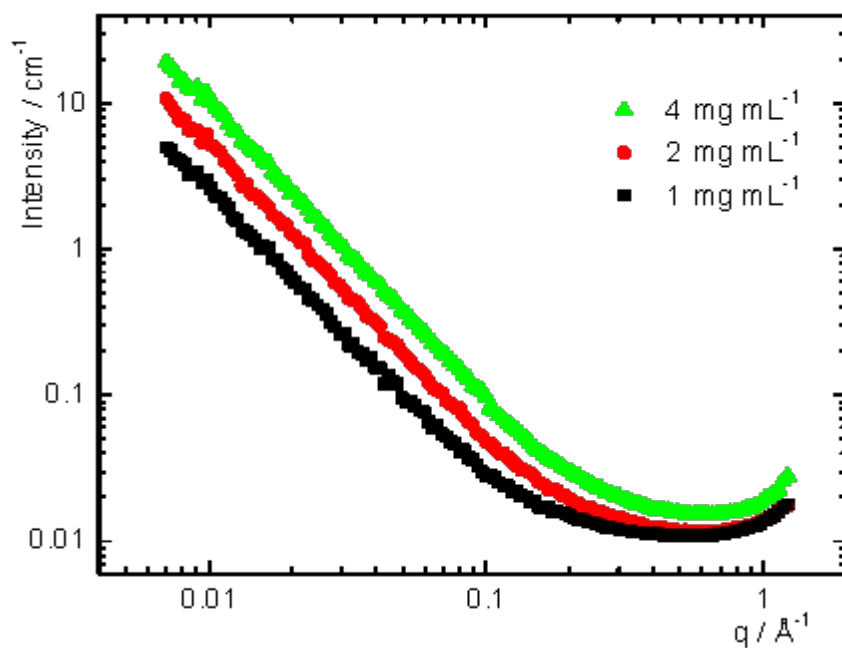


Figure S7. Corrected and normalized SAXS curves of the aqueous nanosheet dispersions to the unit concentration (1 - 4 mg mL⁻¹). The black curve is a fitting scattering function of a model planar particle (1 mg mL⁻¹).

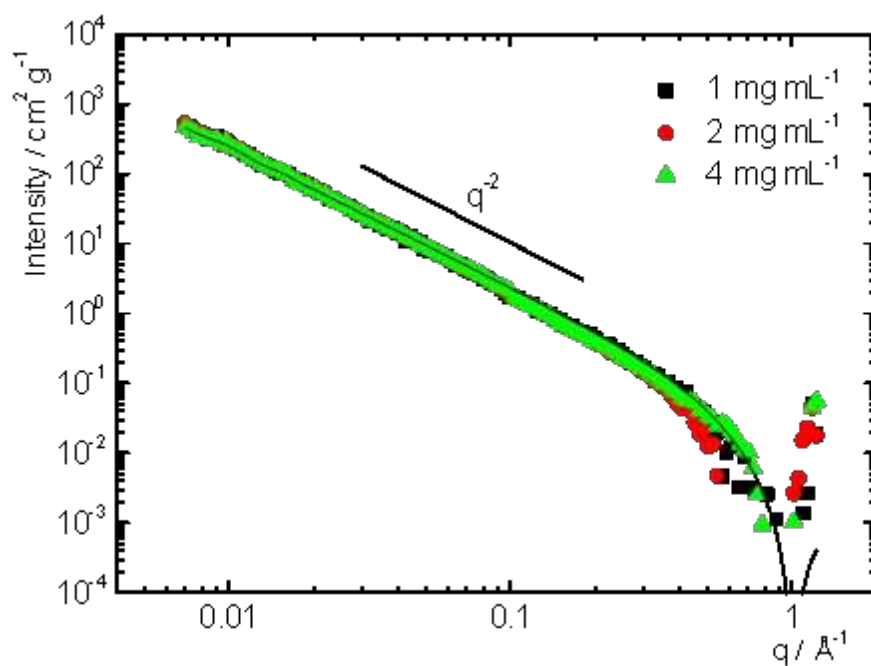


Figure S8: Cyclic voltammetry of the nickel hydroxide nanosheets spin-coated on the basal plane HOPG as a working electrode. Electrochemistry was performed in aqueous 1 M KOH deoxygenated by Ar, scan rate 100 mV s^{-1} , SCE reference electrode. (A) - first three cycles; (B) – the curve development during subsequent 50 cycles (black) to the steady state (green). The arrows show the shifts of the peaks during cycling (black) to the steady-state voltammogram after 50 cycles (green).

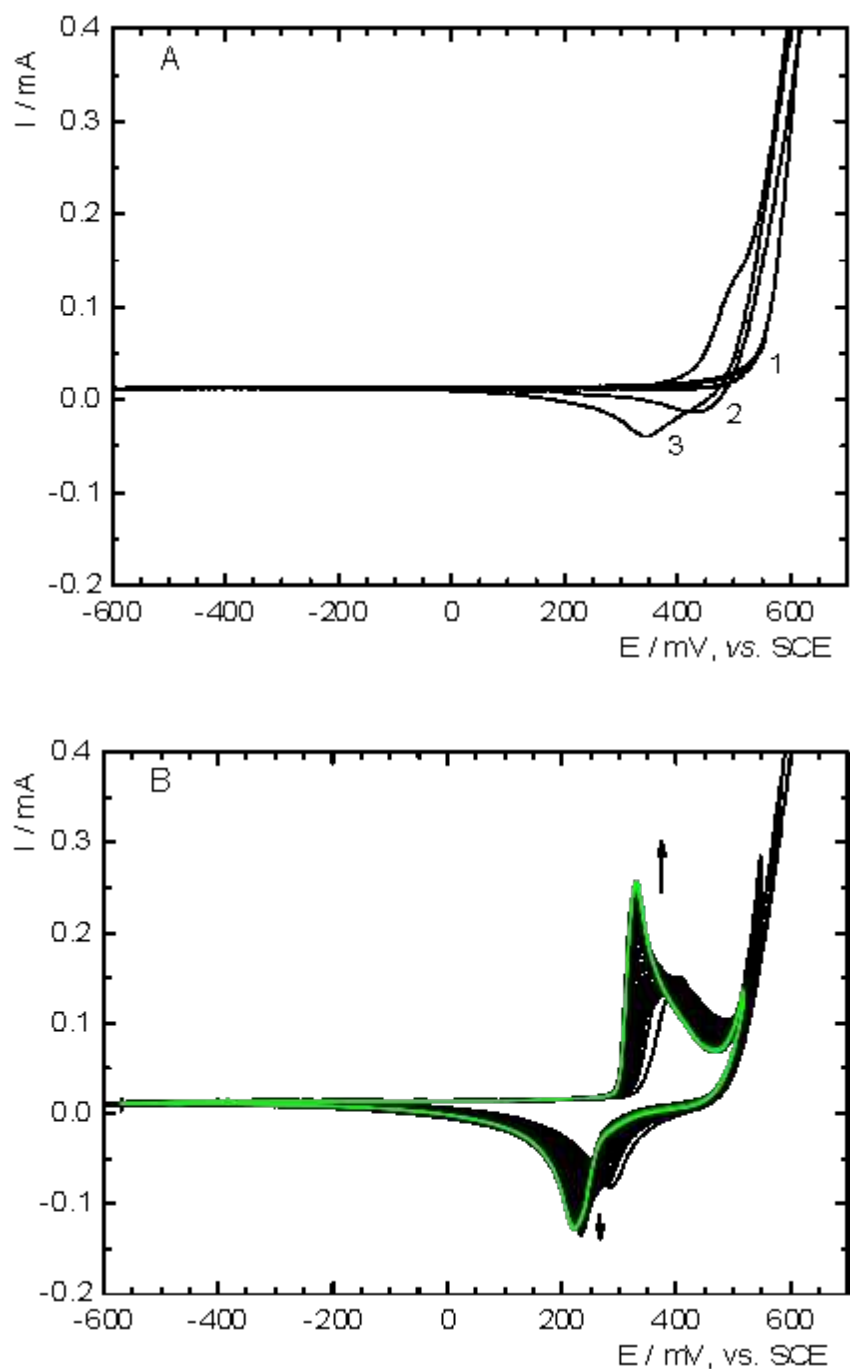


Figure S9. Charge reversibility of the redox reaction of the nickel-cobalt hydroxide nanosheets expressed as a ratio of anodic (Q_a) and cathodic (Q_c) charge Q_a/Q_c , and its dependence on the potential sweep rate (ν), excluding anomalous first peak (see Fig. 5A).

